

2010

# Application of luminescence sensors in oxygen diffusion measurement and study of luminescence enhancement/quenching by metallic nanoparticles

Sanchari Chowdhury  
*University of South Florida*

Follow this and additional works at: <http://scholarcommons.usf.edu/etd>

 Part of the [American Studies Commons](#)

---

## Scholar Commons Citation

Chowdhury, Sanchari, "Application of luminescence sensors in oxygen diffusion measurement and study of luminescence enhancement/quenching by metallic nanoparticles" (2010). *Graduate Theses and Dissertations*.  
<http://scholarcommons.usf.edu/etd/1599>

This Dissertation is brought to you for free and open access by the Graduate School at Scholar Commons. It has been accepted for inclusion in Graduate Theses and Dissertations by an authorized administrator of Scholar Commons. For more information, please contact [scholarcommons@usf.edu](mailto:scholarcommons@usf.edu).

Application of Luminescence Sensors in Oxygen Diffusion Measurement and Study of  
Luminescence Enhancement/Quenching by Metallic Nanoparticles

by

Sanchari Chowdhury

A dissertation submitted in partial fulfillment  
of the requirements for the degree of  
Doctor of Philosophy  
Department of Chemical and Biomedical Engineering  
College of Engineering  
University of South Florida

Co-Major Professor: Venkat R. Bhethanabotla, Ph.D.  
Co-Major Professor: Rajan Sen, Ph.D.  
Randy W. Larsen, Ph.D.  
Vinay K. Gupta, Ph.D.  
Ryan Toomey, Ph.D.

Date of Approval:  
March 24, 2010

Keywords: quantum efficiency, oxygen diffusion, Stern-Volmer plot, surface plasmon  
resonance, alloy nanoparticles, optical properties, dielectric constant

© Copyright 2010, Sanchari Chowdhury

Dedication

To my lovely son Soham

## Acknowledgements

First, I would like to sincerely thank my advisors, Prof. Venkat R Bhethanabotla and Prof. Rajan Sen, for their excellent guidance, constant encouragement and support throughout my PhD studies. This dissertation would not be possible without their intellectual support. I thank Prof. Vinay Gupta, Prof. Randy Larsen and Prof. Ryan Toomey for agreeing to be in my Ph.D. defense committee and for giving me some valuable suggestions during my proposal defense.

My appreciation also extends to the former and present group members of my lab, Dr. Stefan Cular, Dr. Subramanian Sankaranarayanan, Dr. Reetu Singh, Nianthrini Balakrishnan, Ayse Gul Yavuz, Pedro Villalba and Chandra Khoe for their advice and help through these last four years. I must give particular praise to Dr. Stefan Cular for instructing me in the initial techniques for my project. I also thank all those who directly collaborated with me on my thesis projects.

As one of the users of their systems, I would also like to acknowledge the experimental resources provided by Nanomaterial and Nanomanufacturing Research Center (NNRC) of USF without which, this dissertation would be possible. Great support and technical guidance provided by staff members of NNRC are highly appreciated.

Finally, I would like to thank my husband who listened to my ideas, offered suggestions, and always gave me energy, and encouragement. My parents deserve my sincerest love and appreciation for always being there for me with all their unconditional love and encouragement throughout the ups and downs of my life.

## Table of Contents

Table of Contents .....	i
List of Tables.....	vi
List of Figures .....	vii
ABSTRACT .....	x
Chapter 1 - Introduction.....	1
1.1. Introduction to Fluorescence .....	1
1.2. Motivation and Objectives.....	2
1.3. Organization of the Dissertation .....	4
Chapter 2 - Background.....	5
2.1. Luminescence .....	5
2.2. Luminescence Quenching.....	7
2.2.1. Förster Resonance Energy Transfer.....	7
2.2.2. Collisional Quenching and Static Quenching .....	8
2.3. Metal Enhanced Luminescence .....	11
2.3.1. Distance Dependence.....	13
2.3.2. Effect of Surface Plasmon Resonance of Metal Nanoparticles on Luminescence .....	14

2.3.3. Metal Nanoparticles Used for Metal Enhanced Luminescence and Their Synthesis .....	15
2.3.4. Metal Nanoparticles Quenched Luminescence .....	18
2.4. Theoretical Modeling .....	19
2.4.1. Theoretical Investigation of Surface Plasmon Resonance of Nanoparticles .....	20
2.4.2. Modeling of Plasmon Enhanced Luminescence.....	25
2.4.2.1 Calculation of Excitation Enhancement Factor .....	26
2.4.3. Modeling of Effect of Metal Sphere on Excited State Decay Rate.....	27
2.4.3.1 Exact Electrodynamics Theory.....	27
2.4.3.2 Gersten-Nitzan (GN) Model .....	29
2.5. Bimetallic Nanoparticles .....	31
2.5.1. Plasmonic Properties.....	31
2.5.2. Synthesis .....	33
2.5.2.1 Synthesis of Bimetallic Alloy Nanoparticles .....	34
2.6. Characterization Techniques.....	35
2.6.1. Transmission Electron Microscopy (TEM).....	35
2.6.2. Scanning Electron Microscopy (SEM) .....	36
2.6.3. Atomic Force Microscopy (AFM).....	36
2.6.4. Energy Dispersive X-ray Spectroscopy (EDS) .....	37
2.6.5. UV-Vis Absorption Spectroscopy .....	37
2.6.6. Fluorescence Microscopy.....	37

2.6.7. Fluorescence Spectroscopy .....	38
 Chapter 3 - Measurement of Oxygen Diffusivity and Permeability in Polymers	
Using Fluorescence Microscopy.....	39
3.1. Introduction.....	39
3.2. Materials and Methods .....	44
3.2.1. Sensor Films and Polymers .....	44
3.2.2. Instrumentation and Software.....	46
3.2.3. Image Analysis .....	48
3.3. Analytical Models .....	49
3.3.1. Film Separated from The Luminescent Sensor by A Small Volume (Accumulation-in-volume Case).....	49
3.3.1.1 Fick's Equation Combined with The SV Equation.....	49
3.3.1.2 Quasi-steady State Model .....	51
3.3.2. Film-on-sensor Model .....	52
3.4. Results and Discussion .....	52
3.4.1. Characterization of Sensors.....	53
3.4.2. Measurement of Diffusion Using Fluorescence Microscopy.....	58
3.5. Conclusions.....	64
 Chapter 4 - Effect of Ag-Cu Alloy Nanoparticle Composition on Luminescence	
Enhancement/Quenching.....	67
4.1. Introduction.....	67
4.2. Experimental .....	72
4.3. Results and Discussion .....	75

4.4. Conclusions.....	84
Chapter 5 - Silver-Copper Alloy Nanoparticles for Metal Enhanced Luminescence .....	86
5.1. Introduction.....	86
5.2. Experimental Method .....	89
5.3. Results and Discussion .....	93
5.4. Conclusions.....	104
Chapter 6 - Quenching of Fluorescence from CdSe/ZnS Nanocrystals near Copper Nanoparticles in Aqueous Solution.....	106
6.1. Introduction.....	106
6.2. Experimental.....	109
6.2.1. PVP Coated Cu Nanoparticles Synthesis.....	109
6.2.2. CTAB Coated Cu Nanoparticle Synthesis .....	110
6.2.3. Nanoparticles Characterization.....	110
6.2.4. Fluorescence Quenching Experiment .....	111
6.3. Results and Discussion .....	111
6.3.1. Characterization of PVP Coated Copper Nanoparticles .....	111
6.3.2. Collisional Quenching by PVP Coated Copper Nanoparticles .....	112
6.3.3. Characterization of CTAB Coated Cu Nanoparticles.....	116
6.3.4. Quenching Effect of CTAB Coated Cu Nanoparticles on CdSe/ZnS Nanocrystals .....	119
6.3.5. Quenching Mechanism and Effect of Size of Cu Nanoparticles on Quenching Efficiency.....	123
6.4. Summary and Conclusions .....	126

Chapter 7 - Summary, Conclusions and Recommendations.....	128
7.1. Introduction.....	128
7.2. Measurement of O <sub>2</sub> Diffusion Properties Using Inverted Fluorescence Microscopy .....	128
7.3. Ag-Cu Nanoparticles for Enhanced Luminescence .....	129
7.4. Fluorescence Quenching by Cu Nanoparticles .....	130
7.5. Major Contributions .....	131
7.6. Future Directions.....	132
7.6.1. Fluorescence Microscopy for Simultaneous Imaging and O <sub>2</sub> Diffusion Measurement .....	132
7.6.2. Exploration of Other Alloy Nanoparticles for Metal Enhanced Luminescence .....	133
7.6.3. Application of Alloy Nanoparticles for Enhancement of Photovoltaic Cells .....	133
7.6.4. Development of Sensors Based on the Quenching Property of Cu Nanoparticles .....	134
7.6.5. Theoretical and Computational Modeling of Optical Properties of Alloy Nanoparticles .....	134
References.....	136
About The Author.....	End Page

## List of Tables

Table 3-1	SV constants of different microscopic regions of luminescence sensors .....	56
Table 3-2	Oxygen diffusion coefficients for various polymers .....	61
Table 5-1	Fluorescence enhancements of Alexa Fluor 488 and Alexa Fluor 594 on the Ag and Ag-Cu nanoparticles. ....	102
Table 6-1	Concentration of reactants and characteristics of the synthesized Cu nanoparticles .....	118
Table 6-2	Summary of SV equation and quenching constants for different size CTAB coated Cu nanoparticles .....	122

## List of Figures

Figure 2-1	Jablonski diagram.....	5
Figure 2-2	Schematic of Förster resonance energy transfer (FRET).....	8
Figure 2-3	Quenching by intersystem crossing.....	9
Figure 2-4	Dexter interaction.....	10
Figure 2-5	Modified Jablonski diagram in the presence of metal.....	13
Figure 2-6	Distance dependence on the effect of metal on luminescence.....	13
Figure 3-1	Molecular Structure of PtOEP and PtTFPP.....	43
Figure 3-2	Schematic diagrams of diffusion cells for (a) film on sensor experiment and (b) accumulation in volume experiment.....	45
Figure 3-3	Pseudo-colored microscopic fluorescence intensity images (1.64 mm X 2.19 mm) of two luminescence sensors (PtTFPP/PS).....	54
Figure 3-4	SV plot for different regions of sensor a.....	55
Figure 3-5	Experimental and fitted data for the 0.025 mm thick Teflon film (* experimental data – fitted data from model). .....	59
Figure 3-6	Experimental and fitted data (* experimental data – fitted data from model) for the 0.8 mm thick PDMS film.....	59
Figure 3-7	Experimental and fitted data (* experimental data – fitted data from model) for 0.55 mm 3-6265 HP polymer film (silicone elastomer) .....	60
Figure 3-8	Data for the 0.65 mm thick PDMS film containing 10% zeolite (* experimental data – fitted data from model). .....	63
Figure 4-1	$\epsilon_2$ of 10 nm Ag and Cu nanoparticles.....	71
Figure 4-2	Molecular structure of Cy3.....	71
Figure 4-3	Normalized absorption spectra for Ag-Cu alloy nanoparticles. Dotted line is for Ag-Cu nanoparticles with 33% Cu on glass slides. ....	75

Figure 4-4	TEM image of Ag-Cu np synthesized from different composition feeding solution (A) Ag/Cu (1/1) and (B) Ag/Cu (3/7). STEM EDS spectra for (C)Ag/Cu (1/1) (d) Ag/Cu (2/1).....	77
Figure 4-5	SEM images of (A) Ag nanoparticles (B) 2:1 Ag-Cu nanoparticles (C) 1:1 Ag-Cu nanoparticles coated on glass substrate. ....	78
Figure 4-6	AFM images of (D) Ag nanoparticles (E) 2:1 Ag-Cu nanoparticles (F) 1:1 Ag-Cu nanoparticles coated on glass substrates.....	78
Figure 4-7	Pseudo colored image of Cy3 coated on (A) glass (B) Ag (C) 1:1 Ag-Cu and (D) Cu nanoparticles.....	79
Figure 4-8	Experimentally observed luminescence enhancement ration of Cy3. (B) Inset shows the calculated overall quantum efficiency ratio.....	81
Figure 4-9	Calculated overall quantum efficiency measurement factor due to emission enhancement (B) and excitaion enhancement factor.....	81
Figure 4-10	Quantum efficiency enhancement ratio of Cy3 in the proximity of different diameter Ag-Cu nanoparticles at different composition.. ....	83
Figure 5-1	Picture of DC magnetron sputterer with Ag-Cu target.....	90
Figure 5-2	Luminophore on Ag-Cu nanoparticles platform.....	92
Figure 5-3	High resolution TEM image of Ag nanoparticles .....	94
Figure 5-4	(A)-(B) HRTEM image of Ag-Cu.....	95
Figure 5-5	STEM EDS spectra for Ag-Cu alloy nanoparticles.....	96
Figure 5-6	Absorption spectra of Annealed Ag-Cu nanoparticles (surface ratio of Cu in sputter target is 7.5%).....	97
Figure 5-7	Calculated extinction spectra for the Ag-Cu core-shell (Ag in core and Cu in shell) materials at different shell layer thickness.. ....	98
Figure 5-8	SPR spectrum of Ag-Cu and Ag nanoparticles and absorption and emission spectrum of Alexa Fluor 594 and Alexa Fluor 488.....	99
Figure 5-9	Image of Alexa Fluor 488 coated on (A) glass (B) 448 K annealed Ag-Cu . Alexa Fluor 594 coated on (C) glass (D) 298 K Ag-Cu. ....	100
Figure 5-10	Calculated extinction coefficient (black), and overall quantum efficiency enhancement ratio for (blue) Ag (dotted line) and 1:1 Ag-Cu nanospheres (solid line).....	103

Figure 5-11	Calculated extinction coefficient (black), emission enhancement factor (green) and excitation rate enhancement factor (red) for Ag (dotted line) and 1:1 Ag-Cu nanospheres (solid line). .....	104
Figure 6-1	HRTEM micrograph of (A) Cu nanoparticles (B) Red CdSe/ZnS nanocrystals, and (C) STEM EDS spectra of the Cu nanoparticles. ....	112
Figure 6-2	Normalized absorbance spectrum of copper nanoparticles and emission spectrum of CdSe/ZnS nanocrystals. ....	113
Figure 6-3	(A) The emission spectra of yellow nc at different concentration of Cu nanoparticles. (B) Queneching efficiency measured at 580 nm.....	114
Figure 6-4	Stern-Volmer plot of $\frac{I_0}{I}$ for 500 nanomolar concentration of CdSe/ZnS nanocrystals vs. concentration of copper nanoparticles.....	115
Figure 6-5	High resolution TEM images of different sizes CTAB coated copper nanoparticles (A) sample a (B) sample b (C) sample c .....	117
Figure 6-6	Normalized absorbance spectra of different size Cu nanoparticles in aqueous solution.....	117
Figure 6-7	Absorbance spectra of 500 micromol and diluted (1 micromol) copper nanoparticles. ....	119
Figure 6-8	Effect of sample- a, sample b and sample c copper nanoparticles concentration on the 500 nanomol red CdSe/ZnS nanocrystals. ....	120
Figure 6-9	SV plot for 500 nanomolar concentration of red CdSe/ZnS nc for different size Cu nanoparticles. ● sample a ▲ sample b ■ sample c .....	122
Figure 6-10	Normalized absorbance spectra (--) of different size Cu nanoparticles and the excitation (- . -) and emission spectra (...) red CdSe/ZnS nc.....	124
Figure 6-11	Relative dynamic quenching constants ( $K_D$ ) (■) and static quenching constants ( $K_S$ ) (●) vs the mean diameter of Cu nanoparticles.....	126
Figure 6-12	Ratio of theoretically calculated luminescence quantum yields of a dipole emitter with and without copper metal nanosphere. ....	126

Application of Luminescence Sensors in Oxygen Diffusion Measurement and Study of  
Luminescence Enhancement/Quenching by Metallic Nanoparticles

Sanchari Chowdhury

ABSTRACT

The first part of this dissertation deals with the application of a luminescence quenching method to measure diffusion and permeation coefficients of oxygen in polymers. Most luminescence oxygen sensors do not follow linearity of the Stern-Volmer (SV) equation due to heterogeneity of luminophore in the polymer matrix, thus the complexity of data analysis is increased. To circumvent this limitation, inverted fluorescence microscopy is utilized in this work to investigate the SV response of the sensors at the micron-scale. In these diffusion experiments, oxygen concentration is measured by luminescence changes in regions with high SV constants and good linearity. Thus, we avoid numerical complexity of combining nonlinear SV equation with a diffusion model. This technique allows us to measure oxygen diffusion properties in different type of polymers like transparent, opaque, free-standing polymers and polymers that cannot be cast into free standing films and polymer composites.

In the second part of this thesis, we have explored the effect of Ag-Cu alloy nanoparticles on the emission intensity of luminophores at their close proximity. Alloy nanoparticles offer additional degrees of freedom for tuning their optical properties by altering atomic composition and atomic arrangement and thus can be an attractive option for manipulating signal of a wide range of luminophores. In this work, surface plasmon

resonance spectrum of Ag-Cu alloy nanoparticles deposited by sputtering was easily tuned in wide wavelength range by varying one experimental condition- annealing temperature. Large metal enhanced luminescence for different luminophores *viz* Alexa Fluor 594 and Alexa Fluor 488 were achieved at the vicinity of Ag-Cu nanoparticles when maximum spectral overlap between SPR spectra of Ag-Cu nanoparticles and the emission and absorption spectra of the luminophores occur. We also studied the effect of composition of Ag-Cu nanoparticles synthesized by the polyol process on the luminescence of low quantum yield dye Cy3.

In the third part of this thesis, quenching effect of Cu nanoparticles on CdSe/ZnS nanocrystal quantum dots has been explored. As Cu nanoparticles have comparable dielectric properties with gold nanoparticles, they are expected to show similar quenching effects. It was found that Cu is an efficient quencher of fluorescence from CdSe/ZnS quantum dots and the quenching effect is due to resonance energy transfer from quantum dots to Cu nanoparticles.

## Chapter 1 - Introduction

### 1.1. Introduction to Fluorescence

Fluorescence is an extensively used method in the fields of biotechnology, sensors, cellular imaging, medical diagnostics, immunoassay, flow cytometry, and DNA sequencing, to name a few.<sup>1-3</sup> All the observables including quantum yields, anisotropies, spectral shifts and lifetimes, have been used in wide ranging applications of fluorescence.<sup>1</sup> There are many factors which can influence fluorescence and can result in enhancement or quenching of emission. The change of emission intensity has profound implications in most fluorescence applications. For example, fluorescence quenching by different elements like O<sub>2</sub>, NO, and heavy metal ions can be used to detect those elements in the environment as well as in biological samples.<sup>1</sup> On the other hand, fluorescence enhancement is one of the most important design properties for luminophores in applications like improved surface immunoassay, cellular imaging, DNA detection, and enhanced wavelength-ratiometric sensing, and amplified assay detection.<sup>2</sup> Appropriately designed nanostructured platforms of some conducting metals like Ag, Au, Cu and Al can result in strong emission and can reduce the lifetime, thus increasing photostability of vicinal luminophores.<sup>3</sup>

## 1.2. Motivation and Objectives

The objective for the first part of this dissertation is to develop an efficient fluorescence quenching based technique for the measurement of oxygen diffusion in polymers using inverted fluorescence microscopy.

The motivation behind the first objective is as follows: Luminescence sensors have increasingly found promising applications for measuring oxygen diffusion properties of polymers as a result of their simplicity and high sensitivity to oxygen concentration changes. Frequently, these methods use the specific assumption that luminescence quenching which occurs in the sensor film in response to  $O_2$  concentration follows the linear Stern-Volmer (SV) equation.<sup>4</sup> This does not lead to satisfactory results in many cases as for many luminophore molecules, average intensity change with oxygen concentration does not follow the linearity of Stern-Volmer equation due to the heterogeneity of dye dispersed in the polymer matrix. Though several models were developed for describing the nonlinear response of the sensors, all sensors do not follow the same nonlinear model.<sup>5</sup> It is complicated to derive analytical models combining different nonlinear SV models with the Fick's law subjected to different sets of boundary conditions. This nonlinearity issue can be addressed by the proposed fluorescence microscopy technique which would allow one to investigate SV response of luminescence sensors at the micron scale.

The focus of the second part of this dissertation is on establishing scientific principles that exploit the unique and intense optical properties of metal alloy nanoparticles for optimum luminescence enhancement of vicinal luminophores. The following motivate this focus: the most important properties of metallic nanoparticles on

which luminescence enhancement depends are the surface plasmon resonance spectra, scattering and ohmic losses of nanoparticles.<sup>3,7</sup> Understanding the effect of these properties thoroughly and the ability to tune these properties to maximize the spectral overlap between emission and excitation spectra of luminophore molecules and surface plasmon resonance spectrum of nanoparticles enable the design of an effective nanoparticle platform which can enhance the intensity of particular luminophores the most. Alloy nanoparticles offer additional degrees of freedom for tuning their above properties by altering atomic composition and atomic arrangement, and can be an attractive option for enhancing emission intensity of a wide range of luminophores.

Another objective is to develop a theoretical approach for predicting suitable nanostructures for metal enhanced luminescence and interpreting experimentally observed phenomena. Application of reliable theoretical models for the effect of metal nanostructures on luminescence would reduce the number of experimental trials and serve as a guideline for producing suitable nanoparticles for both metal enhanced and quenched luminescence. So, a fundamental understanding of the mechanism of influence of different materials and their properties is expected to result from this research. It is expected that this improved understanding will lead to optimum metal nanostructure platforms for most efficient luminescence applications.

The third part of this dissertation deals with the study the quenching effects of Cu nanoparticles on luminescence emission. This is motivated by the fact that luminescence quenching of luminophores is mostly studied on gold nanoparticle platforms.<sup>8</sup> The imaginary component of the dielectric constant of copper is comparable to that of gold in the wavelength range of 400 nm to 500 nm, and almost twice in the wavelength range of

500 nm to 625 nm. Hence, it is expected that Cu nanoparticles will be better and less expensive alternative to gold for luminescence quenching.

### 1.3. Organization of the Dissertation

This dissertation is organized in seven chapters. Chapter 2 provides the basic concepts of luminescence and the effect of metallic nanoparticles on luminescence are discussed. The details of luminescence quenching and then those of luminescence enhancement by metallic nanoparticles are presented. A brief overview of plasmonic properties of bimetallic nanoparticles and their synthesis are given after this. Characterization techniques used in this dissertation are described at the end of this chapter. Chapter 3 describes the fluorescence quenching based method for the measurement of oxygen diffusivity and permeability in polymers using fluorescence microscopy. Chapter 4 discusses study of the effect of Ag-Cu alloy nanoparticle composition on luminescence enhancement/quenching. Chapter 5 studies the manipulation of surface plasmon resonance spectra of silver-copper alloy nanoparticles and its application in metal enhanced luminescence. Chapter 6 describes fluorescence quenching effect of Cu nanoparticles on CdSe/ZnS quantum dots in aqueous solution. Chapter 7 summarizes the contents of this dissertation and suggests possible future research directions.

## Chapter 2 - Background

### 2.1. Luminescence

Photoluminescence is a molecular level process which can be described as an excitation to a higher energy state due to absorption of photons which then return a to lower energy state accompanied by the emission of photons with longer wavelength.<sup>1</sup> This phenomenon can be described nicely by the Jablonski diagram (Figure 2-1).

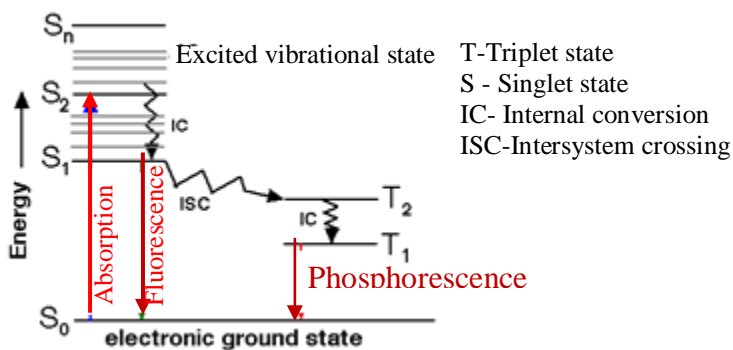


Figure 2-1 Jablonski diagram<sup>1</sup>

In the ground state or the singlet state, fluorophores can exist in a number of vibrational energy levels. Following light absorption, fluorophore molecules are typically excited to some higher vibrational level of  $S_1$  or  $S_2$ . In most cases, fluorophore molecules rapidly relax to the lower vibrational energy level of singlet state from where these molecules emit energy as radiative or non radiative decay. This relaxation time is  $10^{-12}$  second or less whereas fluorescence lifetime is typically near  $10^{-12}$  second.

The emission energy is less than the excitation energy. This phenomenon was first observed by Sir G.G. Stokes in 1852 in Cambridge.<sup>1</sup> Hence, this wavelength shift is called Stokes' shift. Photoluminescence can be of two types: phosphorescence and fluorescence. If the emission occurs from excited singlet states then it is called fluorescence. In this case the electron in the excited state is paired with the electron in the ground state orbital so the return to ground state is allowed. As a result, the fluorescence life time is very short, of the order of nanoseconds. In case of phosphorescence, absorbed photons undergo intersystem crossing into a state of higher spin multiplicity, usually a triplet state, and emit photons which return back to the ground state. As this transition is forbidden, emission rate is very slow and lifetime is usually in the range of milliseconds to seconds.

The luminescence lifetime and quantum yield are two very important characteristics of luminophores. If populations of luminophores are excited, the lifetime is the time it takes for the number of excited molecules to decay to 1/e or 36.8% of the original population. The quantum yield can be defined as the ratio of number of emitted photons to the number of absorbed photons. A fraction of the energy from the photons at excited state is emitted as non-radiative decay. Hence, the quantum yield is less than 1.

Quantum yield (Q) can be given by

$$Q = \frac{\Gamma}{\Gamma + k_{nr}} \quad 2-1$$

where  $\Gamma$  is radiative decay rate and  $k_{nr}$  is non-radiative decay rate.

## 2.2. Luminescence Quenching

A number of processes can lead to a quenching in luminescence intensity. These processes can occur during the excited state lifetime – for example, collisional quenching, energy transfer, charge transfer reactions or photochemistry, or they may occur due to formation of complexes in the ground state. Quenching due to collisional encounters between luminophore and quencher molecule is called dynamic or collisional quenching. In case of static quenching luminophore molecules bind with quencher molecules and form nonfluorescent complexes. Resonance energy transfer from luminophore molecule to the acceptor molecule also results in the quenching of fluorescence. In the following sections these quenching processes are discussed in detail.

### 2.2.1. Förster Resonance Energy Transfer

Resonance energy transfer occurs from excited fluorophore molecule (donor molecule) to an acceptor molecule. The acceptor molecule can be fluorescent or nonfluorescent. In both cases quenching of fluorescence of donor molecule occurs. If the acceptor is fluorescent, it may emit, otherwise it will lose acquired energy as heat. Resonance energy transfer does not require molecular contact as this happens through a space interaction and there is no direct interaction between the electron clouds in the molecules.

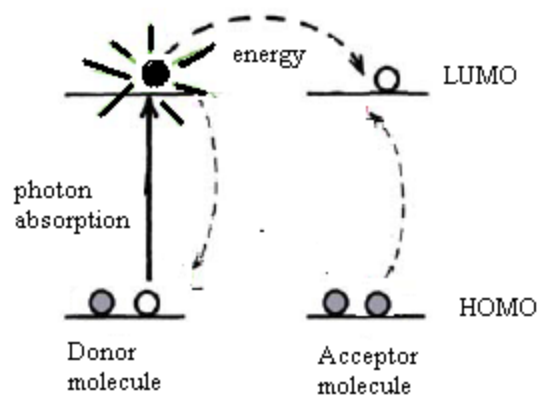


**Figure 2-2 Schematic of Förster resonance energy transfer (FRET)**

The distance dependence of quenching rate due to resonance energy transfer can be given by the following equation

$$Q(r) = \frac{1}{\tau_D} \left( \frac{R_0}{r} \right)^6 \quad (2-2)$$

where  $\tau_D$  is the donor lifetime in the absence of acceptor,  $r$  is the center-to-center distance between donor and acceptor molecule, and  $R_0$  is the Förster distance.

### 2.2.2. Collisional Quenching and Static Quenching

For both collisional and static quenching, molecular contact between luminophore molecule and quencher molecule is required so that the electron clouds of both molecules can interact. There are at least three mechanisms for these quenching processes, i.e. intersystem crossing or the heavy atom effect, electron exchange or Dexter interactions and photoinduced electron transfer. Quenching can occur by any combination of these mechanisms.

In case of intersystem crossing (Figure 2-4) due to encounter with some quencher molecules excited fluorophore molecules ( $F^*$ ) transfers to excited triplet state ( $FT^*$ ) from

excited singlet state. As the emission from excited triplet states is usually delayed, these molecules are likely to be quenched to the ground state by same quencher molecule or result in more loss of energy by nonradiative decay. Quenching by heavy halogen atoms and oxygen are the examples of this kind of quenching.

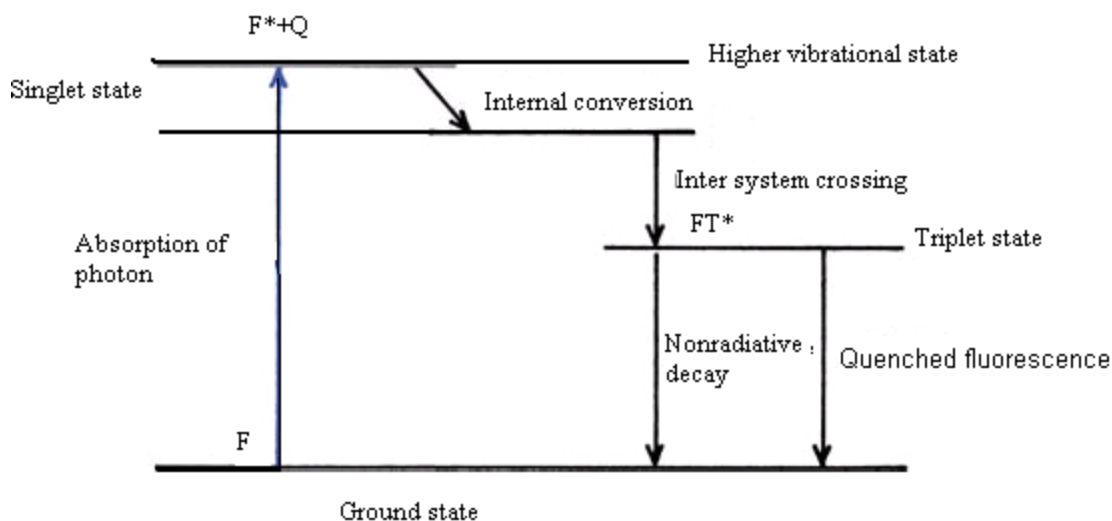


**Figure 2-3 Quenching by intersystem crossing**

In case of electron exchange quenching or Dexter interaction, luminophore molecules act as donor molecules and transfer the electron to acceptor molecules. Electron transfer first occurs from excited donor mole in LU orbital to acceptor molecule. Then acceptor molecule transfers back the electron to donor molecule from HO orbital. Quenching by this process is similar as resonance energy transfer and also it depends on spectral overlap. However, it is a short distance process (15-20 Å) in contrast to resonance energy transfer.

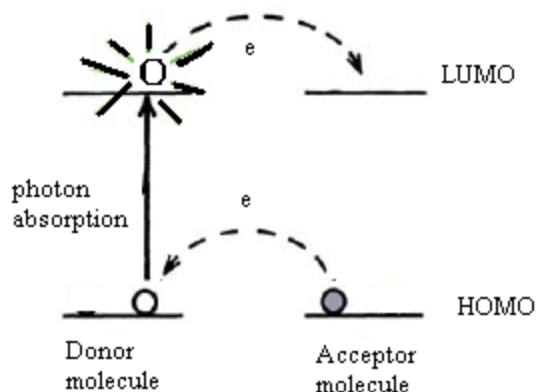


**Figure 2-4 Dexter interaction**

Quenching due to photo-induced electron transfer also results in electron exchange between donor molecule and acceptor molecule. But, in this case a nonfluorescent complex is formed between donor and acceptor molecule and the luminophore molecule can be donor or acceptor molecule.

For quenching by any of above mechanisms, both luminophore molecule and quencher molecule need to be in contact as electron clouds are strongly localized and quenching requires molecular contact at the van der Waals radii. In this case the distance dependence can be expressed as follows

$$Q(R) = A \exp[-\beta(r - r_c)] \quad (2-3)$$

where  $r$  is the center-to-center distance between fluorophore and quencher molecule, and  $r_c$  is the distance of closest approach at molecular contact.  $A$  and  $\beta$  are constants.

The collisional fluorescence quenching follows the of Stern-Volmer (SV) equation given bellow.

$$\frac{I_0}{I} = 1 + K_D [C_Q] \quad 2-4$$

Where  $I_0$  is the luminescence intensity in the absence of quencher molecules,  $I$  represents the quencher and  $[C_Q]$  is the concentration of quencher molecules.  $K_D$  is the Stern-Volmer constant.

In case of static quenching the dependence of  $I_0/I$  on quencher concentration  $[C_Q]$  is also linear similar to dynamic quenching. So the linear dependence of intensity ratio to quencher concentration does not confirm type of quenching. In many cases both static and dynamic quenching occur together. In such cases the Stern Volmer plot will have an upward curvature. The following modified form of SV equation represents both static and dynamic quenching together

$$\frac{I_0}{I} = (1 + K_D [C_Q])(1 + K_S [C_Q]) \quad 2-5$$

### 2.3. Metal Enhanced Luminescence

Though the phenomena of metal enhanced luminescence was known from the 1980s, the application and demonstration of metal enhanced luminescence is mostly new. Different applications of metal enhanced luminescence from different metallic nanoparticles have been successfully demonstrated by the Lakowicz and the Geddes groups<sup>1-3, 9-17</sup>.

Conducting metallic particles, colloids, or surfaces are known to significantly influence the emission of vicinal luminophores. The mechanism of metal enhanced fluorescence is still not fully understood. Geddes and coworkers suggested that metal nanoparticles influence the luminescence by three known mechanisms<sup>9</sup>. First, the

presence of nanoparticles close to the luminophores can create new nonradiative channels due to light absorption inside the metal or Förster energy transfer thus increasing the non-radiative decay rate.<sup>9</sup> Second, metallic nanoparticles are expected to increase the local incident field at molecular location, which enhance of the rate of excitation of luminophore molecules. The third mechanism is the increase of radiative decay rate of luminophore molecules in the presence of metal nanoparticles. Geddes and co-workers recently suggested a unified plasmon-fluorophore description for explaining the third mechanism. According to this theory, non-radiative energy transfer occurs from excited state of luminophore molecule to the surface plasmon resonance of vicinal metal nanostructures and luminophore induces mirror dipole in the metal. As a result surface plasmons radiate the photophysical properties of luminophore molecules, which adds up with the radiative emission of luminophore molecule rate thus increasing the overall radiative rate. This can be represented by following equation<sup>18</sup>

$$Q_m = (\Gamma + \Gamma_m)/(\Gamma + \Gamma_m + k_{nr}) \quad (2-6)$$

where  $\Gamma$  is the unmodified system radiative decay rate,  $\Gamma_m$  is metal-modified system radiative decay rate and  $k_{nr}$  is the non-radiative decay rate. In case of metal enhanced luminescence the lifetime decreases as a result photobleaching effect also reduces. The metal-modified lifetime can be expressed as following

$$\tau_m = 1/(\Gamma + \Gamma_m + k_{nr}) \quad (2-7)$$

Metallic platforms can enhance the radiative decay rate by coupling the emission of luminophores with surface plasmon resonance or scattering of nanoparticles. So it can be inferred that the influence of metal nanoparticles on luminescence is strongly

dependent on the surface plasmon resonance and the scattering efficiency of nanoparticles and the nanoparticles-luminophore separation distance.

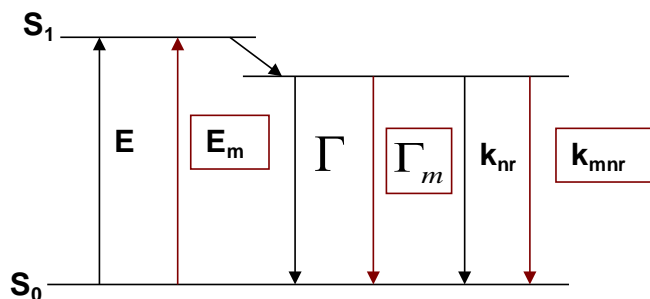


Figure 2-5 Modified Jablonski diagram in the presence of metal.<sup>9</sup>

### 2.3.1. Distance Dependence

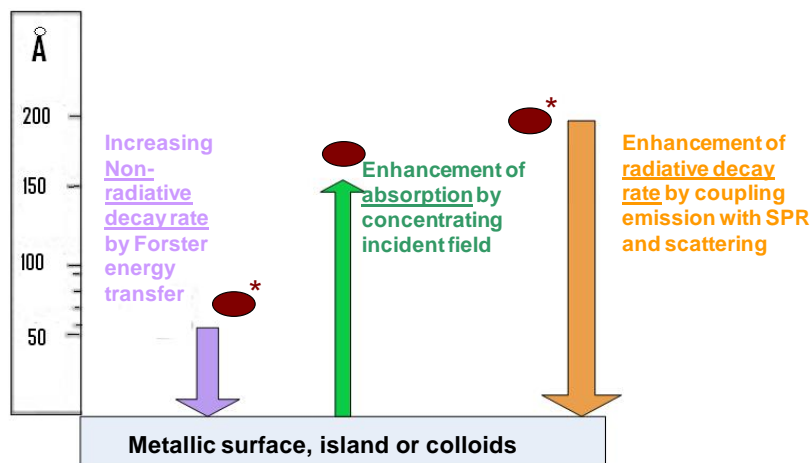


Figure 2-6 Distance dependence on the effect of metal on luminescence.<sup>9</sup>

If the probe molecules are very near to nanoparticles, luminescence emission from the probe molecules directly gets absorbed onto the surface of metallic nanoparticles and is strongly quenched. Similarly if the probes are too far from the nanoparticles platform effects of nanoparticles get diminished. Hence it is important to optimize the distance between the luminophores and nanoparticles. It has been reported in the literature that for the fluorophores positioned less than 50  $\text{\AA}$  from the surface the luminescence

intensity quenches with  $d^{-3}$  dependence<sup>9</sup>. Recently some research work has been devoted to study of distance-dependent metal enhanced luminescence<sup>13,19-23</sup>. The investigation of dependence of the luminescence enhancement on luminophore metal separation distance has been done using various spacer designs. Due to the extremely rough topology of metal surface, it is difficult to accurately control the distance. In some cases, the luminophores are first dispersed in polymer binder then by coating the different thickness film of the polymer containing luminophores the average distance between luminophore and metal surface is varied<sup>21,22</sup>. Using this kind of spacer one can only meaningfully study the effect of average distance as the luminophore is distributed throughout the polymer so the distance is not precisely controlled. To overcome this limitation in recent work luminophore molecules have been attached at a fixed distance using biological linker DNA as a spacer<sup>24</sup>. Alternating monolayers of biotinylated bovine serum albumin (BSA) and avidin is also used to investigate distance dependence<sup>19</sup>. Core-shell nanocomposites with metallic core and silica shell of various thickness have also been used for metal enhanced luminescence<sup>23</sup>. Here the silica shell acts as a spacer. The distance is optimized by investigating metal-core/ SiO<sub>2</sub>-spacer / luminophore system by varying shell thickness thus varying the distance.

### 2.3.2. Effect of Surface Plasmon Resonance of Metal Nanoparticles on Luminescence

Plasmons are quantized and collective oscillation of electron gas density. When the plasmons are confined to the surface and interact with the incident light, then these are called surface plasmons. They usually occur at the metal and dielectric interface. Surface plasmon resonance (SPR) of nanoparticles is dependent on several properties of

nanoparticles such as size, shape, composition, conductivity and inter-particles distance. The intensity of incident optical wave is enhanced in the near field of nanoparticles at the plasmon resonance wavelength. SPR of metallic nanoparticles play an important role in the luminescence enhancement. There are few studies reported in the literature on the relationship between SPR of nanoparticles and luminescence enhancement. Tam *et al.*<sup>25</sup> found that the enhancement is optimal when the nanoparticles plasmon resonance is tuned to the emission wavelength of the fluorophores. Recently, some theoretical and experimental studies have suggested that luminescence enhancement is highest when emission wavelength is red-shifted from the plasmon resonance<sup>24,26</sup>. In all these cases, emissive enhancement of luminophore is considered. It is still unknown what the effect of surface plasmon resonance of wavelength will be when the luminescence enhancement occurs due to absorption enhancement. Knowledge of the exact relationship between surface plasmon resonance and luminescence enhancement can lead us to designing efficient nanoparticle- luminophore assemblies with maximum luminescence. To obtain the information about the relation between surface plasmon resonance and luminescence enhancement, it is important to prepare nanoparticles with different surface plasmon resonance wavelengths.

### 2.3.3. Metal Nanoparticles Used for Metal Enhanced Luminescence and Their Synthesis

Silver nanoparticles have been known to enhance luminescence<sup>2-5,7-16,20-22,24,25,27-38</sup> due to their strong surface plasmon resonance. Metal enhanced luminescence has been studied for various silver nanostructures like silver colloids<sup>8</sup>, silver islands<sup>39</sup>, silver nanotriangles<sup>40</sup>, fractal like silvered surfaces<sup>41</sup> and silver nanorods<sup>5</sup>. Silver

nanostructures are reported to enhance the luminescence from six to 3000 fold<sup>42</sup>. Gold nanoparticles are known to both quench and enhance luminescence depending on the fluorophore-particle separation distance, molecular dipole orientation with respect to particle surface, and size of the nanoparticles.<sup>22,29,43</sup> Recently other metals such as copper<sup>17</sup>, aluminum<sup>44</sup>, nickel<sup>18</sup>, chromium<sup>45</sup> and zinc<sup>46</sup> have been reported to enhance luminescence<sup>17,44</sup>. However, the enhancement effect of these metal nanostructures is not as pronounced as for silver nanostructures due to higher ohmic losses. Zinc oxide (ZnO) nanorod platforms also have been reported to enhance luminescence intensity significantly, from commonly utilized fluorophores in immunoassays<sup>47-49</sup>. Zinc nanostructures enhance the luminescence emission but do not influence the excited state lifetimes of luminophores like other metallic nanoparticles. This implies that the enhanced luminescence observed near zinc nanostructures is mostly due to electric field enhancement effect<sup>50</sup>. Silver, gold and copper nanoparticles are used for metal enhanced luminescence mainly in the visible region where aluminum, zinc and chromium nanostructured films are shown to enhance luminescence of luminophore emitting in the ultraviolet and blue region<sup>8,17,29,44-46</sup>. Nickel nanoparticles can enhance the emission intensity of vicinal luminophores at broad wavelength range (500-800 nm)<sup>18</sup>. The selection of luminophores which can be enhanced by metal nanoparticles is limited by the choice of metals due to the effect of surface plasmon resonance spectra of metals on metal enhanced luminescence.

Different techniques have been suggested in the literature for the synthesis of anisotropic metal structures for applications in metal enhanced luminescence<sup>3,5,10,12,14-17,20-22,24,27,29,34,35,38-41,51</sup>. Some researchers followed the simple wet chemical synthesis

method for depositing spherical metal (mainly silver and gold) nanoparticles on glass slides. They prepare gold or silver colloids in suspension separately then 3-aminopropyl)-trimethoxysilane (APS) treated glass slides were immersed in the suspension to deposit colloidal nanoparticles on them<sup>29</sup>. Silver nanoparticles are also deposited on glass slides in a random fashion by using Tollens reaction<sup>21, 39</sup>. Photodeposition technique has been used to prepare patterned silver nanostructures to facilitate its application to microfluidic devices<sup>10</sup>. Shang *et al.* reported a simple and fast electrochemical technique to deposit silver nanostructure on planar substrates for luminescence enhancement application<sup>35</sup>. These silver nanostructures have relatively homogeneous morphology. Vapor deposition method has been also used for the deposition of both silver and gold nanostructures<sup>16,32,51</sup>. The morphology of vapor deposited nanostructures can easily be controlled by changing thickness and deposition rate. Vapor deposition method has recently been used for the preparation of copper nanostructures for its application to luminescence enhancement<sup>17</sup>.

Silver fractal-like nanostructures were prepared by passing a current between silver electrodes in deionized water and these are found to show better enhancement than spherical nanoparticles<sup>41</sup>. Similar to fractals, rods and triangles are also expected to show better enhancement<sup>5,40</sup>. Aslan *et al.* suggested simple wet chemical synthesis method for silver nanorod and triangular nanoplate deposition<sup>5,40</sup>. They suggested two methods for synthesis of nanorods<sup>5</sup>. In the first method, they deposited nanorods by immersing APS treated glass slides in silver nanorods solution. In the second method, spherical silver seeds were first chemically attached to the planar substrate then the substrate was immersed into a solution containing a cationic surfactant and silver ions where the silver

seeds were subsequently converted and grown into silver nanorods. They used the same method for the growth of silver triangular nanoplates<sup>40</sup>. But, by using these methods it is not possible to obtain well defined nicely arrayed structures of nanoparticles. For this, sophisticated lithography techniques are necessary. High-resolution lithography techniques such as E-beam lithography (EBL) have been used to produce highly regular cylindrical and triangular nanopatterns of gold for the application to luminescence enhancement of quantum dots<sup>22</sup>. Use of EBL allows tuning the surface plasmon resonance of nanoparticles over a wide range of wavelengths and may enable very strong enhancement. It can also help to localize the enhancement process with high spatial control, thus facilitating high emission intensity of luminescence. But the high cost and time involved limit applicability of the EBL technique. A relatively simpler and less expensive technique is nanosphere lithography developed by Van Duyne and co-workers<sup>52-54</sup> by which triangular or hexagonal nanostructures can be deposited.

#### 2.3.4. Metal Nanoparticles Quenched Luminescence

Metallic nanoparticles can quench or enhance luminescence depending on the fluorophore-particle separation distance, molecular dipole orientation with respect to particle surface, and size of the nanoparticles.<sup>22,29,43</sup> The presence of nanoparticles close to the luminophores can create new nonradiative channels due to light absorption inside the metal, quenching the emission of luminophores.<sup>30</sup> If the probe molecules are very close to the nanoparticles (typically less than 5 nm), luminescence emission is quenched due to Förster resonance energy transfer (FRET) from the excited state of the luminophore molecule (donor) to the surface plasmons of the metal nanoparticles

(acceptor). The FRET efficiency depends on the spectral overlap of the acceptor's absorption with the donor's emission, and sensitivity depends on the separation distance between acceptor and donor.<sup>55</sup> Quenching effect due to Förster energy transfer decreases with the cube of separation distance.<sup>56</sup> The relative orientation of luminophore's molecular dipole moment with respect to metallic nanoparticles surface decides the influence of metallic nanoparticles on radiative rate. The radiative rate is decreased for tangentially oriented dipole as the molecular dipole and the dipole induced on the metallic nanoparticles radiate out of phase. On the other hand, radiative rate is increased if the molecular dipole is oriented radially towards metallic nanoparticles.

Luminescence quenching by metal nanoparticles has been studied mostly using gold nanoparticles.<sup>43,55,57-59</sup> Dulkeith *et al.*<sup>55</sup> studied the quenching of the fluorescence of lissamine dye molecules attached to several sizes of gold nanoparticles. They investigated the effect of gold nanoparticles on both radiative and nonradiative decay rates responsible for quenching using time-resolved fluorescence experiments. Horimoto *et al.*<sup>58</sup> studied the effect of shape of gold nanoparticles on luminescence quenching and Ghosh *et al.*<sup>59</sup> studied the size dependence of luminescence quenching.

## 2.4. Theoretical Modeling

In the following sections, the basic concepts of theoretical approaches for the study of metal enhanced luminescence are presented. The effect of surface plasmon resonance of metal nanoparticles on metal enhanced luminescence is also studied theoretically in this work. Firstly, the calculation of the surface plasmon resonance spectra of alloy nanospheres is discussed, and then the calculation of quantum efficiency

modification of luminophore molecule in the presence of metal nanosphere is discussed in detail.

#### 2.4.1. Theoretical Investigation of Surface Plasmon Resonance of Nanoparticles

The surface plasmon resonance spectra of metal particles have been studied for many years<sup>60-65</sup>. Mie was the first to suggest a theory to study absorption spectra for spherical particles by solving Maxwell's equation. His theory is based on classical electrodynamics and by<sup>65</sup>.

Mie's theory is valid for any size particles but is limited to system where inter-particle separation distance is much larger than the wavelength of incident light. According to Mie's theory, the total transmittance through films containing spherical metal particles is

$$T_{tot} = \exp(-N\pi a^2 Q_{ext} d) \quad (2-8)$$

where N is number concentration of spheres per unit volume, a is sphere radius and d is film thickness.

The extinction coefficient is given as

$$Q_{ext} = \left( \frac{2}{x^2} \right) \sum_{n=1} (2n+1) \operatorname{Re}(a_n + b_n) \quad (2-9)$$

$$\text{where } x = \frac{2\pi a n_0}{\lambda} \quad (2-10)$$

$n_0$  is refractive index of the host medium and  $\lambda$  is wavelength of the incident light in vacuum.  $a_n$  and  $b_n$  are Mie scattering coefficients.

$$a_n = \frac{\Psi'_n(y)\Psi_n(x) - m\Psi_n(y)\Psi'_n(x)}{\Psi'_n(y)\zeta_n(x) - m\Psi_n(y)\zeta'_n(x)} \quad (2-11)$$

$$b_n = \frac{m\Psi'_n(y)\Psi_n(x) - \Psi_n(y)\Psi'_n(x)}{m\Psi'_n(y)\zeta_n(x) - \Psi_n(y)\zeta'_n(x)} \quad (2-12)$$

$$m = \frac{\tilde{n}_m}{n_0} \quad (2-13)$$

$$\tilde{n}_m = n_m + ik_m \quad (2-14)$$

$n_m$  is real refractive index of metal and  $k_m$  is absorption coefficient

$$y = \frac{2\pi a \tilde{n}_m}{\lambda} \quad (2-15)$$

$$\psi_n(z) = \left( \frac{z\pi}{2} \right)^{1/2} J_{n+1/2}(z) \quad (2-16)$$

$$\zeta_n(z) = \left( \frac{z\pi}{2} \right)^{1/2} H^{(2)}_{n+1/2}(z) \quad (2-17)$$

where  $J_n$  is the Bessel function and  $H_n^{(2)}$  is second-order Hankel function and  $Z$  is equal to  $x$  or  $y$ .

For calculating absorption spectra for spherical particles using Mie's theory, one needs to know the effective refractive index or dielectric constant for the system. The complex dielectric constant of metals can be calculated using Drude theory and Lorentz theory<sup>66</sup>. According to Drude's theory, the complex dielectric constants of a metal should be calculated using the following formula:

$$\varepsilon_f'(\omega) = 1 - \frac{\omega_p^2 \tau^2}{1 + \omega^2 \tau^2}, \quad \varepsilon_f''(\omega) = \frac{\omega_p^2 \tau}{\omega(1 + \omega^2 \tau^2)} \quad (2-18)$$

where  $\tau$  is the bulk relaxation time of electrons, and  $\omega$  is the frequency of light hitting the materials.  $\omega_p$  is plasma frequency of metal which can be calculated using the following formula:

$$\omega_p = \sqrt{ne^2 / \epsilon_0 m} \quad (2-19)$$

where  $n$  is electron density,  $e$  is the charge of electron and  $\epsilon_0$  is the vacuum permittivity and  $m$  is the mass of electrons.

For optical frequency  $\omega = 2\pi c/\lambda$  is very high so  $(\omega\tau)^2 \gg 1$  under this approximation, we can write

$$\epsilon_f'(\omega) \approx 1 - \frac{\omega_p^2}{\omega^2}, \quad \epsilon_f''(\omega) \approx \frac{\omega_p^2}{\omega^3 \tau} = \frac{\omega_p^2 \Gamma}{\omega^3} \quad (2-20)$$

But for metals, the Drude model alone is insufficient to predict dielectric constants as it implies that only plasma frequency dictates the dielectric constant. Though this works for some metals such as Zn, for most of the metals such as Ag and Cu, plasma frequency cannot by itself account for the dielectric constant. For these metals, the combined effects of the free-electrons (Drude model) and the bound d-electrons (Lorentz model) influence the reflectance properties of the metal. So, for these metals, the dielectric constant can be calculated by the formula

$$\epsilon_r = \epsilon_f + \epsilon_b \quad (2-21)$$

Where  $\epsilon_f$  is described by the Drude model ( $\omega_0 = 0$ ) (equation 1), and  $\epsilon_b$  is described by the Lorentz model. ( $\omega_0 = [E_F - E_d]/\hbar$ .)

$$\epsilon_b'(\omega) = 1 + \frac{4\pi ne^2}{m} \frac{(\omega_0^2 - \omega^2)}{(\omega_0^2 - \omega^2)^2 + \omega^2 / \tau^2} \quad (2-22)$$

$$\varepsilon_b''(\omega) = \frac{4\pi n e^2}{m} \frac{\omega / \tau}{(\omega_0^2 - \omega^2)^2 + \omega^2 / \tau^2} \quad (2-23)$$

There are many studies devoted to calculating effective dielectric constants for composite materials<sup>60,62,63,67-72</sup>. Maxwell–Garnett (M–G) and Bergman theory are mostly used to calculate effective dielectric constant for metal-dielectric composite<sup>60,62,63,67-72</sup>. These theories are valid for only spherical or ellipsoidal metal nanoparticles in dielectric media. These theories are developed considering the interaction of the external electric field with metal particles acting as interacting dipoles, with an effective polarizability given by the Drude relation, while the dielectric constant of the composite material was obtained through the Clausius–Mossotti relation<sup>60,72</sup>. M-G theory is based on the assumptions that the percentage of metal ( $f_a$ ) in dielectric media is very small and interparticle separation is very small compared to the wavelength of light. According to M-G theory, effective dielectric constant of metal-dielectric composite is given by<sup>72</sup>

$$\frac{\varepsilon_{eff} - \varepsilon_h}{\varepsilon_{eff} + k\varepsilon_h} = f_a \frac{\varepsilon_a - \varepsilon_h}{\varepsilon_a + k\varepsilon_h} \quad (2-24)$$

where  $\varepsilon_{eff}$  is effective dielectric constant of composite  $\varepsilon_h$  is dielectric constant of host matrix and  $\varepsilon_m$  is dielectric constant of metal.  $k$  is screening parameter determined by the shape as well as the orientation of the nanoparticles with respect to the external electric field.

For a random mixture of two dissimilar materials, the effective dielectric constant can be calculated using Bergman's theory<sup>60</sup>. According to this theory,  $\varepsilon_{eff}$  can be calculated using the following equation

$$f_a \frac{\varepsilon_a - \varepsilon_{eff}}{\varepsilon_a + k\varepsilon_{eff}} + (1 - f_a) \frac{\varepsilon_h - \varepsilon_{eff}}{\varepsilon_h + k\varepsilon_{eff}} = 0 \quad (2-25)$$

Gao *et al.* incorporated shape distribution of the components in both M–G and Bergman theory<sup>67</sup>. Garcia *et al.* developed a self-consistent technique based on mixing rules to predict the effective dielectric constants, and thus SPR spectra, for multi-component mixtures<sup>68</sup>. They presented a model to correct the imaginary component of dielectric component of metal to account for the enhanced rate of electron scattering due to size dependent effect for nanoparticles.<sup>68</sup>

$$\varepsilon_2 = \varepsilon_2^{bulk} \left( \frac{2d + v_F \tau_{bulk}}{2d} \right) \quad (2-26)$$

where,  $\varepsilon_2^{bulk}$  is imaginary component of dielectric constant of bulk metal,  $d$  is diameter of the nanoparticle,  $\tau_{bulk}$  is bulk relaxation time of the electron and  $v_F$  is the speed of the electrons close to the Fermi surface.

The above mentioned theories are only capable of predicting SPR spectra for spherical particles. With the development of computational resources there are some studies devoted to studying the problem of determining the scattering properties of particles of arbitrary shape and composition<sup>64,70,73-85</sup>. There are two approaches most used for calculating spectra for arbitrary shaped particles. The first approach is the discrete dipole approximations (DDA) method<sup>81-85</sup>. In this method, the particle is assumed to be composed of an equivalent volume filled by a lattice with a cubic cell whose sites are occupied by elementary scatterers electric dipoles. The number of dipoles considered decides the size of problem. Draine *et al.* have developed a FORTRAN program based on DDA approach to calculate scattering and absorption spectra for arbitrary shaped particles<sup>81</sup>. Another approach is approximation of  $N$  spheres where the random shaped

particle is assumed to be composed of number of elementary spheres<sup>78,86-88</sup>. The problem becomes more computationally intensive with the increase in the size of spheres. Both of these methods provide a good approximation about the SPR spectra for arbitrary shape particles in the region of forward scattering.

#### 2.4.2. Modeling of Plasmon Enhanced Luminescence

The intensity of the luminophore at the proximity of metal nanoparticles can be written as<sup>26,30</sup>:

$$I = C\eta(\omega_{flu})\sigma_{abs}(\omega_{abs})|K(\omega_{abs})|^2 I_{exc}(\omega_{abs})T \quad (2-27)$$

Here,  $\omega_{abs}$  is absorption frequency of the molecule,  $\omega_{flu}$  is emission frequency of the molecule,  $\eta(\omega_{flu})$  is quantum yield of emission,  $\sigma_{abs}(\omega_{abs})$  is absorption cross-section of the molecule in vacuum,  $I_{exc}(\omega_{abs})$  is exciting intensity in vacuum, C is a constant, T is integration time of the detector, and  $K(\omega_{abs})$  is local field vector.

From the above expression, it can be seen that by changing the local field for absorption  $k(\omega_{abs})$  and/or quantum yield  $\eta(\omega_{flu})$ , we can change the intensity of luminescence. The absorption rate of the luminophore can be enhanced by increasing both the absorption coefficient of the luminophore itself and the local field intensity. On the other hand, the quantum yield of the luminophore can be influenced by varying the radiative and non-radiative decay rates.

Kümmerlen *et al.*<sup>33</sup> suggested that the quantum efficiency enhancement factor Y (ratio of quantum efficiencies in the presence of metal nanoparticles and without nanoparticles) can be calculated using the following equation:

$$Y = |L(\omega_{abs})|^2 Z(\omega_{flu}) . \quad (2-28)$$

The first term represents the enhancement of local electric field at the excitation frequency ( $\omega_{abs}$ ). The second term describes the change in quantum efficiency due to radiative and non-radiative decay rate enhancements at the emission frequency ( $\omega_{flu}$ ). In the following sections calculation of both excitation enhancement factor and quantum efficiency enhancement factor are discussed.

#### 2.4.2.1 Calculation of Excitation Enhancement Factor

The integrated near-field scattering cross section ( $Q_{nf}$ ) at the excitation wavelength divided by the surface area of the spherical particle is a good measure of average  $|L(\omega_{abs})|^2$ <sup>89</sup>. The near-field scattering cross section can be calculated using the following equation<sup>90</sup>

$$Q_{nf} = 2 \frac{r^2}{a^2} \sum_{n=1}^{\infty} \left\{ |a_n|^2 \left[ (n+1) |h_{n-1}^{(1)}(ka)|^2 + n |h_{n+1}^{(1)}(ka)|^2 \right] + (2n+1) |b_n|^2 |h_n^{(1)}(ka)|^2 \right\} \quad (2-29)$$

where  $r$  is the distance from the center of the spherical nanoparticle and  $a$  is the radius of the nanoparticle.  $k = \sqrt{\epsilon_m} \omega / c$ ,  $\omega$  is the optical frequency (radian per second),  $\epsilon_m$  is the dielectric constant of the media and  $c$  is the velocity of light in vacuum. The term  $h_n^{(1)}$  is the spherical Henkel function of the first kind.  $a_n$  and  $b_n$  are well known scattering coefficients.

### 2.4.3. Modeling of Effect of Metal Sphere on Excited State Decay Rate

Quantum efficiency is calculated as the ratio of radiative decay rate to total decay rate. Spontaneous emission can be modified by resonant coupling with electromagnetic environment.<sup>91</sup> Both the model based on exact electrodynamic theory<sup>92-94</sup> and the Gersten-Nitzan (GN) model<sup>93,95,96</sup> can be used to provide insight into the influence of metal nanospheres on radiative and non-radiative decay rates of luminophore molecules at their close proximity, thus can be used to calculate luminescence quantum efficiency modification of a luminophore molecule in the presence of a noble metal nanosphere. In both of these models, and the luminophore molecule is modeled as a classical dipole with a dipole moment. Using these models, excited state decay rate for a dipole located outside the metallic sphere can be obtained for both radial and tangential orientation of dipoles with respect to metallic surface. In the following section the exact electrodynamic theory developed by Ruppins and by Kim *et al.* is discussed. After that the Gersten and Nitzan improved by Mertens *et al.*<sup>93,95,96</sup> is described.

#### 2.4.3.1 Exact Electrodynamic Theory

The radiative and non radiative decay rate of an excited luminophore molecule in the proximity of metallic nanosphere is modeled using classical electromagnetic theory.<sup>92,94</sup> The radiative decay rate is calculated considering the energy flow (Poynting vector) at large distances and nonradiative decay rate is obtained directly from ohmic losses inside the metallic sphere. In the presence of the metal sphere the total decay rate of emitter molecule in absorbing dielectric can be obtained by comparing the work done on a source in the presence of the sphere to the work done on the same source in the bulk

dielectric. The radiative decay rate in the presence of metallic sphere can be derived by comparing the energy flux through a surface enclosing both source dipole and sphere to the radiated power of source dipole in the bulk dielectric. The nonradiative decay rate is the difference between total decay rate and radiative decay rate.<sup>92,94</sup> The expressions for radiative decay rate ( $\Gamma_R$ ) and total decay rate ( $\Gamma_{tot}$ ) for a luminophore molecule derived from exact electrodynamics are given below.<sup>93,94</sup> These equations were developed considering luminophore molecule as dipole with dipole moment  $\mu$  placed at the distance  $d$  from metal nanosphere with radius  $a$  and dielectric constant  $\varepsilon = \varepsilon' + \varepsilon''$ . For radial orientation of dipole with respect to metallic sphere surface, the expressions are

$$\frac{\Gamma_{tot}^{\perp}}{\Gamma_R^{ref}} = 1 + \frac{3}{2} Re \sum_{l=1}^{\infty} (2l+1)l(l+1)b_l \left[ \frac{h_l^{(1)}(kr)}{kr} \right]^2 \quad (2-30)$$

$$\frac{\Gamma_R^{\perp}}{\Gamma_R^{ref}} = \frac{3}{2} \sum_{l=1}^{\infty} (2l+1)l(l+1)b_l \left[ \frac{j_l(kr) + b_l h_l^{(1)}(kr)}{kr} \right]^2 \quad (2-31)$$

For tangential orientation of dipole with respect to metallic sphere surface, the expressions are

$$\frac{\Gamma_{tot}^{\parallel}}{\Gamma_R^{ref}} = 1 + \frac{3}{2} Re \sum_{l=1}^{\infty} (l+1/2) \left\{ b_l \left[ \frac{\zeta_l'(kr)}{kr} \right]^2 + a_l [h_l^{(1)}(kr)]^2 \right\} \quad (2-32)$$

$$\frac{\Gamma_R^{\parallel}}{\Gamma_R^{ref}} = \frac{3}{4} \sum_{l=1}^{\infty} (2l+1) \left[ \left| j_l(kr) + a_l h_l^{(1)}(kr) \right|^2 + \left| \frac{\psi_l'(kr) + b_l \zeta_l'(kr)}{kr} \right|^2 \right] \quad (2-33)$$

where  $\Gamma_R^{ref}$  is the radiative decay rate for the dipole located in the nonabsorbing embedding medium in the absence of sphere,  $j_l$  and  $h_l$  are the ordinary spherical Bessel and Henkel functions,  $a_n$  and  $b_n$  are the Mie scattering coefficients of the sphere,  $r=a+d$ ,  $\psi_n(x) = xj_n(x)$ ,  $\zeta_n(x) = xh_n^{(1)}(x)$ ,  $k = \sqrt{\varepsilon_m} \omega/c$ ,  $\varepsilon_m$  is the dielectric constant of embedding medium,  $\omega$  is the optical frequency (rad/sec),  $c$  is the speed of light in

vacuum and  $l$  is the angular mode number, The derivatives of  $\psi_n$  and  $\zeta_n$  are derivatives to  $kr$ . In above expressions  $\Gamma_{tot}^\perp$  and  $\Gamma_{tot}^\parallel$  are total decay rate of emitter with 100% quantum efficiency in absence of sphere.

#### 2.4.3.2 Gersten-Nitzan (GN) Model

Using the model<sup>95</sup> the modifications of the radiative decay rate ( $\Gamma_R$ ) and total decay rate ( $\Gamma_{tot}$ ) of luminophore in proximity to metal nanoparticles can be calculated. According to this model excited state decay rate is calculated in two steps. First the quasistatic approximation is used to analyze the electromagnetic interaction between source dipole and metal sphere. The analysis is done based on electrostatics, as the retardation effect is neglected assuming the sizes of nanoparticles to be much smaller than the wavelength. Electrostatic potential is derived from the superposition of the source dipole potential and the induced multipoles of sphere. In the second step, radiative power is calculated from the effective dipole moment comprised of a vectorial superposition of the source dipole moment and the induced dipole moment. Radiative rate modification is obtained by normalizing to the power radiated by an uncoupled source with identical dipole moment. The nonradiative decay rate is calculated by calculating the power dissipated in the metal sphere by the Joule heating law. This model does not consider multipole radiation, and the interference between source dipole and induced dipole is neglected. The key advantage of model over exact electrodynamic theory is that model can be generalized to spheroidally shaped particles. Mertens *et al.*<sup>93,96</sup> introduced a correction factor for radiative reaction and dynamic depolarization in the GN model to modify the quasistatic polarizability of the nanoparticles to account the

retardation effect. This corrected model can accurately describe decay rate enhancement near larger nanoparticles (several 100 nanometers). In this model, the luminophore molecule is modeled as a classical dipole with dipole moment  $\mu$ . For the radial dipole orientation, the expressions for  $\Gamma_R$  and  $\Gamma_{tot}$  for the luminophore molecule positioned at distance  $d$  from the surface of sphere with radius  $a$  and dielectric constant  $\varepsilon = \varepsilon' + i\varepsilon''$  located in the medium of dielectric constant  $\varepsilon_m$  is as follows<sup>96</sup>

$$\frac{\Gamma_{tot}^\perp}{\Gamma_R^{ref}} = 1 + \frac{3}{4(ka)^3} \sum_l l(l+1) \operatorname{Im} \left\{ C_n \frac{\varepsilon - \varepsilon_m}{\varepsilon + \frac{l+1}{l} \varepsilon_m} \left( \frac{a}{a+d} \right)^{2l+4} \right\}; \quad (2-34)$$

$$\frac{\Gamma_R^\perp}{\Gamma_R^{ref}} = \left| 1 + 2C_1 \frac{\varepsilon - \varepsilon_m}{\varepsilon + 2\varepsilon_m} \left( \frac{a}{a+d} \right)^3 \right|^2. \quad (2-35)$$

For the tangential dipole orientation, the expressions for  $\Gamma_R$  and  $\Gamma_{tot}$  are

$$\frac{\Gamma_{tot}^{\parallel}}{\Gamma_R^{ref}} = 1 + \frac{3}{2(ka)^3} \sum_l (l+1)^2 \operatorname{Im} \left\{ C_l \frac{\varepsilon - \varepsilon_m}{\varepsilon + \frac{l+1}{l} \varepsilon_m} \left( \frac{a}{a+d} \right)^{2l+4} \right\}; \quad (2-36)$$

$$\frac{\Gamma_R^{\parallel}}{\Gamma_R^{ref}} = \left| 1 - C_1 \frac{\varepsilon - \varepsilon_m}{\varepsilon + 2\varepsilon_m} \left( \frac{a}{a+d} \right)^3 \right|^2. \quad (2-37)$$

In the above expressions,  $l$  is the angular mode number, and  $\Gamma_R^{ref}$  is the radiative decay rate of luminophore in the absence of nanoparticles.  $C_1$  is the correction factor for radiation dumping and dynamic depolarization:

$$C_1 = \frac{1}{1 - \frac{ik^3\alpha}{6\pi} - \frac{k^2\alpha}{4\pi a}} \quad (2-38)$$

$\alpha$  is the quasistatic polarizability,

$$\alpha = 4\pi a^3 \frac{\varepsilon - \varepsilon_m}{\varepsilon + 2\varepsilon_m}. \quad (2-39)$$

For  $l \neq 1$ ,  $C_l$  is assumed to be 1.

In the present work, a quantum efficiency enhancement factor is calculated using the corrected GN model as suggested by Mertens *et al.*<sup>93</sup>. For better representation of experimental conditions, the source dipole orientation was averaged over all solid angles. This was achieved by averaging the results for decay rates obtained for radial and tangential orientations.

## 2.5. Bimetallic Nanoparticles

Bimetallic nanoparticles constituting various combinations of noble metals have been attracting much attention as they can combine the advantages of two pure metals. They offer many unique properties and advantages over pure nanoparticles, for example, enhanced magnetism<sup>97</sup>, electrochemical properties<sup>98</sup>, catalytic activity<sup>99</sup> and fine tuning of optical properties<sup>100,101</sup>. In this study, the unique plasmonic property of alloy nanoparticles is of main interest. In the following sections a brief overview of plasmonic property of different bimetallic nanoparticles and their synthesis methods are given.

### 2.5.1. Plasmonic Properties

Plasmonic properties of nanoparticles are significantly influenced by dielectric constant, shape, size and structure of nanoparticles. Tunable surface plasmon resonance in wide range is the most interesting property of bimetallic nanoparticles. Bimetallic

nanoparticles can be core-shell, random and separated structures depending on their synthesis method. Dielectric constant can be changed by alloying or mixing two metals with different dielectric constant. Mie scattering theory predicts that surface plasmon resonance of core-shell nanoparticles can be shifted between ultraviolet to mid-infrared range. For Ag-Cu alloy nanoparticles surface plasmon resonance can be shifted from near infrared to ultraviolet region by changing only one experimental condition-annealing temperature. This shifting is due to reorientation of Ag and Cu atoms in Ag-Cu nanoparticles.<sup>101,102</sup> For Ag-Pt hollow nanoparticles, SPR can be redshifted by increasing Pt concentration and once the Pt. concentration exceed a maximum value the peak broadens and is blue-shifted and eventually diminished. For Ag- Au alloy nanoparticles SPR can be shifted by changing the composition.

Theoretical modeling of SPR spectra of alloy nanoparticles requires knowledge of their dielectric constants.<sup>61,103,104</sup> Dielectric constants for alloy nanoparticles of different compositions are not available and have to be calculated using semi-empirical models such as those based on Drude theory and experimental data for pure, bulk metals.<sup>105</sup> In most of this existing work, semi-empirical models are developed based on the assumption of homogeneous distribution of metallic atoms in their alloys. For the core shell structure the dielectric constant is given as follows:

$$\varepsilon_{core}(\omega, R) = \varepsilon_{exp}(\omega) + \frac{\omega_p^2}{\omega^2 + i\omega\Gamma_\infty} - \frac{\omega_p^2}{\omega^2 + i\omega(\Gamma_\infty + \Gamma_{core})} \quad (2-40)$$

$$\varepsilon_{shell}(\omega, R) = \varepsilon_{exp}(\omega) + \frac{\omega_p^2}{\omega^2 + i\omega\Gamma_\infty} - \frac{\omega_p^2}{\omega^2 + i\omega(\Gamma_\infty + \Gamma_{shell})} \quad (2-41)$$

where  $\Gamma_{core}$  and  $\Gamma_{shell}$  are the surface-induced contributions to the damping.

For alloy nanoparticles, the dielectric constant is obtained by modeling the nanoparticle as homogeneous material with physical properties obtained by averaging those of pure metals. Plasmonic frequency at bimetallic surface is given by

$$\omega = \left[ \frac{1}{2} (\omega_p^2 + \omega_p'^2) \right]^{1/2} \quad (2-42)$$

where  $\omega_p$  is the classical plasma frequency and  $\omega_p'$  represents a different plasma frequency based off the dielectric constant at the interface.

### 2.5.2. Synthesis

Bimetallic nanoparticles have been synthesized as alloys or core shell structures using different synthesis methods like solution synthesis and physical deposition techniques. In most cases, alloy nanoparticles are synthesized in solution phase. Simultaneous reduction of corresponding metal ions or metal complexes results in the formation of alloy nanoparticles. Coreduction of two metal ions also results in bimetallic nanoparticles. Bimetallic nanoparticles can also be prepared by laser radiation or heat treatment of mixtures of monometallic nanoparticles. In all cases, the morphology and the size of bimetallic nanoparticles can be controlled by controlling experimental parameters like temperature, ratio of precursors and stabilizing agents. Bimetallic nanoparticles synthesized by different methods will have different plasmonic characteristics as the atomic distribution in bimetallic nanoparticles is different for different synthesis method.

### 2.5.2.1 Synthesis of Bimetallic Alloy Nanoparticles

Coreduction is one of the important methods used for synthesizing alloy nanoparticles. Bimetallic colloids are prepared by chemical reduction, photochemical reduction or thermal decomposition.

Au-Ag alloy nanoparticles were produced by the coreduction of Ag salt ( $\text{AgNO}_3$ ) and gold salt ( $\text{HAuCl}_4$ ) by reducing agent like sodium citrate. For these Au-Ag nanoparticles, the SPR peak blue-shifted by increasing percentage of silver in alloy nanoparticles. This resonance shift is suggested to be due to a modification in the band structure of these alloys, which is different from pure metal.<sup>106</sup> Various composition Ag/Au alloy nanoparticles were synthesized in microemulsion by the co-reduction of  $\text{HAuCl}_4$  and  $\text{AgNO}_3$  with hydrazine.<sup>107</sup> Au-Cu colloidal nanoparticles were synthesized in methanol by coreducing  $\text{HAuCl}_4$  and  $\text{CuCl}_2$  by  $\text{NaBH}_4$  and the polymer poly(N-vinyl-2-pyrrolidone) (PVP) is used as stabilizing agent.<sup>108</sup> Au-Cu nanoparticles were also prepared in reverse micelles by coreduction of their salts.<sup>109</sup> Silver-copper alloy nanoparticles were synthesized via the polyol process by coreducing  $\text{AgNO}_3$  and  $\text{Cu}(\text{HCOO})_2 \cdot \text{H}_2\text{O}$ .<sup>110</sup>

Several other interesting methods are suggested in the literature for synthesizing bimetallic alloy nanoparticles. Smetana *et al.* suggested low temperature digestive ripening procedure for synthesizing Ag-Au and Au-Cu nanoparticles<sup>111</sup>. In this method bimetallic alloy nanoparticles are synthesized by heating colloids of two different pure metal nanoparticles in the presence of alkanethiol under reflux. Haverkamp *et al.* suggested a biosynthetic method using plant *Brassica juncea* for synthesizing Ag-Au and Au-Cu alloy nanoparticles.<sup>112</sup> Bimetallic nanoparticles of Ag, Cu and Au are prepared by

photo chemical reduction of their salts using in ethanol by UV irradiation using benzoin.<sup>113</sup> Bimetallic nanoparticles of Co and Cu were prepared by successive reduction of their salts in hydrazine solution with the aid of sonication.<sup>114</sup>

Physical vapor deposition is also frequently used for the synthesis of bimetallic nanoparticles. Simultaneous sputter deposition of Ag and Au in ionic liquids were used to synthesize Au-Ag nanoparticles in solution.<sup>115</sup> Co-sputtering deposition was also used to deposit bimetallic nanoparticles like Ag-Cu and a Ag-Au on solid substrate.<sup>116,117</sup> Pulsed laser deposition was used to synthesize bimetallic Ag-Cu nanoparticles on glass substrate<sup>102</sup>.

## 2.6. Characterization Techniques

In the present work, first type of characterization techniques, are used to characterize the nanoparticles like imaging, composition analysis and their optical property measurement. The second type of characterization techniques are used to study the fluorescence property of luminophores. Characterization tools used in this work are briefly described below.

### 2.6.1. Transmission Electron Microscopy (TEM)

Transmission electron microscopy is the most useful imaging techniques for nanoparticles (specifically for less than 10 nm size). In case of transmission electron microscopy (TEM) a beam of electrons is transmitted through a electronically transparent specimen interacting with the atoms to produce one image. Due to the small de Broglie

wavelength of electron image with atomic resolution is possible to be captured by TEM. For TEM image sample is required to be dispersed on TEM grids (for example carbon coated copper grid, molybdenum grid).

### 2.6.2. Scanning Electron Microscopy (SEM)

In case of SEM the area of the sample to be analyzed is targeted by a narrowly focused electron beam which can be swept across the surface of specimen to form image or may target one place only to analyze particular position. The image is produced due to the interaction of the electron beam with atoms at or near the surface of the samples. SEM can also produce very high resolution image (1 to 5 nm). SEM specimens required to be conductive at the surface to avoid accumulation of electrostatic charge at the surface. For imaging non-conductive specimens, the specimen surface is coated with a thin film of conducting metal like gold.

### 2.6.3. Atomic Force Microscopy (AFM)

AFM is a high resolution scanning probe microscopy technique in which a microcantilever with a sharp tip is used to scan the surface of sample. The advantage of AFM over SEM is that AFM can provide true three dimensional image of a sample and does not require sample to be conductive and can operate in ambient air or even in liquid. However AFM can only provide image of area an order of 10 micrometers.

#### 2.6.4. Energy Dispersive X-ray Spectroscopy (EDS)

Chemical characterization and elemental analysis of nanometer scale particles can be done by EDS. This analysis is based on the analysis of x-rays emitted by the matter in response to interaction between electromagnetic radiation and matter. As each element has unique atomic structure and can emit unique x-rays, elemental composition can be detected by analyzing the emitted x-rays. EDS for compositional characterization of nanoparticles is usually integrated with TEM or SEM.

#### 2.6.5. UV-Vis Absorption Spectroscopy

In this technique a beam of light of wavelengths in the visible and ultraviolet region passes through the specimen and its intensity before and after interacting of sample is measured to determine the light transmitted through or absorbed by the sample. Absorption peaks can be correlated to the surface plasmon resonance peak of nanoparticles and can be indicative of the type of bonds in a given molecule.

#### 2.6.6. Fluorescence Microscopy

In this microscopy method images are taken based on the fluorescence property of samples. The sample is usually first tagged with a fluorescent molecule and excited by light with excitation energy required for the fluorophores. The fluorescence emission from the specimen is collected through an emission filter to separate the emitted light from the illumination light. A single fluorophore can be imaged at a time.

### 2.6.7. Fluorescence Spectroscopy

In this type of fluorescence electromagnetic spectroscopy fluorescence from sample is analyzed. The sample is excited using a particular wavelength of light and emitted fluorescence emission of a lower energy is detected.

## Chapter 3 - Measurement of Oxygen Diffusivity and Permeability in Polymers Using Fluorescence Microscopy

### 3.1. Introduction

The emission intensity of some luminophores is quenched in the presence of oxygen molecules. Applications of luminescence quenching by oxygen range from the measurement of pressure distribution of air on the wing of an aircraft using pressure sensitive paint<sup>118</sup> to the study of oxygen diffusion properties in polymers<sup>119,120,121</sup> and biological membrane<sup>122</sup>. For measuring diffusion coefficients of oxygen in polymers using luminescence quenching methods, the luminophore is typically dispersed directly in the polymer and the change in the average oxygen concentration is monitored by studying the average intensity change or life-time change of the luminophore using a spectrofluorometer<sup>4,119,120,121</sup>. In these methods, initially, the polymer is equilibrated at a particular concentration of oxygen. Then, the polymer containing luminophore is exposed to higher (“diffusion in”) or lower (“diffusion out”) concentrations of oxygen. The average intensity or lifetime change in the polymer is monitored using a spectrofluorometer for determining diffusion coefficients. In most cases<sup>120,123,126,141</sup> for ease of calibration, the luminophore dispersed in the polymer is assumed to behave ideally and follow the linear Stern-Volmer equation<sup>124</sup>

$$I_0 / I - 1 = K_{sv} p_{O_2}$$

3-1

where  $I_0$  is the luminescence intensity in the absence of oxygen,  $K_{sv}$  is the Stern-Volmer (SV) constant and  $p_{O_2}$  is the partial pressure of oxygen over the polymer.

Yekta *et al.*<sup>4</sup> were the first to develop an appropriate model combining Fick's law of diffusion and the linear Stern-Volmer (SV) equation to extract diffusion coefficients from experimental data for both "diffusion in" and "diffusion out" experiments. This model was based on the concept that the intensity change of the luminophore corresponds to the average oxygen concentration within the polymer. Additionally, this model is based on the assumption of uniform excitation of luminophore throughout the film, which is only true for low optical density films. This model was extensively used later to find diffusion coefficients for different luminophore-containing polymer films which follow the linear SV equation<sup>120,123,126,141,4</sup>

However, typically, it is difficult to fabricate polymer supported luminescence oxygen sensors that exhibit linear response. Luminophore molecules in liquid solvents almost always observe the linearity of SV plot as the temporal fluctuations of the microenvironment are much faster than the luminescence decay rate. As a result all the luminophore molecules are expected to be in the same environment on average. In case of luminophore molecules dispersed in a polymer matrix, different luminescent molecules experience different influences from their respective microenvironments due to micron-scale irregularities in polymer morphology. Heterogeneity of luminescence sensors, which occurs due to incompatibility of the polymer and luminophore, is typically the reason for nonlinearity in response. Influence from unquenchable emission from aggregates of luminophore and also sometimes the unquenchable background emission

may contribute to nonlinear behavior. Influence of dual or continuous gas sorption in the polymer may also result in nonlinearity<sup>130-135</sup>. The exact reasons for the non-linearity are debatable. Several models were developed for describing the nonlinear response of the sensors such as the multi-site quenching model (two-site model)<sup>5</sup> the nonlinear solubility model<sup>134</sup> and a model based on Forster-type energy transfer.<sup>130,131</sup>

For determining the diffusion coefficient, it is quite complicated and computationally demanding to combine the nonlinear SV models with Fick's law. Kneas *et al.*<sup>138</sup> suggested an improved computational scheme in which they combined a nonlinear gas solubility model for SV equation with Fick's law based diffusion model and solved it numerically to interpret the data of oxygen diffusion in polymers. This model can be applied to high optical density films, and the assumption of uniform concentration of O<sub>2</sub> is not required. However, this model can only be applied to cases where the luminophore is uniformly distributed throughout the film. Schappacher and Hartmann<sup>137</sup> were first to develop a partial analytical model to eliminate numerical complexity. They combined the two component model (two sites model) which is mathematically equivalent to the dual sorption model for nonlinear quenching with Ficks law based diffusion model. Unfortunately, the two-site model is not always sufficient to explain non-linear behavior of real sensors and consideration of existence of dye molecules in more than two sites (with their own quenching constants) is necessary.<sup>134</sup> Analytical models combining a multi-site model with Fick's law subjected to different sets of boundary conditions are complicated to derive.

Some researchers<sup>138-140</sup> used fluorescence microscopy to study the heterogeneity in luminescence sensors (luminophore molecules dispersed in a polymer matrix).

Fluorescence microscopy allowed them to study the SV response of the luminescence sensors with microscopic spatial resolution. They reported homogeneous regions of sensors show better response to oxygen concentration than regions where the dye is aggregated.

In the present work, we used conventional fluorescence microscopy to study the heterogeneities of luminescence sensors and their spatial response to O<sub>2</sub> concentration and extend its application for the measurement of oxygen diffusion properties of polymers. We investigated spatial distribution of SV response of the sensor at different oxygen concentrations at the microscopic level. Fluorescence microscopy allowed us to identify relatively homogeneous regions. The responses from these regions were analyzed to calculate the oxygen diffusion coefficients. This method avoids the complexity of including nonlinear SV equations in the analytical models. This method also eliminates the need for generating calibration curves for non-linear SV responses for each and every sensor before using it for diffusion measurement. In the present study, we used the film-on-sensor method and the accumulation-in-volume techniques<sup>141</sup> to investigate oxygen diffusion behavior in a variety of polymers, including transparent and opaque films and those containing additives.

We first chose Platinum octaethylporphyrin (PtOEP) as a probe for luminescent sensor. However, this type of the sensor was not very photostable under continuous illumination of fluorescence microscope. PtOEP showed decrease of intensity during the initial illumination period. This is attributed to the photobleaching and leaching of PtOEP from polymer matrix and deterioration of matrix itself. Hence, we replaced PtOEP with more photostable luminophore platinum(II) *meso*-tetrakis-

(pentafluorophenyl)porphyrin (PtTFPP). The difference in photostability between PtOEP and PtTFPP is mainly attributed to the differences between their side functional groups, ethyl for PtOEP and perfluorophenyl for PtTFPP. The photostability of sensors mainly depends on the size and rigidity of the side functional group and resulting efficiencies of collision with oxygen molecules. While, ethyl groups can easily move, the fluorophenyl group is large and rigid to oxidative/reductive attack. As a result, PtTFPP molecules are less reactive toward photo-oxidation/reduction.<sup>142</sup> PtTFPP also has high emission quantum efficiency and a moderately long emission lifetime which is required for application in luminescence sensing. We used polystyrene as polymer matrix for the sensor.<sup>142</sup>

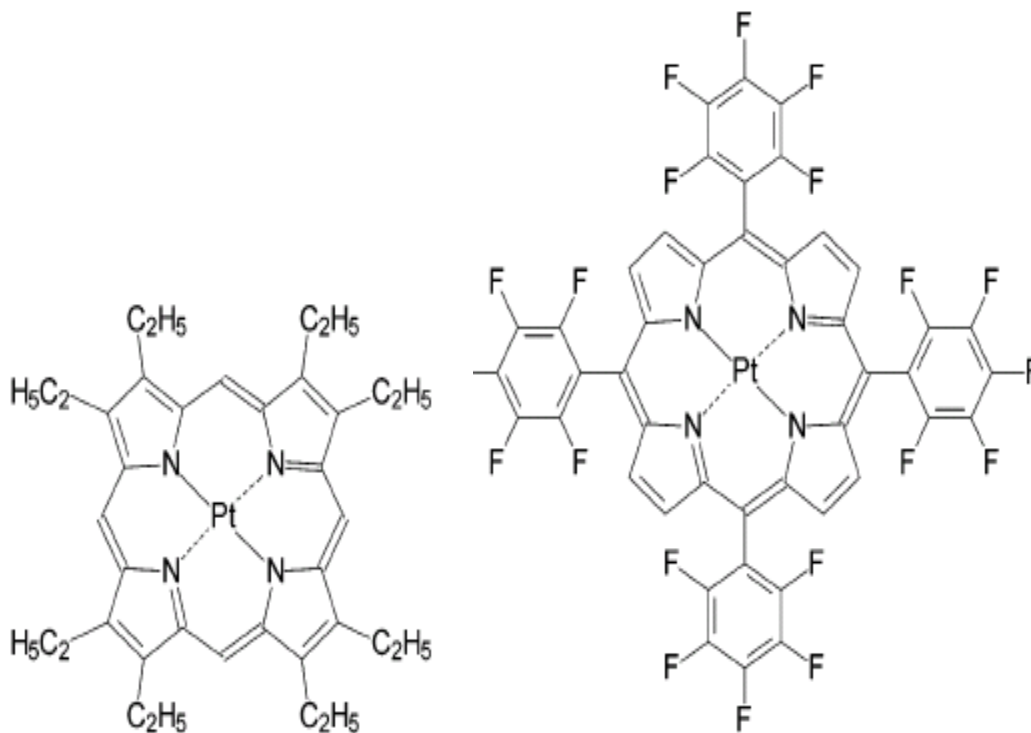


**Figure 3-1 Molecular Structure of PtOEP and PtTFPP<sup>142</sup>**

Oxygen diffusion and permeation coefficients in Teflon and Polydimethylsiloxane (PDMS) were measured to validate our new technique. Then, the technique was used to measure the diffusion coefficient of a high-performance (HP) silicone elastomer (black polymer) and PDMS containing different weight percentages of zeolite (Molecular sieves 5 Å). It should be noted that, in this case the polymer films for which oxygen diffusion properties are measured are different from the polymer used to prepare the oxygen sensors. We combined the SV equation with Fick's law of diffusion to extract the diffusion coefficients from experimental data.

### 3.2. Materials and Methods

#### 3.2.1. Sensor Films and Polymers

The oxygen sensing material was prepared by dispersing  $1.3283 \times 10^{-4}$  mols of luminophore platinum tetrakis (pentafluorophenyl) porphyrin (PtTFPP) (Frontier Scientific, Inc., Logan UT) in 1 liter solution of polystyrene (Sigma-Aldrich; Milwaukee, WI, USA, Avg.  $M_w$  280,000 by GPC)/toluene ( $0.24 \text{ g}\cdot\text{l}^{-1}$ ). This solution was spin-coated on 19 mm diameter glass, cut from 1 mm thick microscope slides. Before coating, the glass slides were cleaned with acetone, methanol, isopropanol and deionized water, then dried with nitrogen gas. Then, the glass pieces were put in an air plasma cleaner (Harrick PDC-32G) for 15 minutes at 6.8 watts power setting. For coating, the spin speed was maintained at 1,000 rpm for 60 seconds for each sensor. Lastly, the sensor pieces were cured at room temperature for 1 hour and at  $120^\circ \text{C}$  for 5 hours. An ellipsometer

(Rudolph AutoELIII) was used to measure the thickness of the resulting sensor (polystyrene containing PtTFPP dye) film.

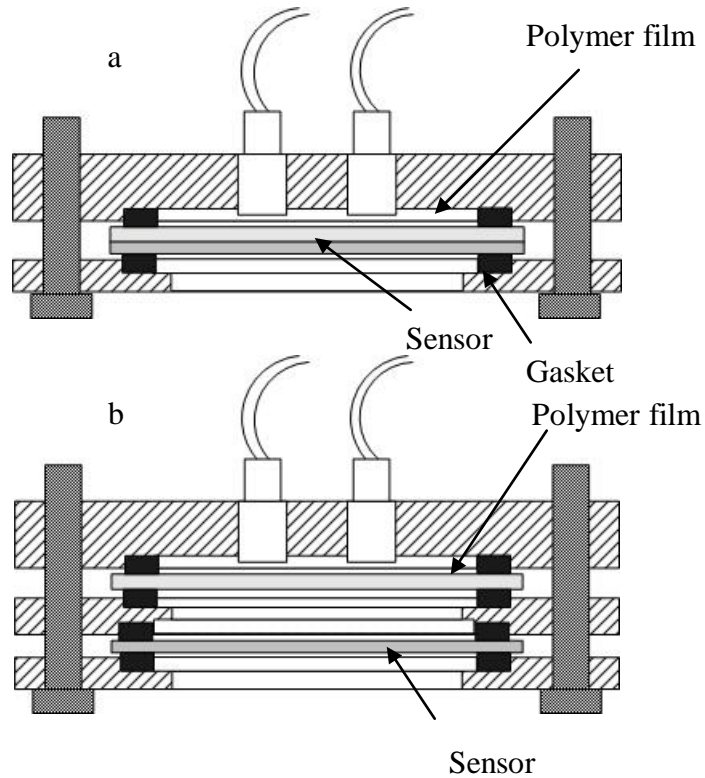


**Figure 3-2 Schematic diagrams of diffusion cells for (a) film on sensor experiment and (b) accumulation in volume experiment.**

The oxygen diffusion and permeation coefficients were measured for different polymers with known and unknown diffusion properties to establish this technique. The permeation and diffusion coefficients of DuPont's Teflon FEP film were measured using accumulation-in-volume technique. The thickness of Teflon film was 25  $\mu\text{m}$ . The diffusion coefficients of Sylgard 184, a common poly(dimethyl-siloxane) (PDMS) and 3-6265 HP polymer (silicone elastomer) (Dow Corning) were measured by film-on-sensor technique. For PDMS, the pre-polymer mixture was first degassed under vacuum (30 in. Hg vacuum) for 30 minutes to remove any air bubbles in the mixture, after which, it was

directly drop cast on a 19 mm luminescence sensor and was pressed against a PET film to smooth the surface. After this, the PDMS film was cured at 120 °C for 1 hour. The 3-6265 HP polymer film was also prepared by drop casting and was cured at 100° C for 35 minutes. For the HP polymer, a Teflon film was used to smooth the surface.

To disperse zeolite ( $\text{Ca}_{1/n}\text{Na}_{12-2n}[(\text{AlO}_2)_{12}(\text{SiO}_2)_{12}] \cdot x\text{H}_2\text{O}$ , molecular sieves, 5 Å, beads, 4-8 mesh, Sigma Aldrich, Milwaukee, WI) into PDMS, the zeolite was first ball-milled in SPEX 8000 Mixer/Mill with 8 mm stainless steel balls for 2 hours. After milling, the average size of zeolite obtained was 50 µm. As the zeolites are hydrophilic, these were dried at 150 °C for 1 hour before preparation of the film. Different weight percentages of zeolite (up to 30%) were dispersed in PDMS solution. These solutions were cast on the sensors, and cured for 1 hour at 120 °C.

### 3.2.2. Instrumentation and Software

The Leica DMI 4000b inverted research fluorescence microscope equipped with Leica DFC340 FX CCD Camera was used in this study. Fluorescence microscopy was carried out with a red filter set (Chroma Technology 41005, HQ535/50x exciter and HQ645/75m emitter). The images of luminescence sensors were taken using a 10X objective (Leica 11506228 HI Plan 10x/0.25 NA, 12.0 mm W.D) and the light source used was a tungsten halogen lamp (100W and 12V). Image Pro-plus version 6 with Scope Pro version 6 (Media Cybernetics, Inc) was used for acquiring and analyzing images. Using Scope-pro, the illumination intensity of light source can be controlled from 0% to 100% of the total intensity and also the shutter can be controlled. The specimen was only exposed to illumination while taking images and the lamp intensity

was maintained at 10% of its total intensity. A macro was written to only have the shutter open while acquiring an image. The exposure time for acquiring each image was set to be 300 milliseconds for each image. Thus, photobleaching of the luminescence sensors was minimized.

For observing the SV behavior of a sensor, it was placed in a chamber that was flushed with different concentrations of oxygen. A circular glass disc with sensor film coated on it was mounted on a stainless steel chamber using a viton gasket (the sensor film was on the inside surface of glass disc) to make the chamber airtight. An air pump was used to control the air pressure inside the chamber. The pressure inside the chamber was monitored using a MKS Baratron pressure transducer (315 BA-1000) with 1000 Torr range with a digital read out. Assuming the concentration of O<sub>2</sub> in air is 21%, the partial pressure of O<sub>2</sub> inside the chamber was determined from the total pressure indicated by the pressure transducer. Images of the sensor were acquired at different concentrations of oxygen and analyzed for intensity using Image Pro-plus.

Stainless steel cells (Figures 3.2) were constructed for diffusion measurements of the polymers such that the volume of the downstream chamber was  $2.68 \times 10^{-7} m^3$  and the exposed surface area of the polymer film was  $5.85 \times 10^{-5} m^2$ . The diffusion cell was painted flat black to prevent reflection of light.

For the accumulation-in-volume experiment, there were two chambers in the diffusion cells (Figure 3.2 (a)). The polymer films were placed between the chambers using viton gaskets to prevent leakage. The upstream chamber of the polymer film was continuously flushed with nitrogen (“diffusion out experiment”). In the downstream chamber, the luminescence sensor was mounted with the viton gasket at the opposite side

of the polymer film. In this experimental configuration, the concentration of oxygen inside the volume of the downstream chamber changes with commensurate change in the luminescence intensity of the sensor. For the film-on-sensor experiment, the polymer film attached to a sensor was placed in a stainless steel chamber (Figure 3.2(b)). In all cases, the polymer film was first equilibrated with air; then exposed to a zero concentration of oxygen. Luminescence intensity changes measured the changes in oxygen concentration at the sensor/polymer film boundary in the film-on-sensor technique. To test the cells for leakage, the same experiment was done with the cell by replacing polymer film with a stainless steel plate. The diffusion cell was mounted on the stage of the microscope in such a way that the sensor faced the illumination source and detector. The image of the sensor film was captured through the 1 mm thick glass on which the sensor film was coated. To ensure that the sensor film was within the focal length of the objective, a new insert for the microscope stage was designed. The insert has a 2 mm deep recession to lower the sample placed on it towards the objective.

### 3.2.3. Image Analysis

The images were processed in the following way to minimize the error in intensity measurement. The intensity of the dark current image, acquired while the camera shutter was closed, was subtracted from the intensity of every raw image to correct the images for the dark current noise of the camera. The ambient lighting image of polystyrene film, which was acquired at the same ambient light at which raw images were taken, was subtracted from the images. The mean intensities of different regions of the corrected images were measured using the intensity track function of Image Pro-plus.

### 3.3. Analytical Models

In this work, diffusion of gas through the polymer material is described by Fick's law, which in one dimension is written in the form

$$\frac{\partial C}{\partial t} = D \left( \frac{\partial^2 C}{\partial x^2} \right) \quad 3-2$$

for constant diffusion coefficient  $D$ . Here,  $C(x,t)$  is the concentration at position  $x$  at time  $t$  and  $D$  is the diffusion coefficient of the gas in the material. The solution of this equation depends on the boundary conditions at the edges of the film. We combined the linear SV equation with the diffusion model to extract the diffusion and permeation coefficients from the experimental data. A nonlinear least square fitting method is used to fit the model to intensity vs. time data to extract the diffusion coefficient.

#### 3.3.1. Film Separated from The Luminescent Sensor by A Small Volume (Accumulation-in-volume Case)

In this case, two different models were used to analyze the data.

##### 3.3.1.1 Fick's Equation Combined with The SV Equation

When the top side (thickness,  $x=0$  at the film surface) of a polymer surface is continuously (time,  $t \geq 0$ ) maintained at zero concentration of  $O_2$  gas (flushed with pure  $N_2$  gas) and at  $t < 0$  the polymer film is kept at equilibrium with air (partial pressure of oxygen  $p_{air}$  and the concentration of oxygen  $C_{i0}$ ), the experimental condition satisfies following boundary conditions:

$$C = C_{10} = Sp_{air} \quad 0 \leq x \leq l \quad t < 0 \quad 3-3$$

$$C = C_0 = 0 \quad x = 0 \quad t \geq 0 \quad 3-4$$

$$D \frac{\partial C}{\partial x} + \frac{1}{\eta} \frac{\partial C}{\partial t} = 0 \quad x = l \quad t \geq 0 \quad 3-5$$

where  $\eta = 0.278 \frac{STAl}{V_{cell}}$  where  $S$  is the solubility of gas in polymer,  $T$  is the temperature,  $A$

is the surface area of polymer,  $C$  is concentration of oxygen,  $l$  is the total thickness of polymer and  $V_{cell}$  is the volume of the cell. For these boundary conditions, Fick's second law has been solved previously<sup>143</sup> :

$$\frac{P_{air} - P}{P_{air}} = 1 - \sum_k \frac{2(\beta_k^2 + \eta^2) \sin \beta_k \frac{x}{l}}{\beta_k [\beta_k^2 + \eta^2 + \eta]} e^{-\frac{D\beta_k^2 t}{l^2}} \quad 3-6$$

where  $\beta_k$  are the roots of:

$$\beta \tan \beta = \eta \quad 3-7$$

Combining equation 3-6 with the SV equation, the luminescence intensity change due to change in oxygen concentration is related to the time.

$$\left( \frac{I_{air}}{I} - 1 \right) = \left( \frac{I_{air}}{I_0} - 1 \right) \left( 1 - \sum_k \frac{2(\beta_k^2 + \eta^2) \sin \beta_k \frac{x}{l}}{\beta_k [\beta_k^2 + \eta^2 + \eta]} e^{-\frac{D\beta_k^2 t}{l^2}} \right) \quad 3-8$$

where  $I_{air}$  and  $I_0$  are the luminescence intensity at the  $O_2$  concentration in air and in the absence of  $O_2$  respectively.

This model is fitted with experimental data using a nonlinear least square method to extract both  $\eta$  and  $D$  values. Then, solubility of gas is calculated from  $\eta$ . Thus, we

can extract information about both diffusion and permeation coefficients by fitting this model to data.

### 3.3.1.2 Quasi-steady State Model

In this model, time is divided into arbitrary small intervals and the diffusion process is considered to be at steady state for each interval. Steady state differential material balance for each interval is combined with Fick's law for diffusion to determine the accumulation of gas into the cell. The amount of oxygen accumulated into the diffusion cell at the end of time interval  $i$  is:

$$M_i = M_{i-1} + F_i \cdot A \cdot \Delta t_i = M_{i-1} + P \cdot \frac{p_{0,t} - p_{h,i-1}}{h} \cdot A \cdot (t_i - t_{i-1}) \quad (3-9)$$

$F$  is the molar flux,  $A$  is the surface area of membrane exposed to gas,  $P$  is the permeation coefficient,  $p_0$  and  $p_h$  are partial pressures of gas outside and inside of the diffusion cell, respectively, and  $V$  is the diffusion cell volume. Partial pressure inside the cell for each time interval may be calculated from the ideal gas law:

$$p_{h,i} = \frac{M_i}{V} R.T \quad (3-10)$$

where  $R$  is universal gas constant and  $T$  is the absolute temperature.

The quasi-steady state model coupled with the SV equation can be used to predict the permeation coefficient data. Luminescence intensity at any time interval  $t_i$ ,

$$I_0 / I_i - 1 = k_{sv} p_{h,i} \quad (3-11)$$

The inside partial pressure of oxygen for each interval ( $p_{h,i}$ ) is calculated from equation

3-10. Eliminating  $k_{sv}$  from equation 3-11 it can be written as,

$$1 - I_{air} / I_i = \frac{(1 - I_{air} / I_0)(p_{air} - p_{h,i})}{P_{air}} \quad (3-12)$$

From this model, only the permeability coefficient can be extracted from experimental data using equations 3-9, 3-10 and 3-12.

### 3.3.2. Film-on-sensor Model

For the film on sensor experiment, where the upstream of the film is maintained under pure nitrogen exposure, with the film initially conditioned with air, the solution for Fick's second law is given by Crank<sup>144</sup>

$$\frac{C_0 - C}{C_0 - C_1} = \left( 1 - \frac{4}{\pi} \sum_{n=0}^{\infty} \frac{(-1)^n}{2n+1} \exp\left(\frac{-D(2n+1)^2 \pi^2 t}{4l^2}\right) \right) \quad (3-13)$$

Here, the initial concentration  $C_0$  is the concentration of oxygen in air and

$C_1 = 0$  (pure nitrogen)

Combining this equation with the SV model, the final equation can be written as <sup>141</sup>

$$\frac{\left(\frac{I_{air}}{I} - 1\right)}{\left(\frac{I_{air}}{I_0} - 1\right)} = \left( 1 - \frac{4}{\pi} \sum_{n=0}^{\infty} \frac{(-1)^n}{2n+1} \exp\left(\frac{-D(2n+1)^2 \pi^2 t}{4l^2}\right) \right) \quad (3-14)$$

## 3.4. Results and Discussion

In the following section the characterization of sensors and diffusion measurement are discussed.

### 3.4.1. Characterization of Sensors

As mentioned in the experimental section, thin film of polystyrene containing PtTFPP dye coated on glass slide was used as a sensor. The diffusion coefficient of oxygen in polystyrene was reported in the literature to be of the order of  $10^{-11} \text{ m}^2/\text{sec}$ .<sup>138</sup> Ellipsometry of sensor film indicated that average thickness of the sensor film was 300 nm to 400 nm. So the diffusion time of oxygen in the sensor film is negligible. Photobleaching of the sensor was studied by exposing the sensor to continuous illumination for 10 minutes. It was found that the intensity decreased by only 3% of the initial intensity. As the total exposure time during experiment was approximately 1 minute, photobleaching was minimal during the experiment so the photobleaching effect was neglected. In the present work, we performed “diffusion out” experiments to distinguish the quenching effect from the photobleaching effect.

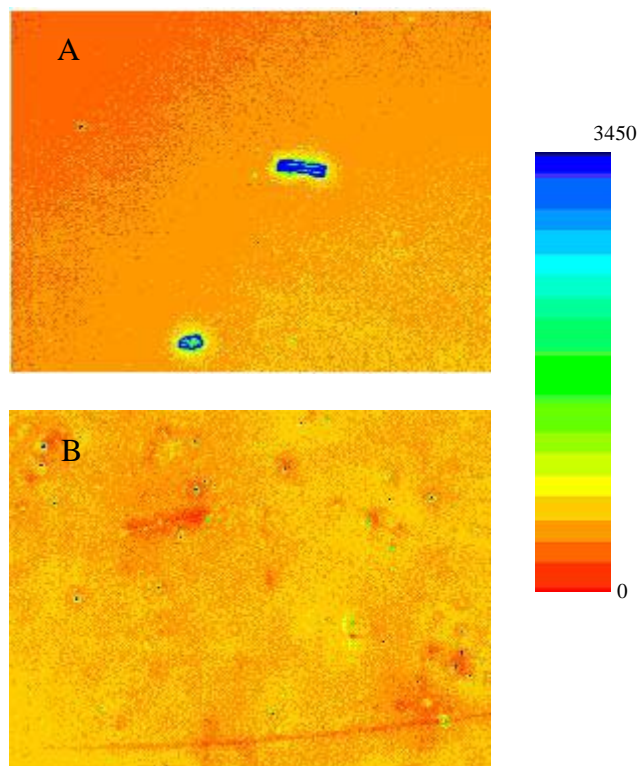


**Figure 3-3 Pseudo-colored microscopic fluorescence intensity images (1.64 mm X 2.19 mm) of two luminescence sensors (PtTFPP/PS).**

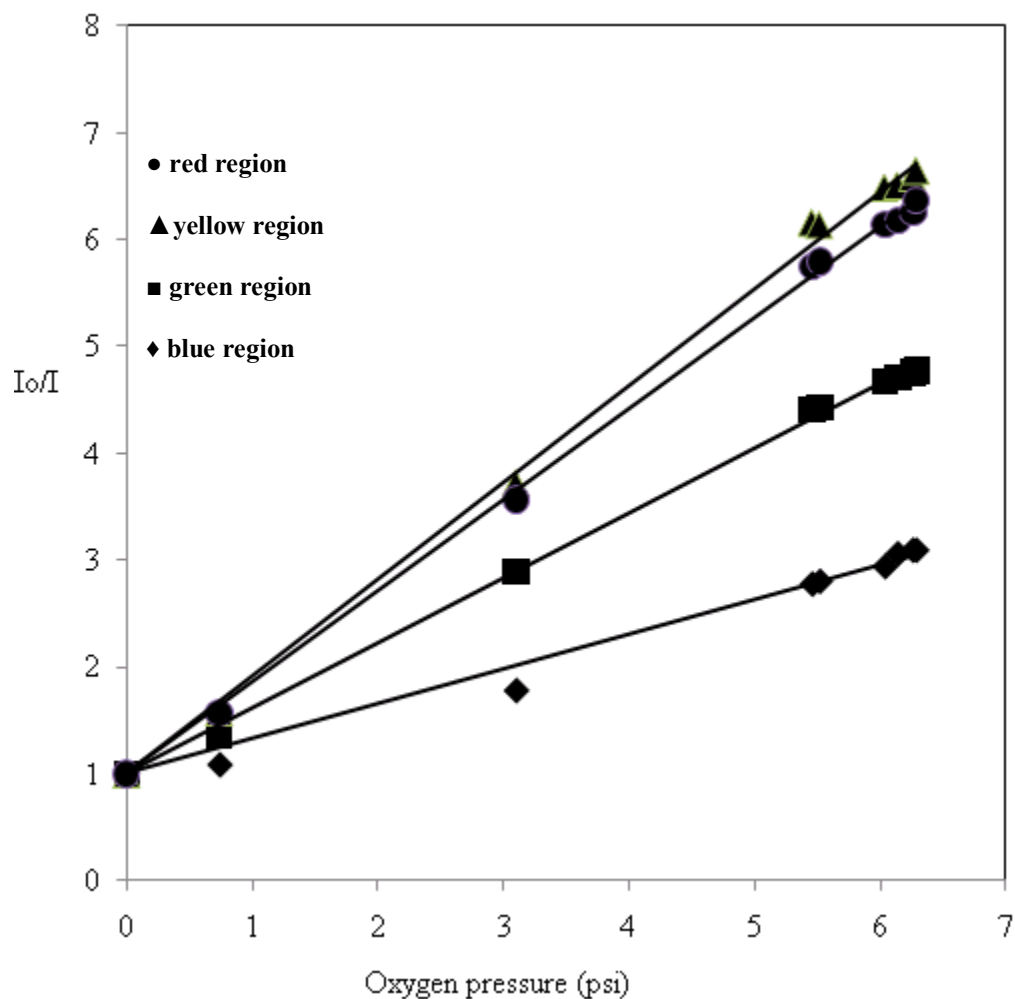


Figure 3-4 SV plot for different regions of sensor a.

Spatial distribution of the SV response of fluorophore PtTFPP in the luminescence sensor was determined using a conventional fluorescence microscope. Figure 3.A and 3.B show pseudo-colored 100X magnified images of portions of two sensors at 0% oxygen concentration. Both of these sensors were fabricated by the same procedure and at the same time. From these images, it can be seen that there are some bright fluorescent spots (blue and green regions) in a nearly homogeneous background region (red and yellow regions) of low intensity. This shows the dye was not homogeneously dispersed in the sensor. Bright spots (blue) are due to micro-crystal

formation of the luminophore due to its incompatibility with the polystyrene matrix. The image here represents a 1.64 mm × 2.19 mm region of the sensor. Four different regions of these two images were investigated for their SV response at nine different oxygen pressures. These regions were chosen from four different intensity regions. SV constants calculated for different regions of the two images (A and B) are given in Table 3.1. Coefficient of determination  $R^2$  gives information about the goodness of fit of the data to the SV model.

**Table 3-1 SV constants of different microscopic regions of luminescence sensors**

Region	Sensor A		Sensor B		After 30 minutes photobleaching of Sensor A	
	$K_{SV}$ (psi <sup>-1</sup> )	$R^2$	$K_{SV}$ (psi <sup>-1</sup> )	$R^2$	$K_{SV}$ (psi <sup>-1</sup> )	$R^2$
1 (Red)	0.85	0.999	0.46	0.961	0.77	0.998
2 (yellow)	0.90	0.998	0.53	0.974	0.79	0.998
3 (Green)	0.61	0.999	0.45	0.967	0.54	0.996
4 (Blue)	0.33	0.986	0.03	0.527	0.25	0.958

It can be seen from these results (Table 3-1) that SV constants and coefficient of determination values for both sensors are higher for nearly homogeneous low-intensity regions (red and yellow) in comparison to high-intensity microcrystal-rich regions. Past investigations on heterogeneity of different sensors also have shown that microcrystalline areas show greater intensity but less quenching by oxygen.<sup>139</sup> In contrast, Bedlek-Anslow *et al.*<sup>140</sup> observed the opposite effect for their sensors (tris(4,7-diphenyl-1,10-phenanthroline)ruthenium(II) dichloride (Rudpp) dispersed in PDMS. They found that regions where the luminophore was aggregated showed less intensity due to self quenching.

Though both the sensors were prepared by the same procedure, comparing the SV response from sensor A and sensor B, it can be seen that the SV response of sensor B is poorer. SV constants and  $R^2$  value are higher for lower intensity region of image A ( $K_{SV} = 0.9 \text{ psi}^{-1}$   $R^2 = 0.998$ ) in comparison to image B ( $K_{SV} = 0.53 \text{ psi}^{-1}$   $R^2 = 0.974$ ). This can be attributed to the fact that the microscopic visual heterogeneity exhibited by image B is more than that of image A. Therefore, it is possible to obtain high  $K_{SV}$  values with good linearity depending on the sensor and as well as the image field chosen to study.

The effect of photobleaching on SV response of sensor A was also studied. The sensor was first exposed to continuous illumination for 30 minutes then SV analyses of the same regions of image A were done again. The results are summarized in Table 3-1. Photobleaching of fluorophore adversely affects its oxygen sensing performance. Specifically, photobleaching effect is very much pronounced in the microcrystalline region. In case of diffusion measurement experiments, the specimens were only exposed to illumination while taking images. The exposure time for acquiring each image was set to be 300 milliseconds. Total exposure time of sample to light while taking data was less than about 1 minute. Thus, photobleaching of the luminescence sensors can be considered negligible.

Based on the SV analysis of different regions of the sensor film, the intensity change of regions which follow the linearity of SV equation and have high SV constants were examined for evaluation of oxygen diffusion parameters.

### 3.4.2. Measurement of Diffusion Using Fluorescence Microscopy

Diffusion coefficient of oxygen in Teflon was measured using the accumulation-in-volume technique. The Teflon film was placed in the diffusion cell and a tight seal was achieved. The polymer film was first equilibrated with air, then the upstream section of the polymer was flushed with pure nitrogen and images of the sensor mounted in the downstream cell were taken simultaneously. A background image was acquired for the same experimental setup without luminophore. These images were processed according to the procedure described in the experimental section. Responses from the nearly homogeneous low-intensity regions (which follow linear SV equation with high SV constants) of the sensor were analyzed for intensity change with respect to time as oxygen diffused out from the downstream chamber across the polymer film. Partitioning of the signal to select areas of uniform intensity was performed using microscope-software-generated intensity-heterogeneity information. This approach allowed for identification of regions of uniform intensity. The sizes of the different regions for which mean intensities were measured were in the range of  $0.04 \text{ mm}^2$  to  $0.25 \text{ mm}^2$  and at least 5 different regions of the sensor were sampled to represent the bulk response. Figure 3-4 shows intensity ratio vs time data for Teflon. The solid line represents the best fit to the diffusion model (Equation 3-8).

Using the quasi steady state model, an approximate value of the permeation coefficient of oxygen in polymer film was first determined. Then, the diffusion model (Equation 3-8) was fit to experimental data to extract both permeation and diffusion coefficients.

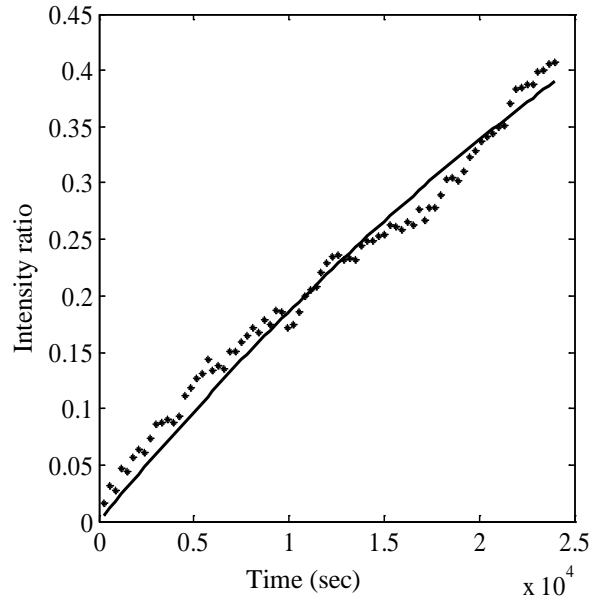


**Figure 3-5 Experimental and fitted data for the 0.025 mm thick Teflon film (\* experimental data – fitted data from model).**

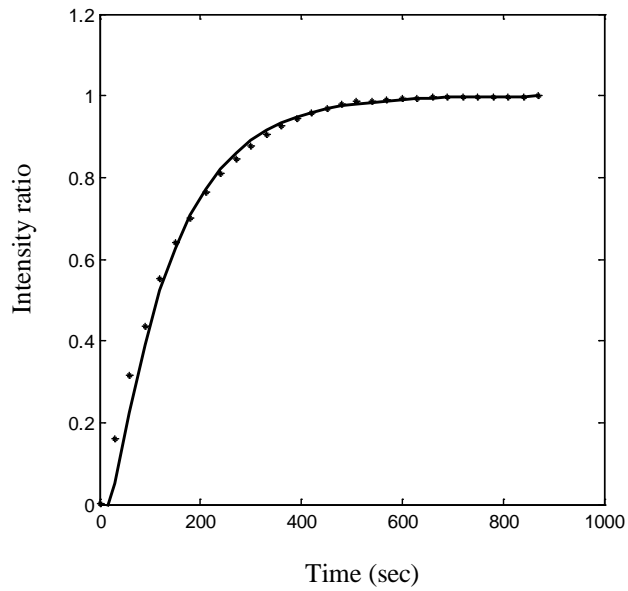


**Figure 3-6 Experimental and fitted data (\* experimental data – fitted data from model) for the 0.8 mm thick PDMS film.**

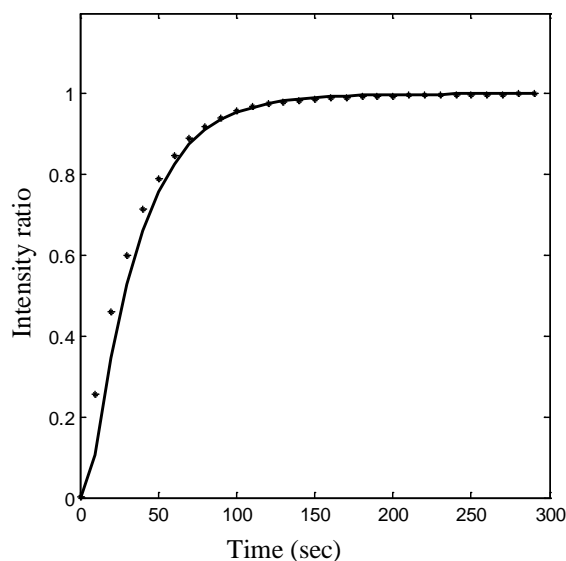


**Figure 3-7 Experimental and fitted data (\* experimental data – fitted data from model) for 0.55 mm 3-6265 HP polymer film (silicone elastomer)**

This experiment was repeated on the same polymer film as well as on different films of the same polymer. For Teflon, from the measurement on the same film, the diffusion and permeation coefficients were  $1.99 \text{ E-}11 \pm 2.2 \text{ E-}13$  and  $2.7\text{e-}10 \pm 7.1\text{E-}12$   $\text{mol}\cdot\text{m}^2/\text{m}^3\text{sec}\cdot\text{atm}$ , respectively, and from measurements on different films, the extracted diffusion and permeation coefficients were  $1.7 \text{ E-}11 \pm 4.99\text{E-}12$   $\text{m}^2/\text{sec}$  and  $2.68\text{E-}10 \pm 9.7\text{E-}11$   $\text{mol}\cdot\text{m}^2/\text{m}^3\text{sec}\cdot\text{atm}$ , respectively. The uncertainty in the data measured for the same film may be due to photobleaching, and the uncertainty in data measured from different films is due to differences in the polymer samples and sensors. These data compare with reported values of  $1.84 \times 10^{-11}$   $\text{m}^2/\text{sec}$  and  $1.62 \times 10^{-10}$   $\text{mol}\cdot\text{m}^2/\text{m}^3\text{sec}\cdot\text{atm}$ <sup>145</sup>. These values for oxygen diffusion and permeation coefficients in Teflon were measured by Koros *et al.*<sup>145</sup> in the temperature range of 40 to 85<sup>0</sup> C using a continuous permeation cell connected with a gas chromatograph. The differences between literature reported values and the values reported by us, could have arisen from

differences in the polymer samples, and from the slight extrapolation in temperature from the literature reported values to our experimental temperature of 25 °C. In our lab, electrochemical sensor technique was used by other researchers to measure the oxygen permeation coefficient in same Teflon sample.<sup>146</sup> The value for permeation coefficient in the Teflon sample obtained using electrochemical sensor technique is comparable with value obtained using the fluorescence method presented here.

**Table 3-2 Oxygen diffusion coefficients for various polymers**

Polymer type	Zeolite weight percentage (%)	Diffusion coefficient (m <sup>2</sup> /sec)
3-6265 HP polymer (silicone elastomer).	0.0	4.52e-09 ± 8.71E-10
PDMS	0.0	9.75E-10 ± 1.25e-10
PDMS + zeolite	2.5	1.09E-09 ± 1.09E-10
PDMS + zeolite	10.0	1.17E-09 ± 1.47E-11
PDMS + zeolite	20.0	1.23E-09 ± 4.04E-11
PDMS + zeolite	30.0	1.32E-09 ± 5.29E-11

For the accumulation-in-volume technique, there are two challenges involved. One is to control the leakage of gas from the diffusion cell, and the second is the longer time associated with the experiment. Leakages were managed by constructing the diffusion cell from stainless steel and using viton gaskets. No change of intensity of sensor was noticed during the control experiment, indicating no leakage. Inherently, accumulation-in-volume technique is a longer experiment. For thicker films with smaller diffusion coefficients, it can take significant experimental times of several months to see any significant change of oxygen concentration in the downstream cell. Though by reducing the volume of the cell experimental time can be reduced, it is still a lengthier experiment and the technique is suitable for thin films only.

In film-on-sensor technique, the test polymer was directly cast onto the sensor. In this case also, the polymer surface which was initially in equilibrium with air was flushed with nitrogen. As oxygen diffused out from the polymer its concentration change at the polymer sensor boundary was sensed by luminophore. The thickness of polymer film on sensor was measured using digital Vernier calipers. The thicknesses of PDMS and the HP polymer films were in the range of 0.6 to 0.8 mm, and 0.48 to 0.50 mm, respectively. Experimental data were fitted with the diffusion model (Equation 3-14) to determine the diffusion coefficient of oxygen in the polymer. This method was first used to measure the diffusion coefficient of oxygen in PDMS for validating the technique. Experimental data and the fitted diffusion model are shown in Figure 3.5. Oxygen diffusion coefficient for pure PDMS obtained from this fit is  $9.75\text{E-}10 \pm 1.24\text{E-}10 \text{ m}^2/\text{sec}$ . This is within the range of values reported in the literature ( $0.54 \times 10^{-9}$  to  $3.4 \times 10^{-9} \text{ m}^2/\text{sec}$ ).<sup>147</sup>

As the sensor was monitored in the reflectance mode using an inverted fluorescence microscope, it is also possible to measure diffusion coefficient of oxygen in opaque films using this technique. To demonstrate this, we measured the oxygen diffusion coefficient in 3-6265 HP polymer, which is black in color. The diffusion model fit the experimental data well (Figure 3.6). New data for this polymer are given in Table 3.2 which is of the same order of magnitude as known data for silicone elastomers. As for the film-on-sensor experiment, the polymer film attached to a sensor was placed in a stainless steel chamber and the surface of polymer film, initially equilibrated with air, was continuously flushed with  $\text{N}_2$ . There is a small, unavoidable time difference between manual opening of  $\text{N}_2$  cylinder to flush the chamber with  $\text{N}_2$  and the start of

image acquisition. This may be the reason for the poor fit at short time shown in Figures 3.5 and 3.6.

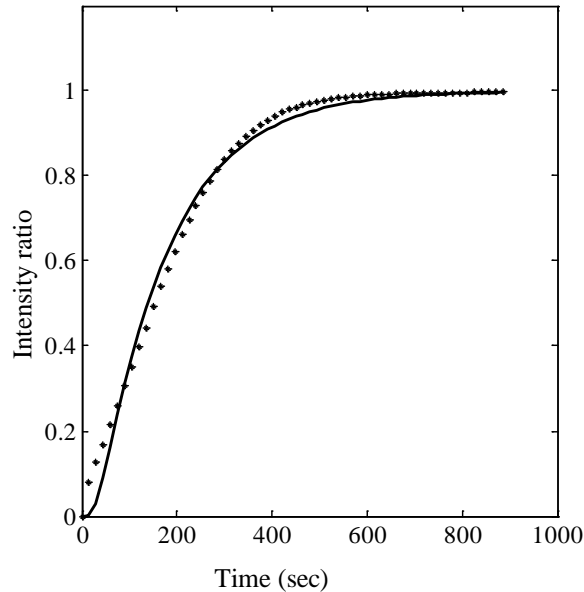


**Figure 3-8 Data for the 0.65 mm thick PDMS film containing 10% zeolite (\* experimental data – fitted data from model).**

Fluorescence microscopy was also used for the measurement of oxygen diffusion in PDMS containing zeolite. The diffusion coefficients of oxygen in the polymer containing zeolites were measured using the film-on-sensor technique. It is shown in Figure 3.7 that the oxygen desorption experimental data fit well to the Fickian diffusion model as described by eqn. 3-17. However, the presence of zeolite causes a little deviation between the simulated data and experimental data. Zeolites in polymers affect gas diffusion in several ways<sup>148</sup>. These particles can adsorb gas molecules and act as gas reservoirs, thus decreasing the diffusion coefficient and affecting dynamic behavior of the membranes cast from these polymer composites. Zeolites can hinder or can facilitate gas

diffusion depending on the kinetic diameter of gas molecules<sup>147</sup>. Gas diffusion in polymers also depends on available free volume of the polymers. Free volume of the polymer at the proximity of polymer-zeolite boundary can either be reduced or enhanced<sup>149</sup>. On the other hand, the packing density in unoccupied zones may increase which may cause the decrease in oxygen diffusion coefficient. As the zeolite content increases, the void spaces formed around the zeolite also increase enhancing the oxygen permeability. On the other hand, the packing density in unoccupied zones may increase, which may decrease the oxygen diffusion coefficient.

In contrast to the previous cases reported in literature<sup>150</sup>, timelag in the diffusion in this case was reduced. Diffusion coefficients for zeolite free and zeolite filled PDMS are given in Table 3.2. Diffusion coefficients reduce as the weight percentage of zeolite increases in PDMS. This trend agrees with literature<sup>148</sup>. Hence, it can be concluded that presence of zeolite in PDMS introduces more free volume as well as more pores which enhance oxygen (kinetic diameter 3.46 Å) diffusion and decrease timelag.

Applicability of the methods developed here is subjected to the condition that no component present in the polymer interferes with the response of the fluorescence sensor to oxygen concentration. For example this method was not successful to measure oxygen diffusion coefficient in epoxy polymer, as this polymer shows fluorescent property in the emission wavelength range of PtTFPP dye.

### 3.5. Conclusions

We demonstrated the application of conventional fluorescence microscopy in studying the relationship between microscopic heterogeneity and the nonlinearity of SV

responses of luminescence sensors. Based on this study, a fluorescence microscopy technique was developed to measure diffusion and permeation coefficients of oxygen in polymers. Using this microscopy technique, microscopic level SV responses of heterogeneous sensors are measurable. This technique allows for the distinction of the responses of background region (nearly homogeneous regions) from the regions of aggregated luminophores. As the nearly homogeneous regions show better response to oxygen concentration and follow the linearity of the SV equation, by studying the response of these, one can eliminate the complexity of combining the nonlinear SV equation with a diffusion model. We also found that the sensors prepared by the same procedure behave differently in term of SV responses. The sensors with less visual microscopic heterogeneity show better responses. Fluorescence microscopy allowed us to visually inspect and chose better sensors for the application. With this method, diffusion data for Teflon and PDMS were obtained, which compared well with literature values. New data for 3-6265 HP polymer (a silicone elastomer) and PDMS containing zeolite are of an expected order of magnitude with comparable materials.

We developed a new, simple quasi-steady model for describing diffusion phenomena for the accumulation-in-volume technique. Photostable luminophore is essential for this technique to be successful. Minimizing photobleaching of the luminophore is a challenge for this method that was overcome by shuttering techniques. The methods developed here can be applied for measuring oxygen diffusion properties in polymers ranging from transparent to opaque, subjected to the condition that no component is present in the polymer which interferes with the response of the sensor to oxygen concentration. The technique is suitable for polymers that cannot be cast into

free standing films, and yields reliable data in reasonable experimental timeframes. This method is also suitable for polymer composites. We expect this fluorescence microscopy technique will be very useful for measuring  $O_2$  diffusion coefficient in biological samples simultaneously with imaging these samples.

## Chapter 4 - Effect of Ag-Cu Alloy Nanoparticle Composition on Luminescence Enhancement/Quenching

### 4.1. Introduction

The emission of luminophores is significantly influenced in close proximity of conducting metallic nanostructures. Using nanoparticle platforms, it is possible to increase the quantum yield of weakly luminescent probes. This increase results from a modification of the radiative decay rate by coupling the emission with surface plasmon resonance (SPR), and by coupling emission at far field with nanoparticle scattering. These nanostructures can also enhance the excitation intensity experienced by vicinal luminophore molecules by enhancing the incident optical field by increasing the local field at the molecular location.<sup>11,28,39,151</sup> The presence of nanoparticles close to the luminophores can create new nonradiative channels due to light absorption inside the metal thus quenching the emission of luminophores.<sup>30</sup> If the probe molecules are very close to the nanoparticles (typically, less than 5 nm), luminescence emission is quenched due to Förster transfer of energy from the excited state of the molecule to the surface plasmons of the metal surface. This quenching effect decreases with the cube of separation distance.<sup>56</sup> If the probes are too far from the nanoparticles, the influence of the nanoparticles is diminished. Hence, there exists an optimum separation distance for maximum emission enhancement/quenching.<sup>13,21,23,152,153</sup>

Metal-enhanced luminescence (MEL) has been studied mostly using silver nanoparticles<sup>3,11,16,19,33,39,151,154</sup> due to their intense and narrow SPR peaks. Gold nanoparticles are known to both quench and enhance luminescence depending on the fluorophore-particle separation distance, molecular dipole orientation with respect to particle surface, and size of the nanoparticles.<sup>22,29,43</sup> Relatively smaller (typically less than 30 nm) gold nanoparticles quench fluorescence emission due to non-radiative transfer from the excited states of luminophore molecules to the gold nanoparticles.<sup>43</sup> Larger gold nanoparticles can enhance luminescence due to the increased contribution of nanoparticle scattering.<sup>22,155</sup> Other metals such as copper and aluminum have been reported to enhance luminescence.<sup>17,44</sup> Recently, zinc oxide (ZnO) nanorod platforms have been reported to enhance luminescence intensity significantly from commonly utilized fluorophores in immunoassays.<sup>47-49</sup> Both enhancement and quenching of luminescence due to the proximity of nanoparticles are efficiently utilized for many different applications. Enhanced signal and photostability of luminophores, improved surface immunoassay and DNA detection, enhanced wavelength-ratiometric sensing, and amplified assay detection are few examples of the applications of MEL. On the other hand, quenching resulting from metallic nanoparticles has been successfully utilized for the improvement of homogeneous and competitive fluorescence immunoassay,<sup>156,157</sup> optical detection of DNA hybridization,<sup>158</sup> competitive hybridization assay,<sup>159</sup> and in optoelectronics.<sup>160</sup>

There are some theoretical models explaining the influence of metal nanostructures on luminescence of dyes in the literature. Models based on exact electrodynamic theory<sup>92,93</sup> and the Gersten-Nitzan (GN) model<sup>93,95,96</sup> provide insight

into the influence of metal nanospheres on radiative and non-radiative decay rates of luminophore molecules at close proximity. These theories explain that electromagnetic interaction between luminophore and metal nanostructures results in the increase of both radiative and non-radiative decay rates depending on luminophore-nanoparticles separation distance and the properties of nanoparticles (size, shape, and dielectric constant) which decide the scattering and surface plasmon resonance behavior of the nanospheres. Based on these theories, it can be concluded that both radiative and non-radiative decay rates can be manipulated to result in luminescence enhancement or quenching by designing nanostructured platforms of particular shape, size, and composition. Mertens *et al.*<sup>93,96</sup> have corrected the GN model to account for radiation damping and dynamic depolarization and have shown that results obtained using this corrected GN model compare well with a model based on exact electrodynamics. This corrected GN model is suitable for a larger particle-size range than the original version. Kümmerlen *et al.*<sup>33</sup> presented a model that is based on the GN model and includes both excitation enhancement by local field effects and the change in emission intensity due to radiative and non-radiative decay rate enhancement. In our study, we used a theoretical model based on theory proposed by Kümmerlen *et al.*<sup>33</sup> and Mertens *et al.*<sup>93</sup> to study the effect of composition of alloy nanoparticles on quantum efficiency enhancement.

SPR wavelength and scattering efficiency, the most important properties of nanostructures which dictate the enhancement/quenching of luminophore molecules<sup>24,154</sup>, can be manipulated by controlling any of the parameters of particle size, aspect ratio, shape, particle-to-particle distance and surrounding dielectric medium.<sup>54,154,161</sup> Alloy nanoparticles offer additional degrees of freedom for tuning their optical properties by

altering atomic composition and atomic arrangement<sup>162</sup>, thus can be an attractive option for manipulating the luminophore signal. Herein, we report the use of alloy nanoparticles for MEL. We demonstrate that by tuning the composition of alloy nanoparticles, the signal of vicinal luminophore can be manipulated. Due to their interesting optical properties, we chose silver-copper alloy nanoparticles as a material for our study.<sup>101,102,116,163</sup> Figure 4-1 shows imaginary components of dielectric constants ( $\epsilon_2$ ) for 10 nm Ag and Cu nanoparticles in the wavelength range of 200 nm to 800 nm. The imaginary components of dielectric constants of bulk metal are modified using the model suggested by Garcia *et al*<sup>68</sup> (Equation 2-26). From this Figure 4-1, we can see the imaginary component of the dielectric constant of copper is significantly larger (more than twice) than that of silver in the wavelength range of 300 nm to 600 nm. Hence, it is expected that in this wavelength range, due to higher ohmic losses, Cu nanoparticles will mostly quench the luminescence at close proximity.<sup>17</sup> Further, the SPR spectrum of Ag is more intense and narrower than that of Cu nanoparticles. The absorption peak attributed to SPR occurs at shorter wavelengths for Ag. Hence, by modifying the composition and atomic arrangement we can tune both breadth and location of the peak of the SPR spectrum of Ag-Cu alloy nanoparticles.<sup>163</sup> We observed the effects of Ag-Cu alloy nanoparticles on the fluorescence emission from Cy3, a commonly used luminophore in biological applications. We chose Cy3 due to its low quantum yield (<.04). Cy3 is a reactive water-soluble fluorescent dye of the cyanine dye family with excitation peak at 550 nm and emission peak at 570 nm (see Figure 4-2 for molecular structure).<sup>164</sup> We found that the composition of alloy nanoparticles has a strong effect on

MEL. We establish simple and straightforward routes for manipulating the brightness of emission from luminophore by changing the composition of the alloy nanoparticles.

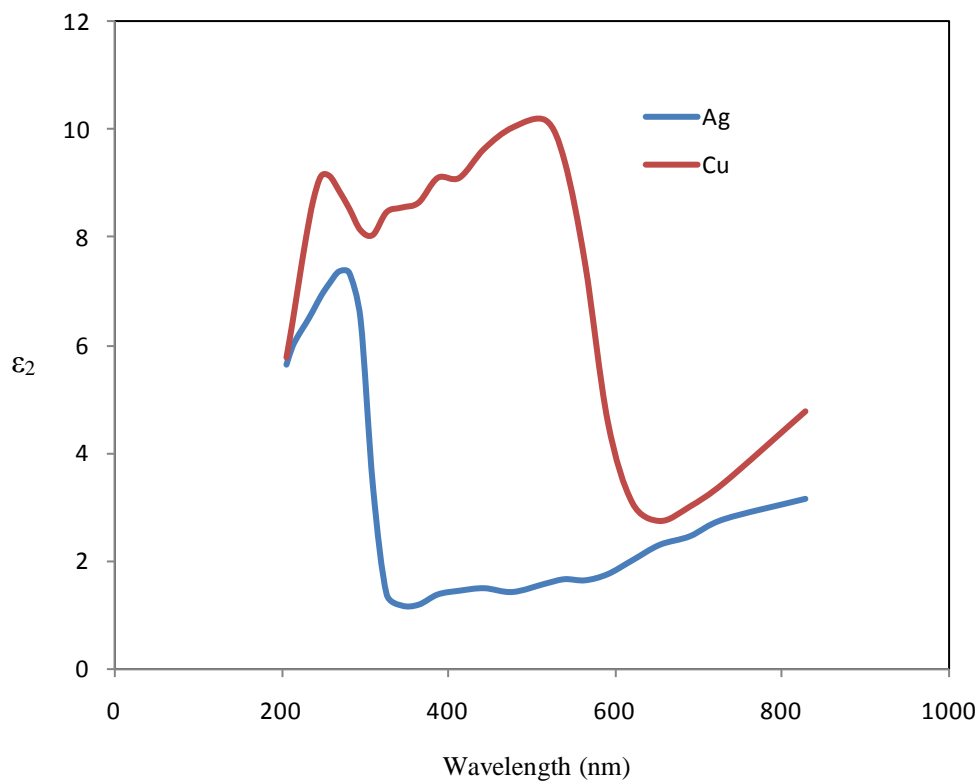


Figure 4-1  $\epsilon_2$  of 10 nm Ag and Cu nanoparticles.

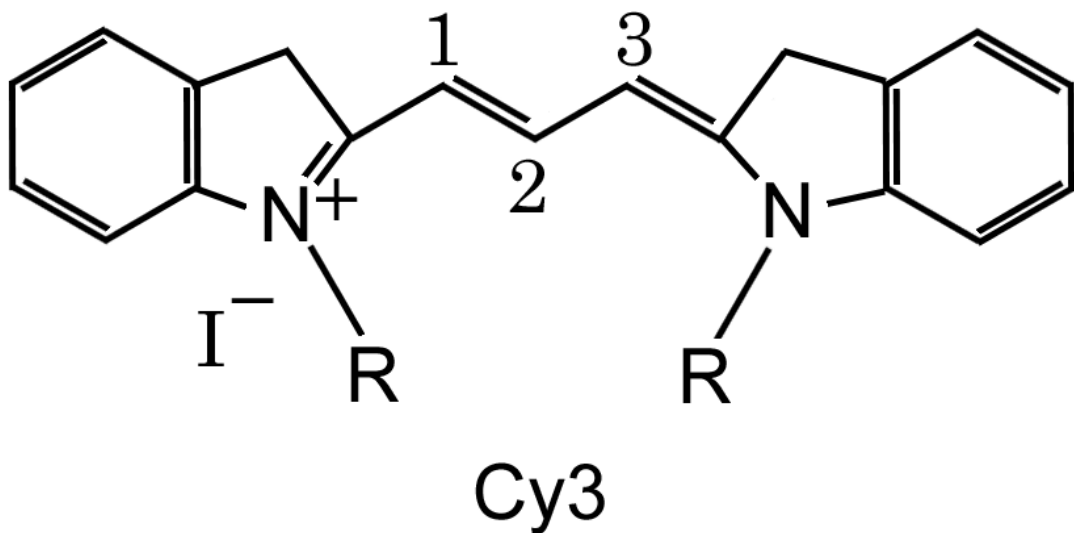


Figure 4-2 Molecular structure of Cy3. <sup>164</sup>

## 4.2. Experimental

In this study, Ag-Cu nanoparticles of five different compositions were synthesized using the polyol process as described in reference.<sup>110</sup> Silver nitrate (>99%), copper (II) acetate hydrate (98%) and polyvinylpyrrolidone (PVP, 55000 molecular weight) were obtained from Sigma-Aldrich Co. MO, and used as received. Same volume of solution of PVP (1.0634 g in 20 ml ethylene glycol) was first added to ethylene glycol solution of copper salt (0.016 moles) and was then de-aerated by bubbling with nitrogen for 30 minutes. The solution was then held at 175<sup>0</sup> C for 20 minutes under nitrogen atmosphere, and a certain amount of AO<sub>3</sub>- ethylene glycol solution was added to it. The reaction was then allowed to continue for another 5 minutes before bringing the system down to room temperature. Alloy nanoparticles of different compositions were synthesized by varying the molar ratio of silver and copper salts in the reaction mixture. With an increase in copper percentage, the color of the colloidal solution changed from yellowish to more reddish. Copper nanoparticles were synthesized following the same procedure except that the silver nitrate solution was replaced by the reducing agent ascorbic acid.

Glass substrates were silanized to immobilize silver-copper nanoparticles on these<sup>40</sup>. Glass slides were first cleaned with piranha solution for 30 minutes (1:3 30% hydrogen peroxide/concentrated sulfuric acid); (CAUTION! *Piranha solution reacts violently with most organic materials and should be handled with extreme care*). The cleaned glass substrates were silanized by immersing them in 2% 3-(aminopropyl)triethoxysilane (APS) solution in methanol for 2 hours.<sup>40</sup> After this, the slides were thoroughly cleaned with methanol followed by water to remove any excess

APS. Ag-Cu nanoparticles were deposited on the APS coated glass slides by soaking them in freshly prepared solutions for specific times. Copper nanoparticles were immobilized on the glass slides following the procedure given by Male *et al.* <sup>165</sup> Piranha- cleaned glass slides were immersed in 20% poly (diallyldimethylammonium chloride), (PDDA, MW 200 000-350 000, Aldrich) aqueous solution for 16 hours. Then, these slides were thoroughly rinsed with deionized water and dried in a nitrogen stream. These polymer coated glass slides were incubated in Cu nanoparticle solution for 3 hours. Finally, Cu nanoparticles coated glass slides were rinsed with deionized water and dried with nitrogen.

Silver nanoparticles were synthesized using the well-known Tollens reaction. <sup>21</sup> In summary, 10% ammonium hydroxide was added to 10 ml of aqueous  $\text{AgNO}_3$  (0.1 M) while stirring. Once the initially formed brown precipitate dissolved, a 0.8 mole solution of NaOH in water was added to the solution. Preparation of Tollens reagent was completed by adding  $\text{NH}_4\text{OH}$  drop-wise to the solution until the brown precipitate dissolved. The Tollens reagent was stored in a refrigerator for 30 minutes to reduce its temperature to  $\approx 4^\circ \text{C}$ . For deposition of silver nanoparticles on glass substrates, equal amounts of the Tollens reagent and 0.5 M dextrose solution were mixed together and immediately drop cast on a piranha-cleaned glass substrate followed by rinsing with de-ionized water after 1 minute. The surface morphology of the nanostructures was observed and characterized by transmission electron microscopy (FEI Morgai 268D), atomic force microscopy (Digital Instruments, Nanoscope IIIa), and scanning electron microscopy (Hitachi S-800). A UV-vis spectrometer (JASCO, V-530) was used for measuring the light extinction spectra attributed to the SPR of these nanoparticles. TEM samples were prepared by

dispersing a few drops of Ag-Cu alloy nanoparticle solution on a carbon film supported by molybdenum grids.

Luminophore coatings on the nanoparticles and glass substrates were accomplished by dispersing Cy3-labeled streptavidin in 0.25% poly (vinyl alcohol) (PVA, MW 15000) aqueous solution by sonicating and then coating the solution on the substrates by spin coating (1500 rpm speed). The resulting polymer thickness was approximately 26 nm. Hence, the average distance between the substrate and a luminophore molecule was approximated by 13 nm. As the luminophores were coated following the same procedure for all samples, the separation distance between luminophore molecules and nanoparticles and the coverage of the luminophore molecules on nanoparticles are assumed to be the same for all samples.

A Leica DMI 4000b inverted fluorescence microscope equipped with a Leica DFC340 FX CCD camera was utilized for all luminescence measurements. This allowed inspection of a large area in a single view frame. Fluorescence microscopy was carried out with customized filter sets (Chroma Technology) for Cy3. To avoid photobleaching, the specimen was exposed to illumination only while taking images. Image Pro-plus version 6 with Scope Pro version 6 (Media Cybernetics, Inc) was used for acquiring and analyzing images. We obtained fluorescence intensities for each sample by analyzing a 1.64 mm × 2.19 mm image-section of each substrate. Background images were obtained from an uncoated substrate and unmodified glass cover slips at the same conditions. Images from the experimental samples were corrected for uneven illumination with the help of these background images. Images of nanoparticle coated glass coverslip were captured and compared with the image of a bare glass coverslip to test for the possibility

of scattered light from metal particles. These images showed that the emission filters effectively removed the scattered light, so its contribution is negligible. The luminescence intensity of each sample was determined by measuring the mean intensity and subtracting the mean value of the background image.

#### 4.3. Results and Discussion

The UV-Vis absorbance spectra attributed to surface plasmon resonance of colloidal Ag-Cu nanoparticles show a single peak in the visible range. With increasing copper percentage, this SPR peak shifts to longer wavelengths (Figure 4-3). This result confirms that the nanoparticles are a bimetallic form of silver and copper and not a mixture of silver nanoparticles and copper nanoparticles.<sup>166</sup> The red-shifts of the SPR peaks with increasing copper concentration are attributed to the decrease in conductivity<sup>101</sup>. There is no visible difference between the position of absorbance peaks of Ag-Cu nanoparticles in solution and on APS coated slides.

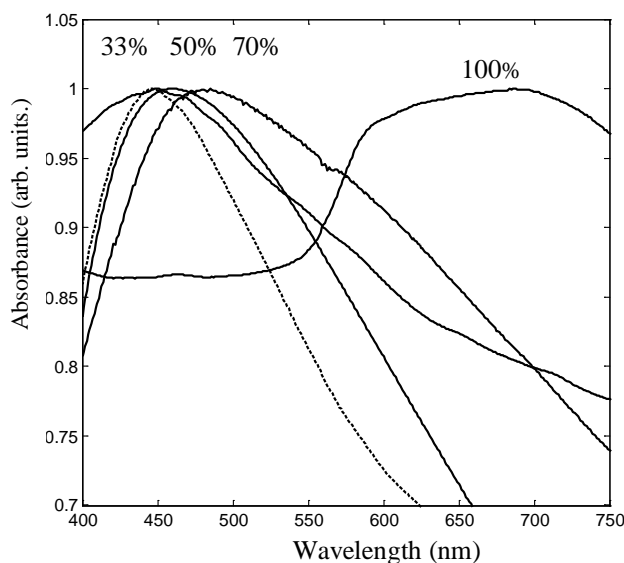


**Figure 4-3 Normalized Absorption spectra for Ag-Cu alloy nanoparticles. Dotted line is for Ag-Cu nanoparticles with 33% Cu on APS coated glass slides.**

Transmission electron microscopy (Figure 4-4) of the colloidal Ag-Cu alloy nanoparticles indicated the particle size to be in the range of 130 nm to 200 nm (derived from a population of 100 particles). STEM EDS data (Figure 4-4(C) and 4-4 (D)), confirms that the nanoparticles comprise both Ag and Cu. The energy dispersive X-ray analysis on the single particle showed that the composition for each particle was roughly consistent with that of feeding solution (Figure 4-4(C) and (D)). Estimation of exact composition of Ag-Cu nanoparticles, which can be measured by using method like inductively coupled plasma mass spectroscopy (ICP-MS) analysis<sup>167</sup>, is beyond the scope of this study. However, lack of information about exact composition should not affect the conclusions of this study.

The concentration of nanoparticles increased with increase in immersion time of APS coated glass slides in Ag-Cu colloidal solutions. As the copper percentage increased, the time required to attach the Ag-Cu colloids on glass slides also increased. For comparison, APS coated glass slides were allowed to soak in different composition Ag-Cu colloidal solutions until the concentrations of nanoparticles on glass slides were approximately the same. The sizes of different composition Ag-Cu nanoparticles coated on glass slides were also found to be approximately the same. The size of nanoparticles and particle density were measured using Image j software. From the SEM images of the Ag-Cu nanoparticles (Figures 4-5(B) and 4-5(C)) the average size of these nanoparticles on the glass slides was measured to be approximately 150 nm (derived from a population of 800 nanoparticles). SEM images of the Ag nanoparticles (Figure 4-5(A)) indicate their average size to be approximately 80 nm. AFM images of the Ag and Ag-Cu nanoparticles on glass slides are given in Figures 4-6(A),4- 6(B) and 4-6(C). The particle

density for Ag nanoparticles was estimated to be 38 particles/square microns. Particle density for Ag-Cu nanoparticles was estimated to be 20 particles/square microns. It is difficult to obtain the same size and particle density for silver and silver-copper nanoparticles due to limitations of the synthesis techniques.

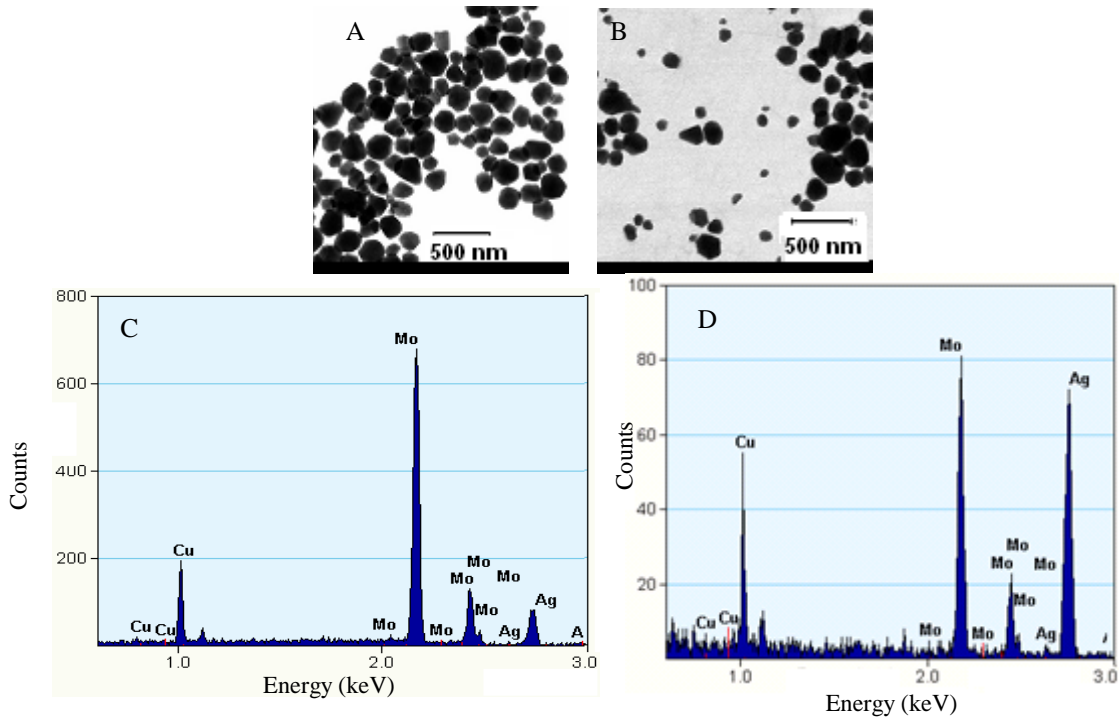


**Figure 4-4** TEM images of Ag-Cu np synthesized from different composition feeding solution (A) Ag/Cu (1/1) and (B) Ag/Cu(3/7). STEM EDS spectra for (C) Ag/Cu (1/1) and (D) Ag/Cu (2/1).

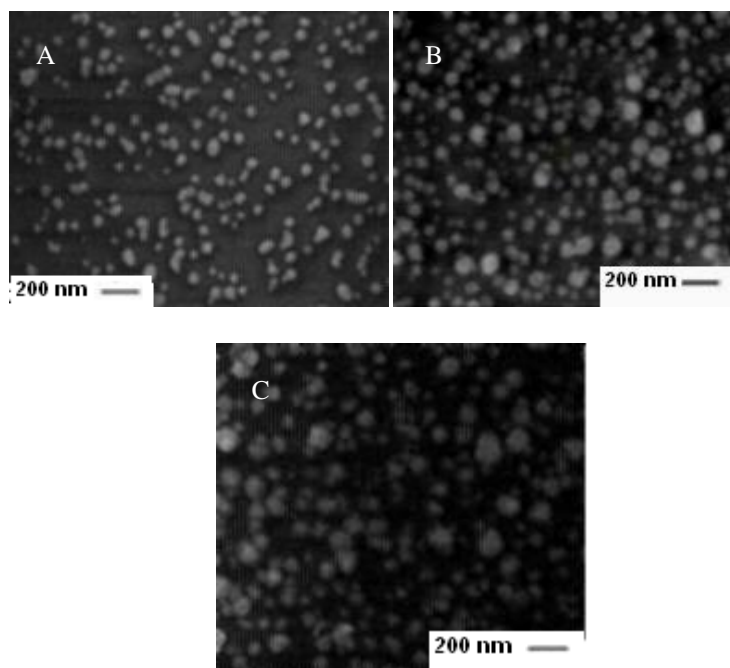


**Figure 4-5 SEM images of (A) Ag nanoparticles (B) 2:1 Ag-Cu (C) 1:1 Ag-Cu nanoparticles coated on glass substrate.**

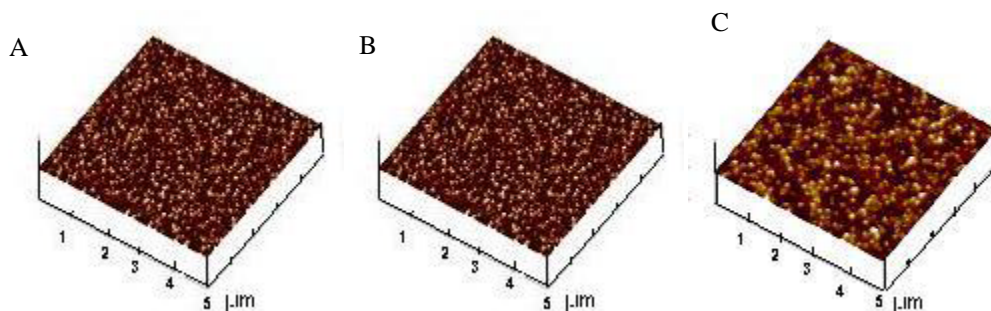


**Figure 4-6 AFM images of (A) Ag nanoparticles (B) 2:1 Ag-Cu nanoparticles (C) 1:1 Ag-Cu nanoparticles coated on glass substrates.**

Luminescence intensity of Cy3 was observed to increase significantly in the vicinity of both Ag and Ag-Cu nanoparticles (Figure 4-7). The enhancement ratio for Ag and Ag-Cu nanoparticles was calculated by comparing luminescence intensity of the sample with the luminescence intensity of the luminophore coated on an APS coated glass substrate. Please note average fluorescence intensity of dye coated on glass is not zero here. In the case of copper nanoparticles, the enhancement ratio was calculated

comparing the luminescence intensity with luminophore coated on PDDA coated glass slides. The Ag nanoparticles platform resulted in very strong enhancement ( $90 \pm 19$  times) for Cy3. As the quantum efficiency of dye Cy3 is very small, the enhancement effect is high. The Ag-Cu nanoparticles also showed enhancement ( $55 \pm 15$  times for 2:1 Ag-Cu,  $30 \pm 6$  times for 1:1 Ag-Cu) but as the copper percentage in nanoparticles increased, the enhancement decreased. Finally, instead of enhancing, the Cu nanoparticles quenched ( $7 \pm 5$  times) the luminescence of Cy3. This may be due to the fact that in the vicinity of metal nanoparticles, both the radiative decay rate and the non-radiative decay rates increase, and as the percentage of Cu increases, the nonradiative decay rate also increases, eventually surpassing the radiative decay rate.

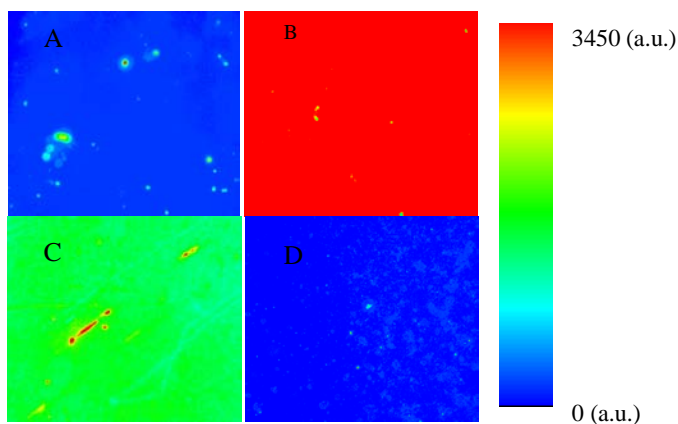


**Figure 4-7** Pseudo colored image of Cy3 coated on (A) glass (B) Ag nanoparticles (C) 1:1 Ag-Cu nanoparticles and (D) Cu nanoparticles.

We calculated the modified overall quantum efficiency at the proximity of different compositions of Ag-Cu nanoparticles based on the model suggested by Kümmerlen *et al.*<sup>33</sup> which includes both excitation and emission enhancement factors as discussed in Section III. The absorption enhancement factor was calculated based on the

enhancement of local electric field at the excitation frequency ( $\omega_{abs}$ ). The corrected GN model<sup>93,96</sup> model was used to calculate the quantum efficiency change due to radiative and the non-radiative decay rate enhancements. For better representation of experimental conditions, the source dipole orientation was averaged over all solid angles. This was achieved by averaging the results for decay rates obtained for radial and tangential orientations. Dielectric constants for Ag-Cu nanoparticles of different compositions were calculated following the procedure described by Bruzzone.<sup>105</sup> The dielectric function was calculated using the semi-empirical model based on Drude theory and experimental data. The experimental data used for this calculation were obtained by averaging the values for pure metals over the volume.<sup>168</sup> Drude contributions for nanostructure and bulk were calculated using the values of pure metal averaged over volumes. Though Ag-Cu cannot form a solid solution at room temperature as does Ag-Au, the surface plasmon resonance spectrum resembles that of alloy nanoparticles.<sup>113</sup> This is due to the fact that both silver and copper exist in the surface of Ag-Cu nanoparticles, and surface plasmon resonance is a surface phenomenon.<sup>113</sup>

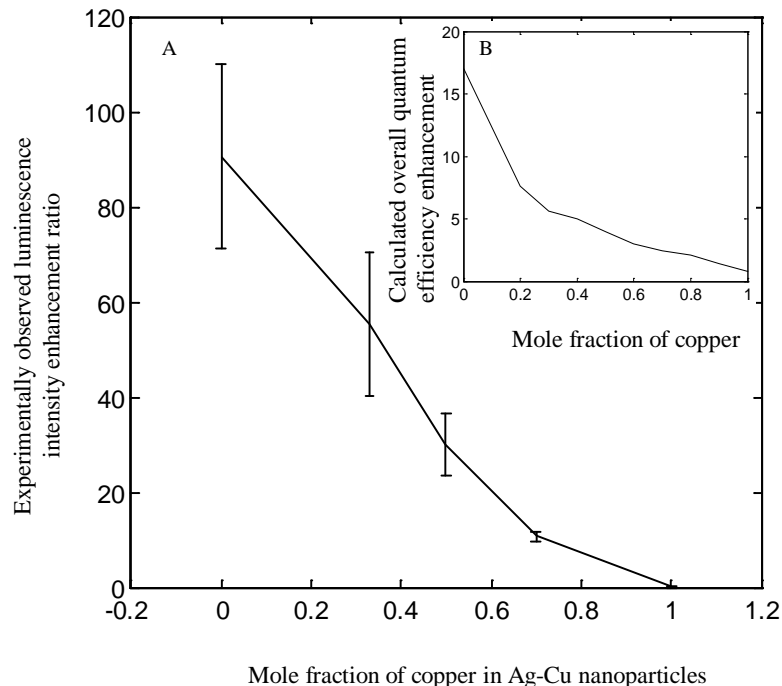


**Figure 4-8 (A) Experimentally observed luminescence enhancement ratio of Cy3. (B) Inset shows theoretically calculated overall luminescence quantum efficiency enhancement ratio.**

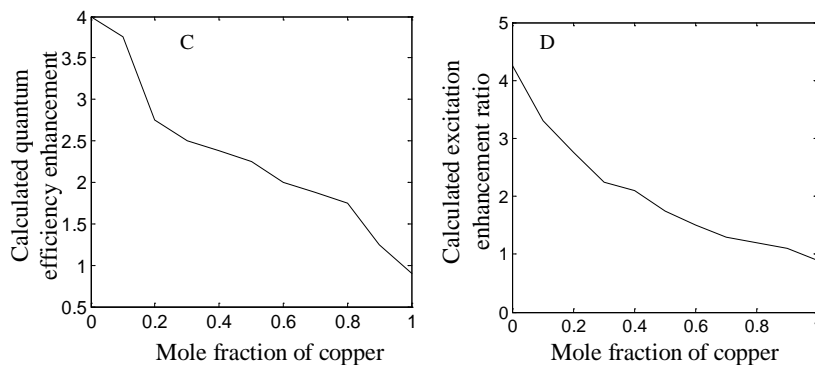


**Figure 4-9 (A) Calculated quantum efficiency enhancement factor due to emission enhancement. (B) and excitation enhancement factor.**

Calculations were done to corroborate experimental results and to establish the optimum size of nanoparticles. Figure 4-8 A and 4-8B show the theoretically calculated modified overall quantum efficiency and the experimentally observed luminescence

enhancement ratio of luminophore Cy3 in the vicinity of different compositions of Ag-Cu nanoparticles. The calculations were done assuming the size of nanoparticles to be 150 nm and the separation distance between nanoparticles and luminophore molecules to be 13 nm to compare with experimental results. The surrounding dielectric medium was assumed to be poly (vinyl alcohol). The enhancement of local electric field amplitude ( $|L_{abs}^2|$ ) was calculated at the absorption frequency of Cy3 (550 nm). The quantum efficiency change ( $Z(\omega_{flu})$ ) due to radiative and nonradiative decay rate enhancement was calculated at 570 nm emission wavelength, which is the emission peak for Cy3. The quantum efficiency was calculated taking into account all multipole modes up to  $l=100$ . Dipole orientation was assumed to be averaged over all solid angles. It can be seen from Figures 4-8A and 4-8B that both theoretical and experimental results show the same trend that with increase in copper percentage in nanoparticles, the enhancement effect decreases, with pure copper quenching luminescence. The theoretically calculated emission enhancement factor and excitation enhancement factor are separately shown in Figures 4-9A and 4-9B, respectively. We can see that both emission and excitation have comparable effects on overall quantum efficiency change. Some reasons for the discrepancy in numerical values between theoretical and experimental results are the differences in experimental geometry (nanoparticles are not in a homogeneous dielectric environment, all the nanoparticles were not of spherical shape and not of same size, luminophore nanostructures separation distance is not precise) with respect to theoretical calculations, which assumed uniformity in these parameters. It can be also because we observed the luminescence intensity of the image over the entire bandwidth of filters used for fluorescence microscopy not at any particular wavelength.

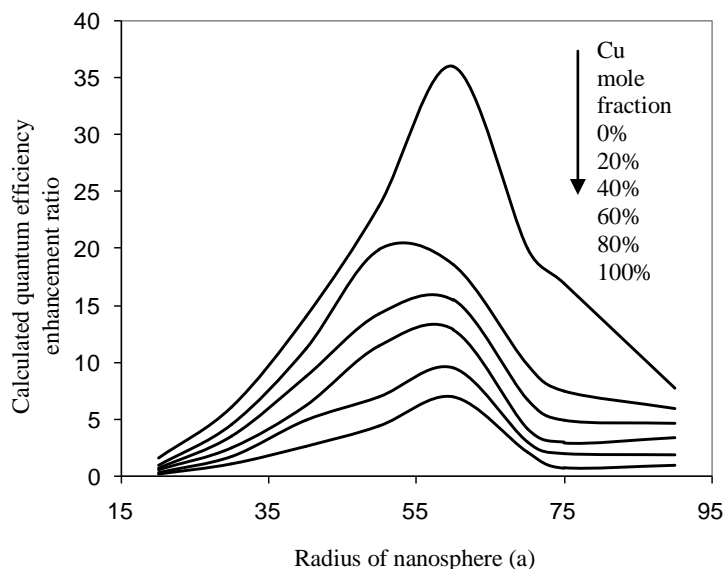


**Figure 4-10 Quantum efficiency enhancement ratio of Cy3 in the proximity of different diameter Ag-Cu nanoparticles at different compositions.**

It is known that quantum efficiency enhancement depends on the size of spherical nanoparticles<sup>93</sup>. Figure 4-10 shows the dependencies of quantum efficiency enhancement on the size of Ag-Cu nanoparticles at the fluorophore-nanoparticles separation distance of 13 nm. The calculation for Figure 4-10 was done considering the same emitter-particle orientation and surrounding conditions as for Figure 4-8. It can be seen from Figure 4-10 that there is an optimum size of nanoparticles for which quantum efficiency enhancement is maximum. The coupling between the emission of the luminophore and the plasmon mode increases as the size of the nanoparticles decreases, and coupling efficiency of emission at far field through nanoparticle scattering increases as the size of nanoparticles increases. Both of these coupling phenomena are responsible for enhancement of quantum efficiency. Spectral overlap between the absorption and emission spectra of luminophore and surface plasmon resonance spectra of metal nanoparticles is very important for optimum luminescence enhancement<sup>24,154</sup>. Some

theoretical and experimental studies have suggested that luminescence enhancement is largest when the emission wavelength is slightly red-shifted from that of the plasmon resonance<sup>24,26,169</sup>. When the size of the particle increases, the plasmon resonance is shifted to longer wavelength and broadened and decreases in magnitude due to dynamic polarization<sup>170</sup>. So, there exists an optimum diameter. We can see from Figure 6 that the optimum radius for Ag, Ag-Cu and also for Cu nanoparticles is approximately 60 nm. At this optimum diameter, even Cu nanoparticles show enhancement instead of quenching. So it can be inferred that if we can synthesize alloy nanoparticles of optimum diameter using advanced methods like electron beam lithography, we can elucidate the effect of composition on metal-enhanced luminescence better.

#### 4.4. Conclusions

In summary, in this work, metal-enhanced luminescence/ quenching of luminophore Cy3 is explored in the vicinity of Ag-Cu alloy nanoparticles at different compositions. The effect of composition of Ag-Cu alloy nanoparticles on luminescence enhancement is studied. We have shown that strongest enhancement is observed on the Ag nanoparticles platform, and as the percentage of copper increases in the nanoparticles, the enhancement decreases. At pure copper nanoparticles platforms, the luminescence is quenched. A simple technique to tune the brightness of a luminophore by changing the composition of alloy nanoparticles is presented. Experimentally obtained data for luminescence change qualitatively match with theoretical calculations. We believe such manipulation in luminescence brightness of a dye will open up different applications of luminescence emission. We expect quenching effect of copper nanoparticles will

motivate the utilization of these nanoparticles as an inexpensive alternative to gold in biological applications such as homogeneous and competitive fluorescence immunoassay, detection of DNA hybridization, competitive hybridization assay, and also in optoelectronics.

## Chapter 5 - Silver-Copper Alloy Nanoparticles for Metal Enhanced Luminescence

### 5.1. Introduction

Luminescence based measurements and devices are currently widely used methods in different fields such as biology, chemistry, materials science and medicine. Single molecule detection<sup>171</sup>, DNA sequencing<sup>172</sup>, quantum cryptography<sup>173</sup>, and LEDs<sup>174</sup> are some examples of its numerous, diverse applications. Strong luminescence intensity is one of the most important desired properties of luminophores for their applications in luminescence sensors. It is possible to design and synthesize luminophores with desired spectral properties. However, it is difficult to design luminophores with desired luminescence intensities. Nearby conducting metallic particles, colloids, and surfaces are known to significantly influence the emission of vicinal luminophores<sup>3,9,11-13,16,17,20-24,27-29,32,33,36-39,44,151,154,155,175-177</sup>. Planar metal films are generally known to quench the emission from nearby fluorophores. Luminescence enhancements ranging from tens- to hundreds-fold in signal intensity have been reported in the literature<sup>3,22,24,27,41,47,174,178</sup>. Though the phenomena of metal enhanced luminescence (MEL) is known from the 1980s, the demonstrations and applications of MEL are mostly new. Different applications of metal enhanced luminescence and from different metallic nanoparticles have been reported in recent literature<sup>2-17</sup>. MEL has been studied mostly using silver and gold nanoparticles<sup>19-24,27-29,33,34,40,41,51,179</sup> due to their intense and narrow SPR peaks.

Recently, other metals such as copper and aluminum have been reported to enhance luminescence<sup>17,44</sup>. But, due to the higher ohmic losses, the MEL effect is not as pronounced in Cu and Al as it is in Ag or Au. Recently zinc oxide (ZnO) nanorod platforms have been reported to enhance luminescence intensity significantly, from commonly utilized fluorophores in immunoassays<sup>47-49</sup>.

Luminescence enhancement phenomenon is dependent on several parameters such as material properties, size and shape of nanostructures, and luminophore-nanostructure separation distance. Metal nanoparticles can influence vicinal luminophore molecules in several ways such as by enhancing the incident optical field, increasing the radiative decay rate and quenching the emission by increasing nonradiative decay rate<sup>11,28,39,151</sup>. If the probe molecules are very close to the nanoparticles (typically less than 5 nm), luminescence emission is quenched due to Forster transfer of energy from the excited state of the molecule to the surface plasmons of the metal surface. This quenching effect decreases with the cube of separation distance<sup>56</sup>. If the probes are too far from the nanoparticle–platform, the influence of the platform is diminished. Hence, there exists an optimum separation distance for maximum emission enhancement<sup>13,21,23,152,153</sup>.

Using nanoparticle platforms, it is possible to increase the quantum yield of weakly luminescent probes by modifying their radiative decay rate to increase their emission efficiency, or by coupling the emission with far field scattering. The emission intensity of luminophores with nearly unit quantum yield can also be improved by enhancing their absorption by increasing the local electric field. Light intensity of nanoparticles at near field is strongly dependent on the surface plasmon resonance (SPR)

wavelength of the metal nanostructures. SPR wavelength, one of the most important properties of nanostructures, dictates the choice of materials to be used for luminescence enhancement. Tam *et al.*<sup>154</sup> found that the enhancement is optimal when the plasmon resonance wavelength of the nanoparticles is tuned to the emission wavelength of the low quantum yield luminophores. Recent theoretical and experimental studies have suggested that luminescence enhancement is largest when the emission wavelength is slightly red-shifted from that of the plasmon resonance<sup>24,26</sup>. Chen *et al.*<sup>24</sup> suggested that the optimal location of the SPR peak of nanoparticles is between the excitation and emission peaks of luminophores for maximum enhancement, as both excitation and emission rates can be enhanced in such a situation. One can expect that the ability to tune the position of the SPR peak of the nanoparticles over a wide range of wavelengths will allow for extension of the MEL phenomenon to a wide range of luminophores. So far, MEL has been studied mostly on pure metal platforms. SPR wavelengths of pure metal nanoparticles can be tuned to different values by controlling several parameters such as particle size, shape, particle-to-particle distance and surrounding dielectric medium<sup>24,53,54,180,181</sup>. However, it is easier to tune SPR spectra of alloy nanoparticles over a wide range of wavelengths as these offer additional degrees of freedom for tuning their optical properties by altering atomic composition and atomic arrangement<sup>162</sup>. This could potentially enable development of specifically tailored nanoparticle platforms for MEL of a wide range of luminophores. This is the motivation for us to study alloy nanostructured platforms for MEL.

Herein, we report the use of alloy nanoparticles for MEL. We demonstrate that SPR spectra of alloy nanoparticles can be tuned by manipulating an easily controlled

experimental variable to result in maximum spectral overlap of the emission and absorption spectra of the luminophores with the SPR spectrum of the nanoparticles. Also, we show that Ag-Cu nanomaterials can serve as excellent candidates for MEL, due to their interesting optical properties<sup>101,102,116,163</sup>. These alloy nanoparticles are less lossy than pure Cu ones<sup>116</sup>, hence, expected to result in better MEL. The SPR spectrum of Ag is more intense and narrower than that of Cu nanoparticles. The absorption peak attributed to SPR occurs at shorter wavelengths for Ag. Hence, by modifying the composition and atomic arrangement we can tune both breadth and location of the peak of the SPR spectrum of Ag-Cu alloy nanoparticles<sup>163</sup>. SPR peak wavelengths of Ag-Cu alloy nanoparticles can easily be tuned in the visible and near infrared region by changing only the annealing temperature<sup>101</sup>. We observed enhanced fluorescence emission from two thiol-reactive dyes, Alexa Fluor 594 and Alexa Fluor 488 (obtained from Molecular Probes, Invitrogen, Portland, OR), at the proximity of these Ag-Cu alloy nanoparticles. We establish simple and straightforward routes for the successful growth and fabrication of nanostructured platforms which can be effectively utilized to enhance the luminescence of any luminophore. In addition, our work also provides insights into the effect of SPR on MEL.

## 5.2. Experimental Method

In this study, Ag or Ag-Cu nanoparticles were deposited on 22×22 mm glass cover slips (Fisher finest cover glass, thickness approximately 140 microns) by using DC magnetron sputtering (Plasma Sciences CRC-100 Sputter Tool). Before the depositions, the cover slips were cleaned by air plasma (Harrick PDC-32G) for 10 minutes at 6.8

watts power setting. During deposition, the background pressure was of the order of  $10^{-6}$  Torr, the Ar pressure was 5 mTorr and the current and voltage were 50 mA and 0.4 kV respectively. An Ag target was utilized to deposit the Ag nanoparticles and a Cu foil attached on the Ag target was utilized for the Ag-Cu nanoparticle deposition (Figure 5-1). Varying the ratio of the surface area of Ag to Cu exposed for sputtering allowed for changing the composition of the Ag-Cu alloy nanoparticles. Surface morphology of the nanostructures was observed and characterized by transmission electron microscopy (FEI Tecnai F20 S-Twin TEM). An electrical furnace (Lindberg, Blue M) was used for annealing of the Ag-Cu nanoparticles. Annealing temperature ranged from 298 K to 523 K and the annealing time was 5 minutes. Annealing was done in vacuum (30 inch Hg vacuum) to minimize oxidation of the nanoparticles. An UV-vis spectrometer (JASCO, V-530) was used for measuring the light absorption spectra attributed to the SPR of these nanoparticles.

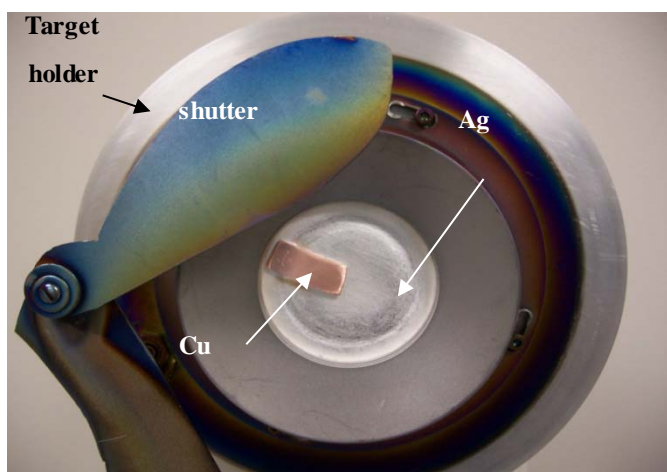


**Figure 5-1** Picture of DC magnetron sputterer with Ag-Cu target

Mouse Immunoglobulin G (IgG), labeled with luminophores Alexa Fluor 488 and Alexa Fluor 594 was coated on samples (Figure 5-2) following known methods<sup>177</sup>. Samples

were first non-covalently coated with mouse anti-rabbit IgG (Immunopure, Pierce Biotechnology) solution (25  $\mu$ g/ml) which was diluted with sodium phosphate buffer (pH 7.4). Blocking was performed using blocking solution (1% bovine serum albumin solution in sodium phosphate buffer). Protein labeling kits of both Alexa Fluor 488 and Alexa Fluor 594 were used to label goat anti-mouse IgG with dye. Dye labeled anti-mouse IgG was also diluted using sodium phosphate buffer. Diluted dye-labeled conjugate solution was coated on the sample (already coated with mouse anti-rabbit IgG). Details of the coating procedure are as follows. The samples were covered with tape containing punched holes (of size 36 mm<sup>2</sup>) to form wells on the surface of the slides. A coating solution of IgG (25  $\mu$ g/ml of IgG dissolved in Na-phosphate buffer) was added to each well (25  $\mu$ l /well), and samples were incubated for 4 h at room temperature in a humid container. Samples were then rinsed with water. Blocking was performed by adding 35  $\mu$ l blocking solution per well and incubating at room temperature for 4 h in a closed humid container again. 25  $\mu$ l dye-labeled conjugate dye anti-mouse IgG (diluted to 10  $\mu$ g/ml with Na-phosphate buffer, 50 mM, pH 7.4) was added to each hole of the sample slide (coated with mouse IgG) and samples were incubated at room temperature in a humid container for 2 h. Samples were then rinsed with water and were ready for the measurement.

As the luminophores were coated following the same procedure for all samples, the separation distances between luminophore molecules and the various nanoparticle platforms are assumed to be the same.

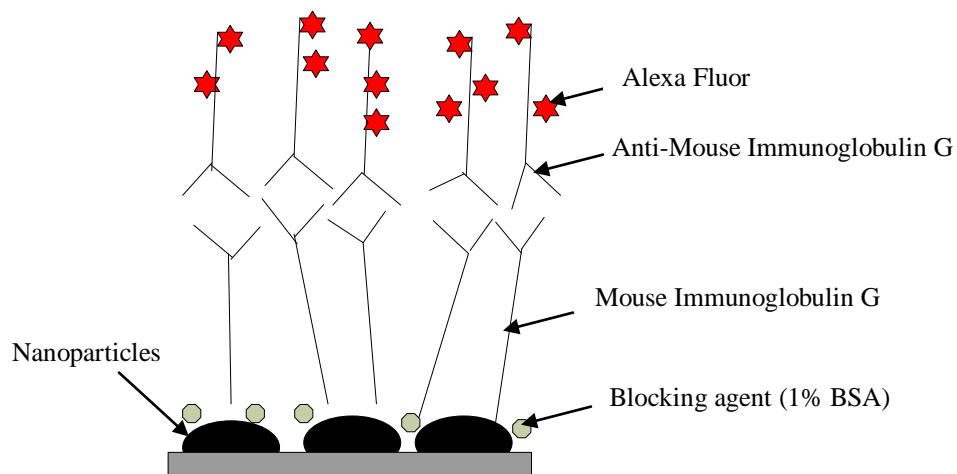


**Figure 5-2 Luminophores on Ag-Cu nanoparticles platform<sup>177</sup>**

The Leica DMI 4000b inverted fluorescence microscope equipped with Leica DFC340 FX CCD camera was utilized for MEL measurements. This allowed overall inspection of a large area in a single view frame. We took images of each specimen with customized filter sets for each luminophore. Fluorescence microscopy was carried out with a green filter set (Chroma Technology 31001, Exciter D480/30x, Dichroic 505 nm ,Emitter D535/40m) for Alexa Fluor 488 and red filter set (Chroma Technology 31004, Exciter D560/40x, Dichroic 595 nm ,Emitter D630/60m) for Alexa Fluor 594. To avoid photobleaching, the specimen was exposed to illumination only while taking images. Image Pro-plus version 6 with Scope Pro version 6 (Media Cybernetics, Inc) was used for acquiring and analyzing images. We obtained fluorescence intensities for each sample by analyzing a 1.64 mm × 2.19 mm image-section of each substrate. Background images were obtained from an uncoated substrate, and unmodified glass cover slips at the same conditions. Images from the experimental samples were corrected for uneven illumination with the help of these background images. Image of nanoparticles coated glass coverslip was captured and compared with image of bare glass coverslip to test for

the possibility of scattered light from metal particles. These images showed that the emission filters effectively removed the scattered light so its contribution is negligible. Luminescence intensity of each sample was determined by measuring the mean intensity and subtracting the mean value of the background image.

### 5.3. Results and Discussion

Transmission electron microscopy (FEI Tecnai F20 S-Twin TEM) of the Ag-Cu alloy nanoparticles indicated the average size to be  $14.77 \text{ nm} \pm 5.4 \text{ nm}$  (derived from a population of 100 particles) (Figure 5-4 (A)) and after annealing these nanoparticles at 448 K, the average size is  $13.88 \pm 4.07 \text{ nm}$  and the average size of Ag nanoparticles was  $13.78 \pm 3.12 \text{ nm}$ . From the HRTEM image (Figure 5-4 (B)), the lattice spacing was measured to be 0.21-0.24 nm. In the {111} lattice plane, silver has lattice spacing of 0.24 nm whereas the lattice spacing of Cu is 0.21 nm<sup>182</sup>. This, combined with STEM EDS data (Figure 5-5), confirms that the nanoparticles are comprised of both Ag and Cu. In these Ag-Cu nanoparticles, silver and copper remain phase separated<sup>113</sup>. From the TEM EDS data, approximate composition of the Ag-Cu nanoparticles was found to be 1:1.

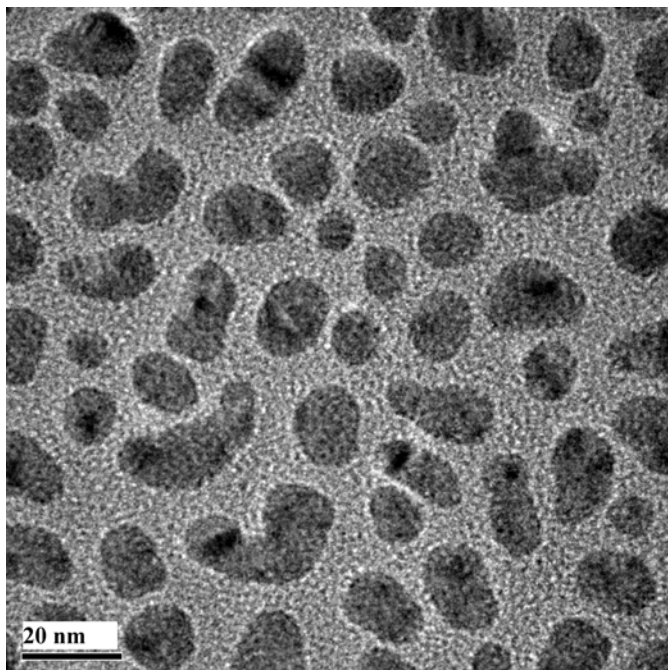


**Figure 5-3 High resolution TEM image of Ag nanoparticles**

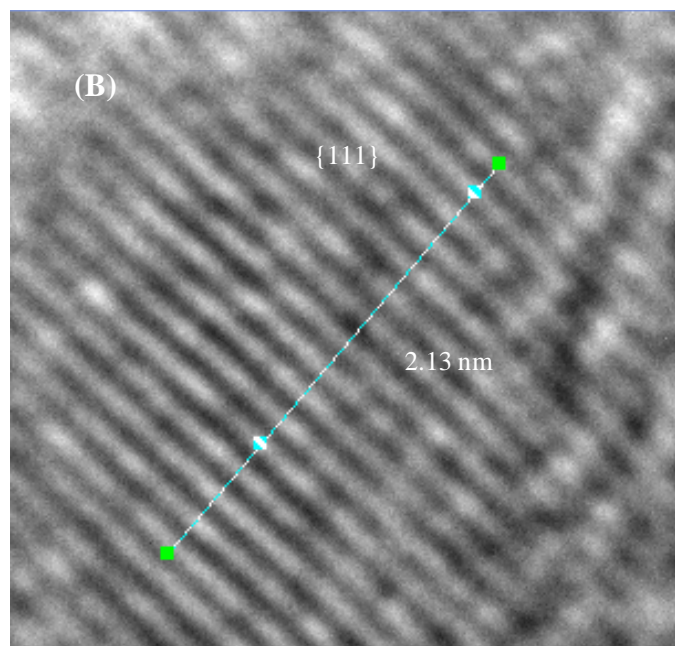
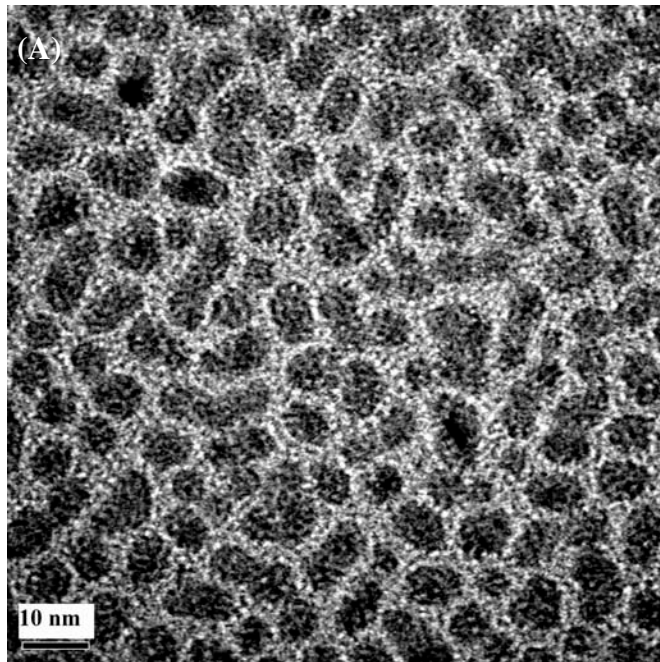


**Figure 5-4 (A)-(B) HRTEM image of Ag-Cu**

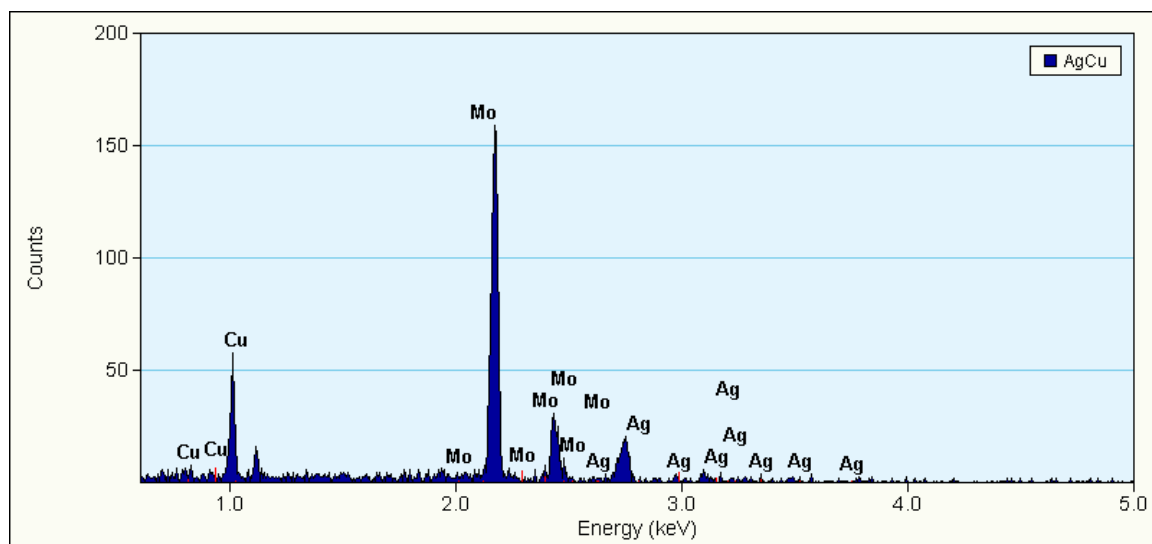


**Figure 5-5 STEM EDS spectra for Ag-Cu alloy nanoparticles**

The absorbance spectra (taken using UV-Vis spectrophotometer, JASCO, V-530), attributed to SPR of Ag-Cu nanoparticles, show a single peak in the visible range. With increasing copper percentage, this SPR peak shifts to higher wavelengths and becomes broader. This result confirms that the nanoparticles are a bimetallic form of silver and copper and not a mixture of silver nanoparticles and copper nanoparticles<sup>166</sup>. The red-shifts of the SPR peaks with increasing copper concentration are attributed to the decrease in conductivity<sup>101</sup>. The SPR peak of Ag-Cu alloy nanoparticles blue shifts upon increasing the annealing temperature from 298 K to 523 K. With increase in annealing temperature, Cu atoms surface-segregate, thereby increasing the concentration of Ag in the nanoparticle core as a result, and the SPR peak gradually moves nearer to the SPR peak of pure Ag nanoparticles (Figure 5-6).

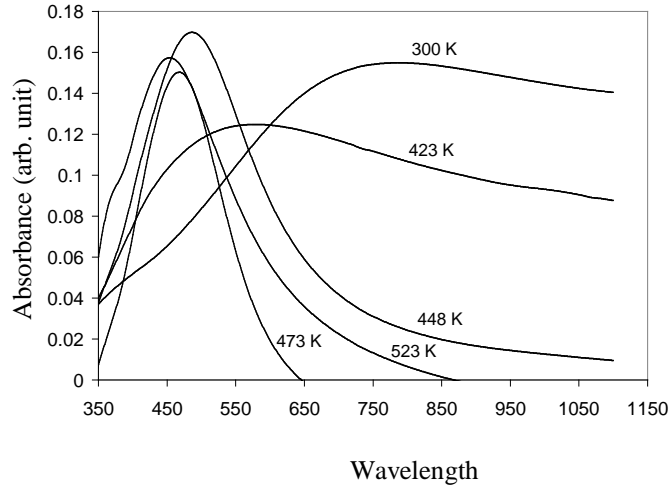


**Figure 5-6 Absorption spectra of Annealed Ag-Cu nanoparticles (surface ratio of Cu in sputter target is 7.5%)**

This can be explained as follows: for the core-shell structure, the effective dielectric constant is a function of the dielectric constant of both core and shell materials and also the volume fraction of shell layer. The SPR absorbance spectrum peak, which can be calculated from the imaginary part of polarizability, a function of effective dielectric constant, will be nearer to that of core material for shell layer volume fraction up to approximately 0.6. Detailed calculations based on equations given in literature are shown below.

The extinction coefficient of well dispersed small particles is proportional to  $\omega \text{Im}(\alpha)$ , where  $\alpha$  is the polarizability of the sphere, and  $\omega$  is the wavelength of light.  $\alpha$  can be calculated from the following equation<sup>183</sup>

$$\alpha = R^3 \frac{(\epsilon_s - \epsilon_m)(\epsilon_c + 2\epsilon_s) + (1-g)(\epsilon_c - \epsilon_s)(\epsilon_m + 2\epsilon_s)}{(\epsilon_s + 2\epsilon_m)(\epsilon_c + 2\epsilon_s) + (1-g)(2\epsilon_s - 2\epsilon_m)(\epsilon_c - \epsilon_s)} \quad (5-1)$$

where  $\epsilon_s$  and  $\epsilon_c$  are the dielectric constants of core and shell materials respectively,  $R$  is the radius of nanosphere,  $\epsilon_m$  is the dielectric constant of medium and  $g$  is the volume

fraction of shell layer. Based on the above equation, extinction spectra is calculated for 20 nm Ag-Cu core shell nanosphere (Figure 5-7).

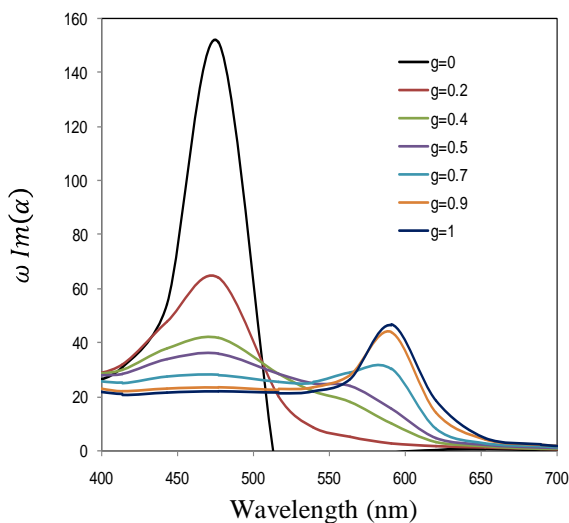


**Figure 5-7** Calculated extinction spectra for the Ag-Cu core-shell (Ag in core and Cu in shell) materials at different shell layer thickness.

Luminescence intensity of both Alexa Fluor 594 and Alexa Fluor 488 was observed to increase significantly at the vicinity of these Ag-Cu nanoparticles (Figure 5-9 D and 5-9 F). Enhancement ratio was calculated by comparing luminescence intensity of the sample with the luminescence intensity of the luminophore coated on a 3-(aminopropyl)triethoxysilane (APS) coated glass cover slip. As shown in Figure 5-8, the SPR spectrum of the 448 K annealed Ag-Cu nanoparticles nicely overlaps both the excitation and emission spectra of Alexa Fluor 488. This annealed Ag-Cu nanoparticle platform results in very strong enhancement ( $141 \pm 19$  times) of luminescence of Alexa Fluor 488 (Figures 5-9 C and 5-9 D). The Ag-Cu nanoparticles annealed at 298 K, which show less spectral overlap, also result in substantial enhancement ( $100 \pm 10$  times). The lowest enhancement ( $50 \pm 11$ ) was observed at the proximity of pure Ag nanoparticles

(deposited at the same conditions as Ag-Cu nanoparticles), for which the spectral overlap is least.

The effect of spectral overlap on luminescence enhancement is also pronounced for Alexafluor 594. We found  $23 \pm 12$  times enhancement of emission from Alexa Fluor 594 at the proximity of room temperature grown Ag-Cu nanoparticles (Figures 5-9 E and 2 F). On the other hand, both pure Ag nanoparticles and the 448 K annealed Ag-Cu nanoparticles grown at similar conditions result in lower enhancements ( $9 \pm 1$  times for 448 K annealed Ag-Cu nanoparticles and  $6 \pm 3$  times for Ag particles) because of less spectral overlap. The best case Ag-Cu studied was 2.8 times better than pure Ag for Alexafluor 488 and 3.5 times better for Alexafluor 594. In both cases, the spectral overlap was largest when maximum enhancement was seen. It is possible to achieve this enhancement for the alloy particles because the breadth of the peak can also be tuned. Please note the average intensity of luminophores coated on glass slide is near to 0 but not 0 (around 150 in the scale shown in Figure 5-9).

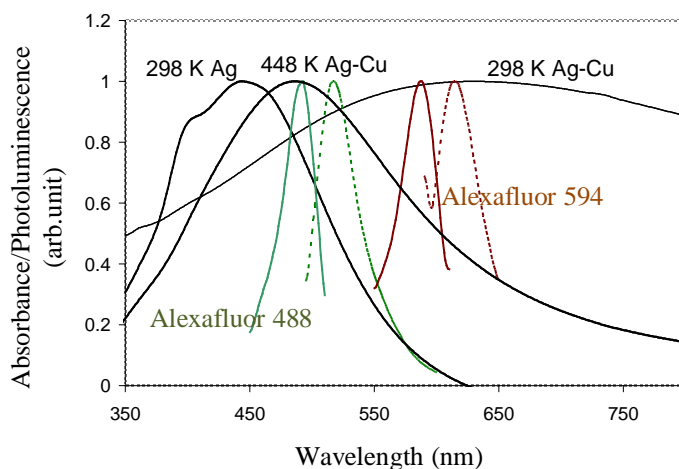


**Figure 5-8 SPR spectrum of Ag-Cu and Ag nanoparticles used for MEL and excitation and emission spectrum of Alexa Fluor 594 and Alexa Fluor 488.**

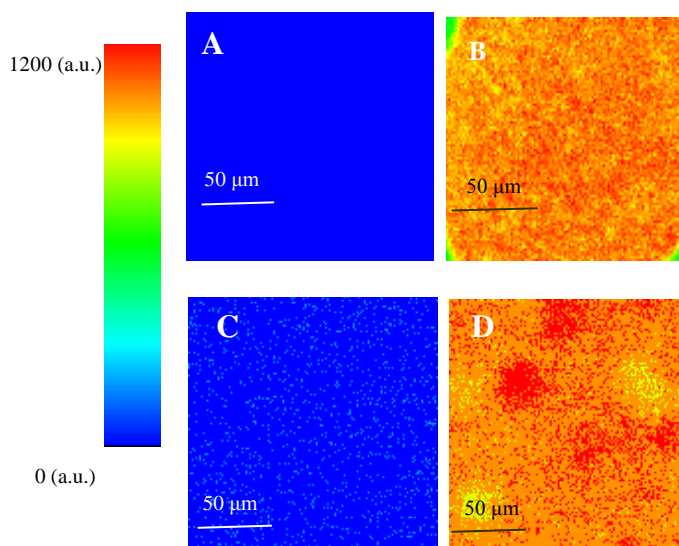


**Figure 5-9 Image of Alexa Fluor 488 coated on (A) glass (B) 448 K annealed Ag-Cu . Alexa Fluor 594 coated on (C) glass (D) 298 K Ag-Cu.**

Possible differences in protein binding to glass and Ag and Ag-Cu nanoparticles may lead to increased fluorescence signals. The difference in protein binding may arise due to the difference in hydrophobicity, as protein adsorption increases with hydrophobicity of surface when factors like electrostatic and hydrogen bonding are not pronounced.<sup>184</sup> Where Ag and Cu surfaces are usually hydrophobic in nature, the oxide layers formed on these usually reduce their hydrophobicity.<sup>185</sup> The glass slides were coated with APS to promote their hydrophobicity. Higher surface area available for nanoparticles also can increase the protein adsorption. In this work, both the glass and the nanoparticles samples were coated with very less concentration of protein (7 nanogram/mm<sup>2</sup>) and sufficient time was allowed for the absorption of the protein. This enhances the possibility of complete immobilization of the protein on the surface and may reduce the difference in amount of protein binding in glass and nanoparticles samples. In the present work the protocol described by Matveeva et al.<sup>177</sup>, has been

followed for coating fluorophore conjugated protein on both glass surface and nanoparticles surface. They reported that the protein binding to the Ag nanoparticles surface is approximately 20–30% better than the glass surface.<sup>177</sup> We expect the difference of amount of protein binding between nanoparticles surface and glass surface should be even lower in present case, as the glass surface was coated with hydrophobic APS.<sup>2</sup> Hence, this small difference in protein binding itself cannot explain the large fluorescence enhancement observed on the Ag-Cu and Ag surface. However, exact estimation of differences between the proteins adsorption between the glass and the nanoparticles surface, which is beyond the scope of this study, may facilitate the more accurate prediction of enhancement factor.

By enhancing the local field for absorption and/or quantum yield due to radiative and non radiative decay rates, we can increase the intensity of luminescence. The intensity of the incident optical wave is enhanced in the near field of the nanoparticles at the SPR wavelength. Hence, strongest excitation should be observed when the SPR spectrum of nanoparticles overlaps the excitation peak of the luminophore<sup>24</sup>. Same as for excitation, when SPR spectrum of the nanoparticles overlaps the emission spectrum of luminophore, emission intensity enhancement should be the highest<sup>179</sup>. However, as in this case high quantum yield luminophores were used, excitation enhancement should be more pronounced than emission enhancement. As a result, the spectral overlap with excitation spectra should be more important.

**Table 5-1 Fluorescence enhancements of Alexa Fluor 488 and Alexa Fluor 594 on the Ag and Ag-Cu nanoparticles.**

	Size	SPR peak	Enhancement ratio for Alexa Fluor 488	Enhancement ratio for Alexa Fluor 594
Ag nanoparticles annealed at 298 K	$13.78 \pm 3.12$ nm	444 nm	$50 \pm 11$	$6 \pm 3$
Ag- Cu bimetallic nanoparticles annealed at 298 K	$14.77 \pm 5.4$ nm	631 nm	$101 \pm 10$	$24 \pm 12$
Ag-Cu bimetallic nanoparticles annealed at 448 K	$13.88 \pm 4.07$ nm	486 nm	$142 \pm 19$	$10 \pm 1$

Here, we present a theoretical calculation for overall quantum efficiency factors in the proximity of pure Ag nanoparticles and for the 1:1 Ag-Cu nanoparticles, based on the model suggested by Kümmerlen *et al.*<sup>33</sup> which includes both excitation and emission enhancement factors (detailed computational methodology is given in the supplementary information). Exact representation of experimental conditions is not possible in theoretical calculations due to the differences in experimental geometry (nanoparticles are not in a homogeneous dielectric environment, all the nanoparticles are not of spherical shape and not of the same size, luminophore-nanostructures separation distance is not uniformly the same). Furthermore, accurate dielectric constants of room temperature and annealed Ag-Cu nanoparticles are not known, or evaluable, as they remain phase separated. However, these calculations provide some insights into the experimental findings.

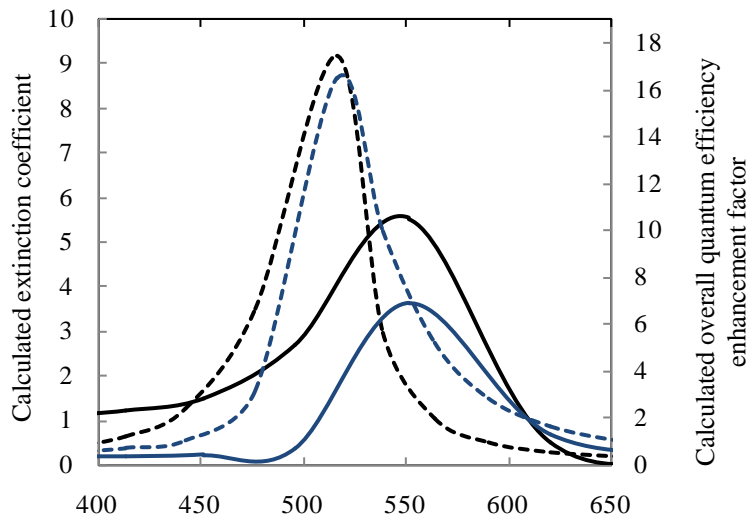


**Figure 5-10** Calculated extinction coefficient (black) and overall quantum efficiency enhancement ratio for (blue) Ag (dotted line) and 1:1 Ag-Cu nanoparticles (solid line).

Figure 5-10 shows the theoretically calculated extinction coefficient (using Mie theory), and the overall quantum efficiency enhancement factor for pure Ag and 1:1 bimetallic Ag-Cu nanoparticles. From Figure 5-10, the effect of spectral overlap is clearly evident. In the wavelength range of 450 nm to 555 nm, as the extinction spectrum for the Ag nanoparticles is more pronounced, overall quantum efficiency enhancement in the proximity of the Ag is better than that of the Ag-Cu nanoparticles. Most importantly, in the wavelength range of 555 nm to 605 nm, the Ag-Cu nanoparticles show better overall quantum efficiency enhancement than pure Ag as the spectral overlap is better for the Ag-Cu nanoparticles. For both Ag nanoparticles and Ag-Cu nanoparticles, the maximum overall quantum efficiency enhancement wavelengths are slightly red-shifted with respect to the extinction coefficient peaks. As the calculations were done for the high quantum yield (0.5) luminophore, the excitation enhancement effect is more pronounced than the emission enhancement effect. The theoretically calculated emission

enhancement factor and excitation enhancement factor are separately shown in Figure 5-11. These theoretical findings help in interpreting our experimental observations.

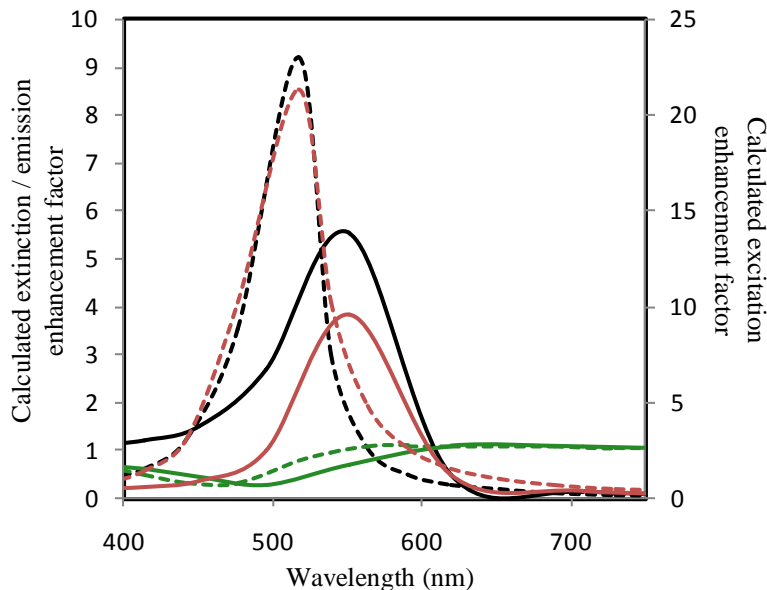


**Figure 5-11** Calculated extinction coefficient (black), Emission enhancement factor (green) and excitation enhancement factor (red) for Ag (dotted line) and 1:1 Ag-Cu nanospheres (solid line).

#### 5.4. Conclusions

In summary, the MEL effect of Ag-Cu alloy nanoparticles has been explored in this work. Ag-Cu alloy nanoparticle platforms were found to produce strong enhancement for the two luminophores studied, *viz.* Alexa Fluor 488 and Alexa Fluor 594. The effect of spectral overlap on luminescence is explored in this work. A synthesis technique to tune the SPR spectrum of alloy nanoparticles from infrared to visible region very easily by changing composition or annealing schedule is presented. Ag-Cu alloy nanoparticles were observed to show even better enhancement than pure Ag nanoparticles when the SPR spectrum was tuned to result in maximum spectral overlap. For a particular luminophore, we can tune the annealing temperature of particular

composition Ag-Cu nanoparticles to result in maximum spectral overlap which can help in optimum luminescence enhancement. We expect our study to motivate exploration of other alloy nanoparticles for MEL based applications.

## Chapter 6 - Quenching of Fluorescence from CdSe/ZnS Nanocrystals near Copper Nanoparticles in Aqueous Solution

### 6.1. Introduction

The emission of luminescent probes is modified significantly at the close proximity of metal surfaces and nanoparticles. Using nanoparticles, it is possible to both enhance and quench the emission of luminescent probes. Luminescence quenching by metal nanoparticles has been studied mostly using gold nanoparticles.<sup>43,55,57-59</sup> Gold nanoparticles can show both static and dynamic quenching effect.<sup>189</sup> The gold nanoparticles can quench the fluorescence of different fluorophores due to different reasons like resonance energy transfer, formation of static quenching complex and internal electron transfer.<sup>189</sup> Luminescence quenching due to Förster resonance energy transfer (FRET) from the excited state of the luminophore molecule (donor) to the surface plasmons of the metal nanoparticles (acceptor) depends on the spectral overlap of the acceptor's absorption with the donor's emission, and sensitivity depends on the separation distance between acceptor and donor.<sup>55</sup> Quenching effect due to Förster energy transfer decreases with the cube of separation distance.<sup>56</sup> The quenching effect of metal nanoparticles due to resonance energy transfer is decided by several properties of the nanoparticles like dielectric constant, size and shape.

Quenching of luminescence due to the proximity of nanoparticles has been utilized for many different applications. Quenching resulting due to metallic nanoparticles has been successfully utilized for the improvement of homogeneous and competitive fluorescence immunoassay<sup>156,157</sup>, optical detection of DNA hybridization<sup>158</sup>, competitive hybridization assay,<sup>159</sup> and in optoelectronics<sup>160</sup>. Recently, many researchers have utilized the quenching effect of gold nanoparticles on nanocrystal quantum dots for biological and solar cell applications.<sup>184-186</sup> However the widespread application of luminescence quenching requires exploration of cheaper metals.

Imaginary component of the dielectric constant of copper is comparable to that of gold in the wavelength range of 400 nm to 500 nm, and almost twice in the wavelength range of 500 nm to 625 nm. Hence, it is expected that Cu nanoparticles will show similar or better quenching effects in comparison to gold nanoparticles in these wavelength ranges due to ohmic losses. In our previous study we reported quenching of luminophore Cy3 in the vicinity of Cu nanoparticles platform. However, the quenching effect of Cu nanoparticles on fluorophores in solution is yet to be explored. Details of the quenching mechanism are also not fully understood. The observation that Cu nanoparticles efficiently quench the emission from the fluorophore suggests that Cu nanoparticles might serve as efficient quencher of different other luminophore. We study the quenching effects of Cu nanoparticles on the fluorescence emission from different sizes of CdSe/ZnS nanocrystals, a commonly used quantum dot in biological applications. We observe the effect of Cu-nanoparticle concentration on quenching.

In this work, to understand the quenching mechanism, we have studied both static and dynamic quenching effects of Cu nanoparticles. Two sets of fluorescence quenching

experiments were performed. In the first set of experiments we have studied the dynamic quenching effect of Cu nanoparticles on the emission of CdSe/ ZnS nanocrystals. For this dynamic quenching study, Cu nanoparticles coated with PVP were synthesized. These Cu nanoparticles have no functional binding sites to bind with the mercaptoundecanoic ligands coated CdSe/ ZnS nanocrystals thus the quenching should be purely collisional quenching. In the second set of experiments, we have studied the effect of different size CTAB coated Cu nanoparticles on the luminescence of mercaptoundecanoic ligands coated CdSe/ ZnS nanocrystals. In this case, electrostatic binding between cationic Cu nanoparticles and anionic CdSe/ZnS nanocrystals is possible, thus can result in static quenching.

Cu nanoparticles of variable sizes have been studied to observe the effect of size on their quenching effect on luminophores. There are few studies to see the effect of gold nanoparticles size.<sup>59,189</sup> These studies are suggestive but in some case provide contradictory information. For example Ghosh *et al.*<sup>59</sup> studied the quenching effect of gold nanoparticles of size ranging from 8 nm to 73 nms and suggested that with the increase in nanoparticles size the quenching effect reduces. On the other hand, Cheng *et al.*<sup>189</sup> have observed the opposite effect for Au nanoparticles having core diameters from 1.3 to 3.9 nms on the luminophore [Ru(bpy)3]2+. They found quenching effect increases with the increase in size. Dulkeith *et al.*<sup>55</sup> found a size-dependent increase in nonradiative decay rate and a decrease in the radiative rate in case of the quenching of lissamine dye attached to a Au nanoparticle. In our study, we have used the theoretical calculation based on improved Gersten-Nitzan model to provide better insight into the size dependence of quenching by metallic nanoparticles. The Gersten-Nitzan (GN) model

<sup>93,95,96</sup> provides insights into the influence of proximal metal nanospheres on radiative and non-radiative decay rates of luminophore molecules. The GN model can be used to interpret both luminescence enhancement and quenching effects of metallic nanoparticles.<sup>55,93</sup> According to this model, the electromagnetic interaction between luminophores and metal nanoparticles results in the increase of both radiative and non-radiative decay rates, depending upon the luminophore-nanoparticle separation distance and the properties of the nanoparticle (size, shape and dielectric constant), which decide the scattering and surface plasmon resonance behavior of the nanoparticle. Mertens *et al.*<sup>93,96</sup> have corrected the GN model to account for radiation damping and dynamic depolarization.

## 6.2. Experimental

### 6.2.1. PVP Coated Cu Nanoparticles Synthesis

Stable Cu-nanoparticle colloid solutions were synthesized using the process described by Wu *et al.*<sup>190</sup> Copper (II) acetate hydrate (98%) and polyvinylpyrrolidone (PVP of molecular weight 55,000) were obtained from Sigma-Aldrich, and used as-received. An aqueous solution of 0.8 M PVP and 0.4 M L-ascorbic acid (reagent grade, fine crystal, Fisher Scientific) were mixed with an aqueous solution of 0.01 M copper salt and 0.8 M PVP in 1: 1 volume ratio under constant stirring at 45 °C without any inert gas protection. The reaction was then allowed to continue for 1 hour before bringing the system down to room temperature. The initial precursor solution of light blue color

changes to a red colloidal slurry. Then, the solution was diluted with ethanol and centrifuged. The supernatant was rejected to remove excess PVP, unconverted salts and by-products. This centrifugation was repeated 4 times and the precipitated red Cu nanoparticles were collected and dispersed in deionized water at room temperature.

### 6.2.2. CTAB Coated Cu Nanoparticle Synthesis

CTAB coated Cu nanoparticles were synthesized using a method described in literature.<sup>191</sup> Hydrazine, cupric chloride and cetyltrimethylammonium bromide (CTAB) were obtained from Sigma-Aldrich. Equal volume of two aqueous solutions of CTAB, one containing hydrazine (.02-.04 M) and other containing cupric chloride (.001 M ) were mixed together at room temperature. The pH of cupric chloride and CTAB solution required to be maintained at 10 to avoid the oxidation of Cu nanoparticles.  $\text{NH}_4\text{OH}$  was added to this solution to maintain the pH. Cu nanoparticles synthesis completed after about 2 hours. By varying the concentration of hydrazine different size Cu nanoparticles were obtained.

### 6.2.3. Nanoparticles Characterization

Shape and size of the nanoparticles was observed and characterized by transmission electron microscopy (FEI Morgai 268D). An UV-vis spectrometer (JASCO, V-530) was used for measuring the light absorption spectra attributed to the SPR of these nanoparticles. TEM samples were prepared by dispersing a few drops of the Cu nanoparticle solution on a carbon film supported by molybdenum grids.

#### 6.2.4. Fluorescence Quenching Experiment

Three different CdSe/ZnS nanocrystals coated with mercaptoundecanoic ligands (green, orange and red) were purchased from NN-Labs, Fayetteville, AR. The solution of Cu nanoparticles was added to the 500 nanomol solution of nanocrystals in a required mole ratio and the spectral changes were monitored immediately. Fluorescence spectra of the samples were recorded on an ISS PC1 photon counting spectrofluorimeter.

### 6.3. Results and Discussion

#### 6.3.1. Characterization of PVP Coated Copper Nanoparticles

At the time of synthesis of the Cu nanoparticles, ascorbic acid serves as both reducing agent and antioxidant to reduce copper salt precursor and prevent further oxidation of synthesized Cu nanoparticles. In the aqueous solution, the absorbance peak of the copper nanoparticles is around 588 nm. Intensity and position of this absorbance peak for Cu nanoparticles in aqueous solution did not show any significant change for at least 5 days which indicates that these nanoparticles are stable. Transmission electron microscopy of the Cu nanoparticles indicated the average size to be  $10.11 \pm 3.6$  nm (Figure 6-1 (A)) and the average size of red CdSe/ZnS nanocrystals was determined to be  $7.63 \pm 0.83$  nm (Figure 6-1(B)). STEM EDS data (Figure 6-1 (C)), confirm that the nanoparticles are comprised of only Cu and oxidation is negligible.

### 6.3.2. Collisional Quenching by PVP Coated Copper Nanoparticles

These Cu nanoparticles have no functional binding sites to bind with CdSe/ZnS nanocrystals with mercaptoundecanoic ligands so the quenching should be collisional quenching. The CdSe/ZnS nanocrystals were mixed with the PVP stabilized copper nanoparticles in aqueous solution.

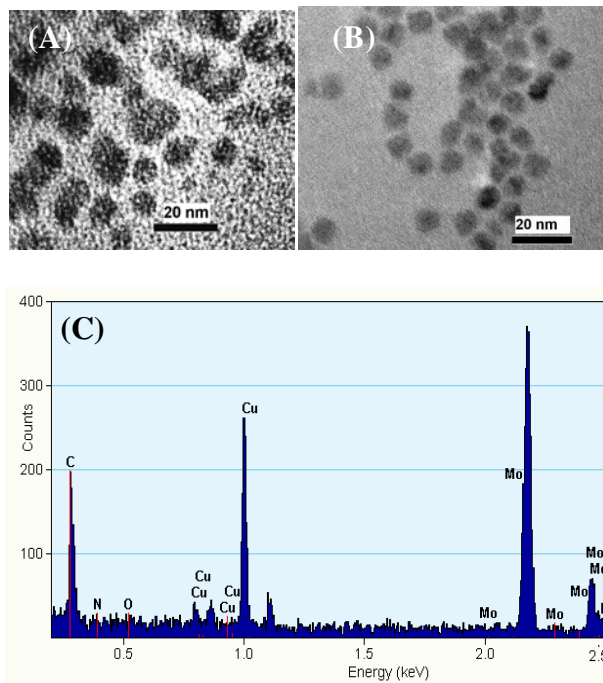


**Figure 6-1 (A) HRTEM micrograph of (A) Cu nanoparticles (B) Red CdSe/ZnS nanocrystals, and (C) STEM EDS spectra of the Cu nanoparticles.**

Figure 6-2 shows the absorbance spectrum attributed to SPR of Cu nanoparticles and the emission spectra of green, red and yellow CdSe/ZnS nanocrystals. The absorbance spectrum of Cu nanoparticles overlaps only with the emission spectrum of yellow CdSe/ZnS nanocrystals. Fluorescence from the yellow nanocrystals displayed significant quenching upon conjugation with copper nanoparticles.

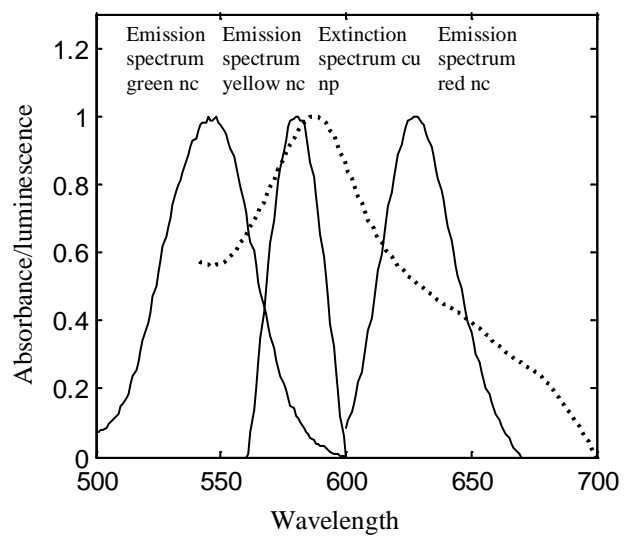


**Figure 6-2 Normalized absorbance spectrum of copper nanoparticles and luminescence spectra of CdSe/ZnS nanocrystals.**

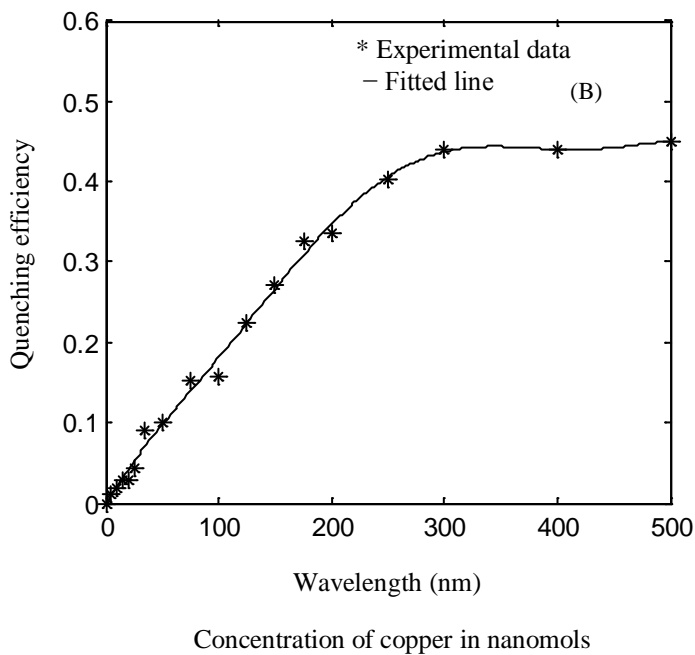
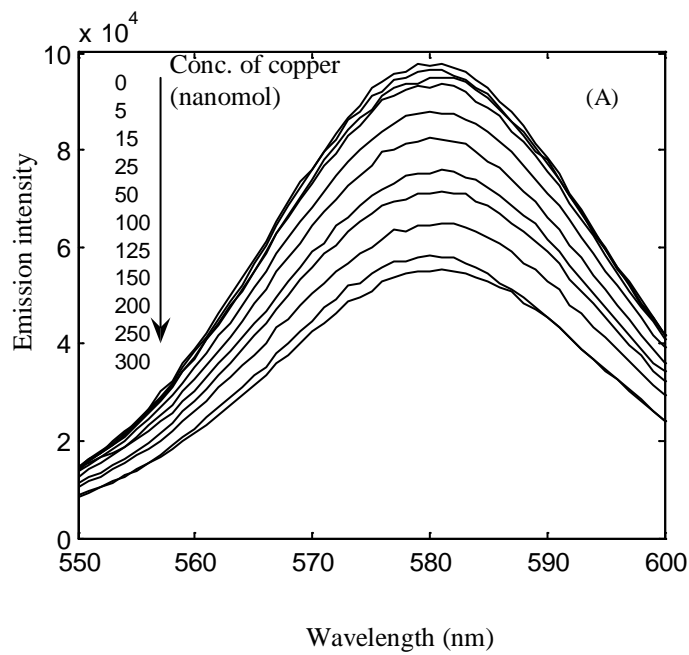


**Figure 6-3 (A) The emission spectra of yellow nc at different concentration of Cu nanoparticles. (B) Quenching efficiency measured at 580 nm.**

These experimental results revealed that quenching is sensitive to nanomol range concentration of copper nanoparticles (Figure 6-3(A)). The emission wavelength remained the same but the intensity of CdSe/ZnS nanocrystals decreases with the

concentration of copper nanoparticles. The quenching efficiency of yellow nanocrystals estimated on the basis of emission intensity and shown in Figure 6-3(A) and Figure 6-3(B), shows a significant increase and reaches an asymptotic value at the nanoparticle concentration of 300 nM. Most of the nanocrystals have been quenched at a molar ratio of metal nanoparticles/yellow nanocrystals of 0.6. Interestingly, in the range of 0 to 250 nanomols, quenching efficiency of yellow CdSe/ZnS nanocrystals shows almost linear behavior with copper concentration.

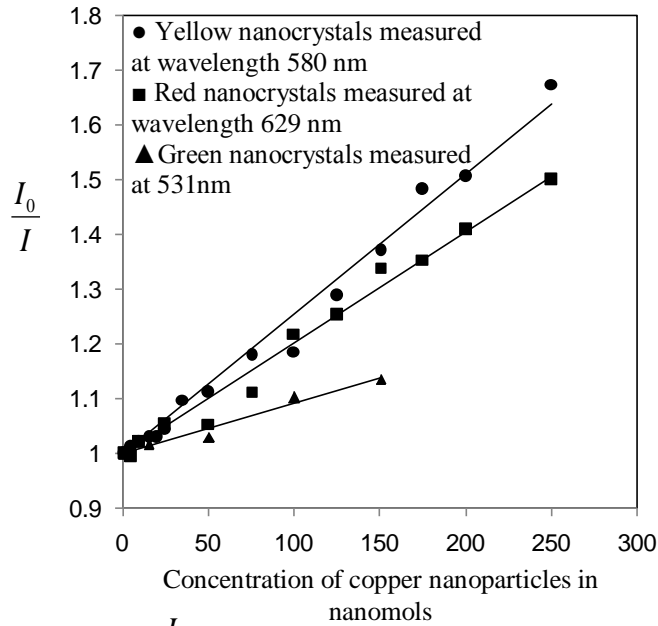


**Figure 6-4** Stern-Volmer plot of  $\frac{I_0}{I}$  for 500 nanomolar concentration of CdSe/ZnS nanocrystals vs. concentration of copper nanoparticles.

Figure 6-4 shows that the fluorescence quenching of CdSe/ZnS nanocrystals follows the linearity of Stern-Volmer (SV) equation,

$$\frac{I_0}{I} = 1 + K_Q [C_Q] \quad (6-1)$$

Where  $I_0$  is the luminescence intensity in the absence of quencher molecules,  $Q$  represents the quencher and  $[C_Q]$  is the concentration of quencher molecules.  $K_Q$  is the

Stern-Volmer constant. This can be attributed to the fact that, at dilute acceptor concentration, Forster kinetics approach the SV limit.<sup>192</sup> We can also see from Figure 6-4 that the SV constant is higher for yellow nanocrystals (compared to those of the red and green nanocrystals) for which the emission spectrum has maximum overlap with the absorption spectrum of Cu nanoparticles. This phenomenon is consistent with the FRET theory that the fluorescence quenching efficiency increases with the increase in spectral overlap of the donor's emission with the acceptor's absorption.

### 6.3.3. Characterization of CTAB Coated Cu Nanoparticles

Three different size nanoparticles samples a, b and c were synthesized varying the concentration of hydrazine. With the increase in concentration of hydrazine the size of copper nanoparticles decreased. Figure 6-5 (A-C) shows the TEM micrographs of these three different size nanoparticles. From the TEM images of the CTAB coated Cu nanoparticles the average size of these nanoparticles were obtained. The absorbance spectra, attributed to SPR of different sizes Cu nanoparticles are given in figure 6-6.

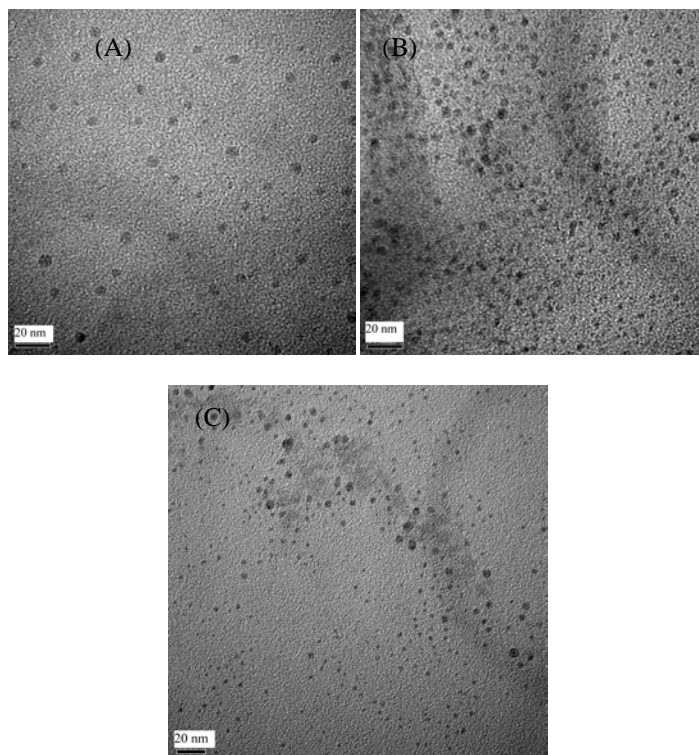


**Figure 6-5** High resolution TEM images of different sizes CTAB coated copper nanoparticles (A) sample a (B) sample b and (C) sample c

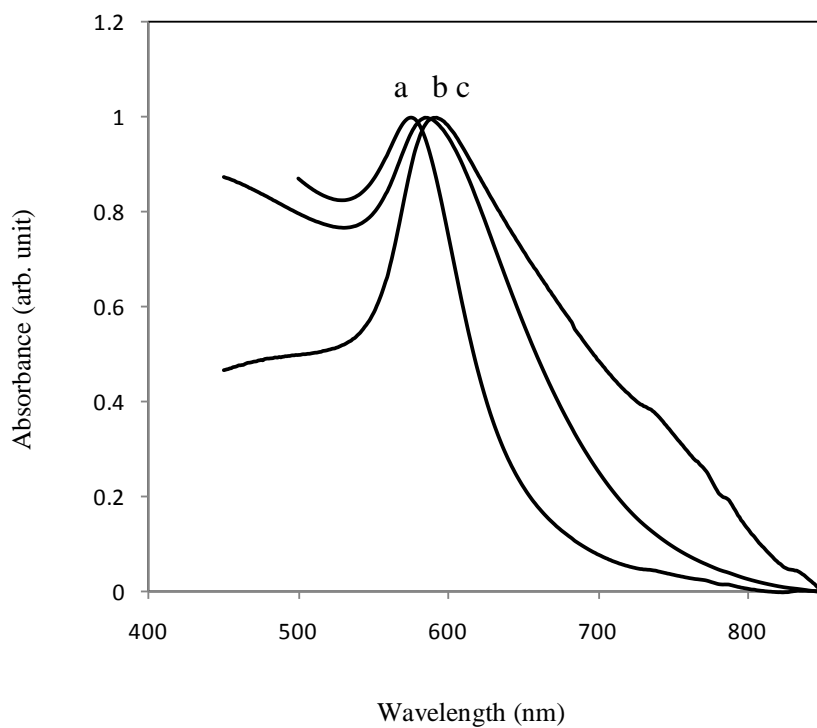


**Figure 6-6** Normalized absorbance spectra of different size Cu nanoparticles in aqueous solution.

Table 6.1 summarizes the concentration of precursor and the reducing agents used for synthesizing samples a, b and c and the resulting sizes of nanoparticles and their absorption peaks. With the increase in Cu nanoparticle size the absorbance peak redshifts. Typical absorption peak for copper oxide around 800 nm is not seen confirming the negligible formation of copper oxide.<sup>193</sup> These copper nanoparticles were stable at least for 3 days. Diluting these Cu nanoparticles solution also does not oxidize the nanoparticles only the absorption intensity decreases (Figure 6-7).

**Table 6-1 Concentration of reactants and characteristics of the synthesized Cu nanoparticles**

Samples	[CuCl <sub>2</sub> ] (mole)	[N <sub>2</sub> H <sub>5</sub> OH] (mole)	[CTAB] (mole)	Size of nanoparticles (nm)	Absorbance peak (nm)
A	.001	.02	.01	6.83+/-1.00	592
B	.001	.03	.01	5.58+/-1.16	588
C	.001	.04	.01	3.71+/-1.00	574

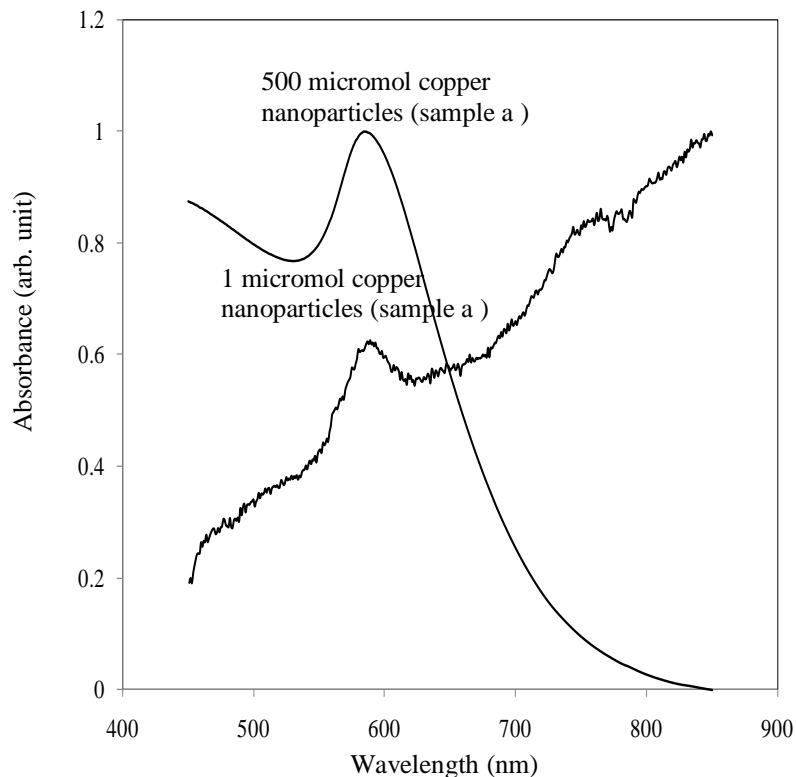


**Figure 6-7 Absorbance spectra of 500 micromol and diluted (1 micromol) copper nanoparticles.**

#### 6.3.4. Quenching Effect of CTAB Coated Cu Nanoparticles on CdSe/ZnS Nanocrystals

Luminescence of red CdSe/ ZnS nanocrystals in aqueous solution quenches in the presence of CTAB coated Cu nanoparticles (Figure 6-8). The emission intensity of 500 nanomol red CdSe/ZnS nanocrystals solution decreases with increasing concentration of Cu nanoparticles, however the peak position of emission spectra remain same. This quenching effect is sensitive to nanomol concentration of Cu nanoparticles. The fluorescence spectra shown in Figure 6-8 is solely that of CdSe/ZnS nanocrystals as Cu nanoparticles do not show any luminescence.

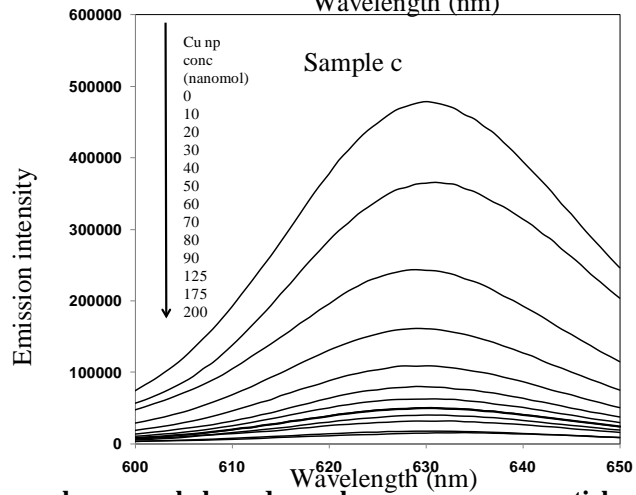
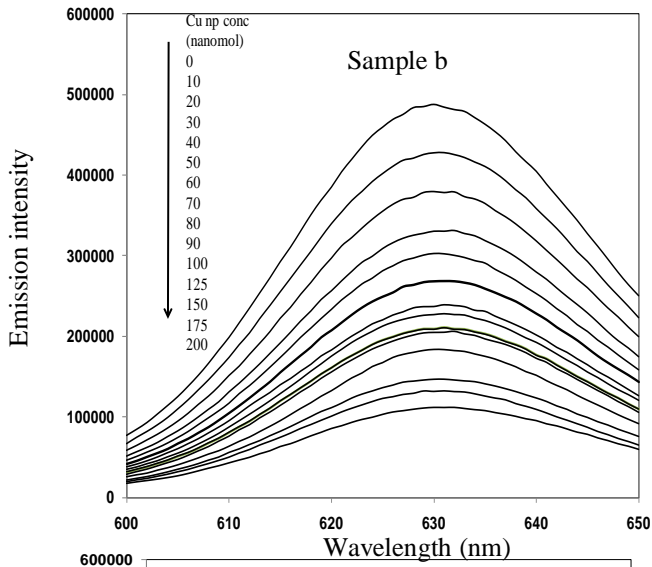
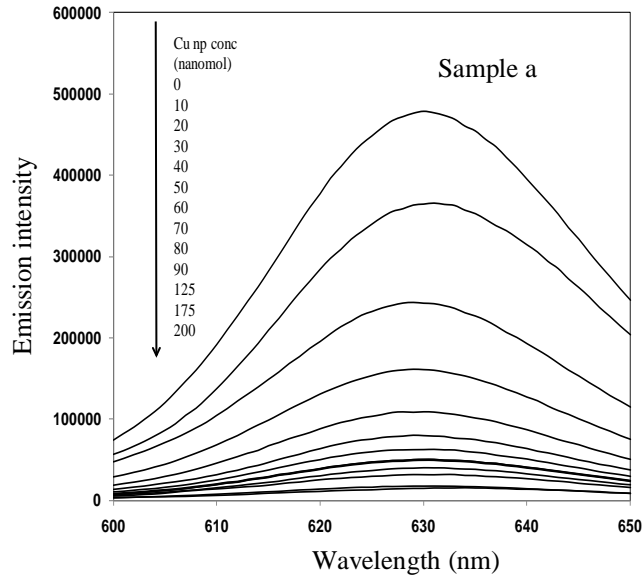


**Figure 6-8 Effect of sample a, sample b and sample c copper nanoparticles concentration on the 500 nanomol red CdSe/ZnS nanocrystals.**

Figure 6-8 shows the  $I_0/I$  plot for red CdSe/ ZnS nanocrystals for different concentration for sample a, b and c of Cu nanoparticles. In all these cases the quenching effect does not follow the linearity of Stern-Volmer plot.  $I_0/I$  vs. Cu nanoparticle concentration plots show an upward curvature towards the y-axis indicating the quenching may be due to the combination of both collisional and static quenching. In this case the modified SV equation is given below

$$\frac{I_0}{I} = 1 + (K_s + K_d)[C_q] + K_s \cdot K_d [C_q]^2 \quad (6-2)$$

where  $C_q$  is the concentration of quencher elements and  $K_s$  and  $K_d$  are static and dynamic quenching constants respectively. The above equation is fitted to the  $I_0/I$  vs. Cu nanoparticles concentration data for different size Cu nanoparticles (Figure 6-9).  $K_D$  and  $K_S$  are obtained from this fitted equation. The lower value is assigned to the dynamic quenching constant as probability of static quenching due to formation of electrostatic complex is more than probability of dynamic quenching. A second set of experiments (discussed in later sections) which deal with only dynamic quenching also give the dynamic quenching constant of same order. Quenching constants for different size Cu nanoparticles are summarized in Table 6-2.

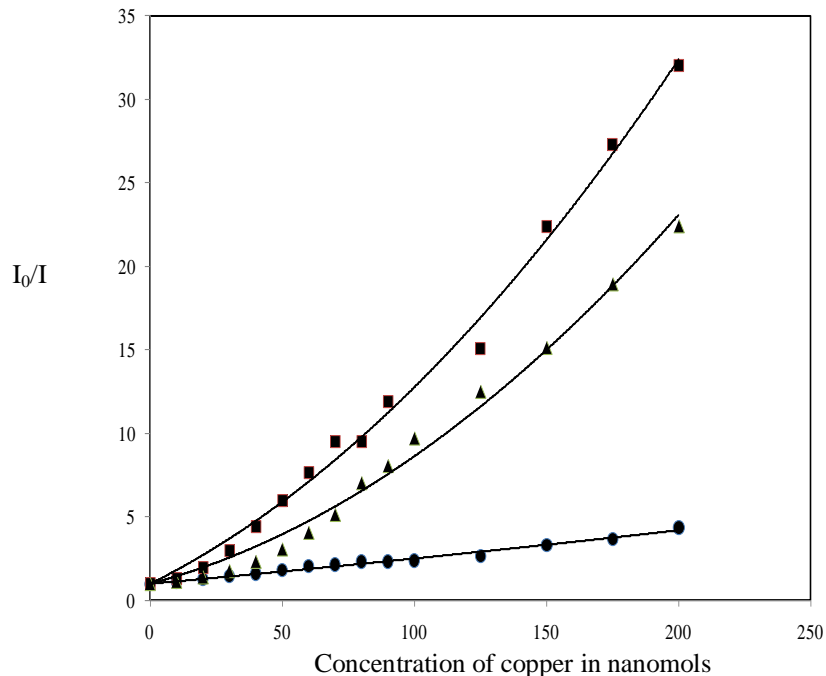


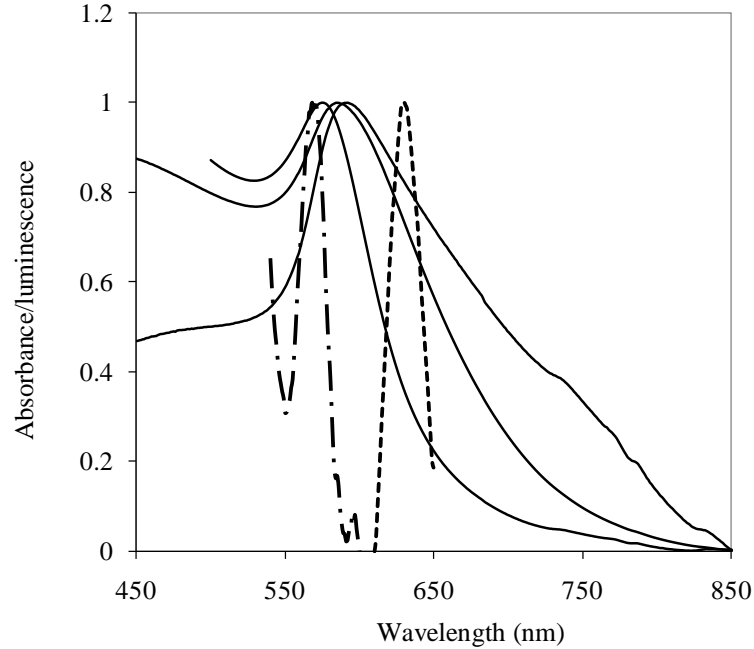
Figure 6-9 SV plot for 500 nanomolar concentration of red CdSe/ZnS nanocrystals for different size Cu nanoparticles ● sample a ▲ sample b ■ sample c

Table 6-2 Summary of SV equation and quenching constants for different size CTAB coated Cu nanoparticles

Samples	SV equation	K <sub>D</sub> (/nanomol conc.)	K <sub>S</sub> (/nanomol conc.)	Relative K <sub>D</sub> (/Cu np number)	Relative K <sub>S</sub> (/Cu np number)
A	$\frac{I_0}{I} = 1 + .0143[Q_{Cu}] + 9E - 06[Q_{Cu}]^2$	0.0006	0.01364	1.00	1
B	$\frac{I_0}{I} = 1 + .0423[Q_{Cu}] + .0003[Q_{Cu}]^2$	0.009	0.033288	8.18	0.75
C	$\frac{I_0}{I} = 1 + .0785[Q_{Cu}] + .0004[Q_{Cu}]^2$	0.006	0.06813	1.60	1.25

### 6.3.5. Quenching Mechanism and Effect of Size of Cu Nanoparticles on Quenching Efficiency

The quenching of luminescence of CdSe/ZnS by CTAB coated Cu nanoparticles may be due to the combined effect of resonance energy transfer and the formation of static quenching complexes via attractive electrostatic interactions. Resonance energy transfer from luminophores to nanoparticles requires good overlap between the emission and excitation spectra of luminophores and the absorbance spectra of nanoparticles. It is seen that in case of pure dynamic quenching (quenching of CdSe/ZnS nanocrystals by PVP coated Cu nanoparticles) the effect of spectral overlap is pronounced on the quenching efficiency confirming the possibility of resonance energy transfer. In the case of this static quenching experiment, though there is less spectral overlap between emission spectrum of red CdSe/ZnS nanocrystals and the absorbance spectra of the CTAB coated Cu nanoparticles is not large enough, large spectral overlap between the excitation spectrum of red CdSe/ZnS nanocrystals and sample C of Cu nanoparticles (showing maximum quenching effect) exists (Figure 6-9).



**Figure 6-10 Normalized absorbance spectra (-----) of different size Cu nanoparticles and the excitation (- . - .) and emission spectra (.....) red CdSe/ZnS nc.**

The results in Tables 6-2 and the quenching efficiency vs, Cu nanoparticles diameter plotted in Figure 6-11 show interesting effects of nanoparticle size on quenching. Where static quenching constants increases with the decrease in size of Cu nanoparticles, dynamic quenching constants first increase then decrease with increase in size. As Energy transfer is the most likely dominant mode of quenching in these experiments, the presence of nanoparticles not only influences the nonradiative decay rate of vicinal luminophores due to Förster energy transfer (from luminophore molecules to nanoparticles), but also affects the radiative decay rate.<sup>55</sup> This observation can be explained based on the calculation using improved GN model. Using the improved model,<sup>93,95,96</sup> we calculated the modifications of the radiative decay rate ( $\Gamma_R$ ) and total decay rate ( $\Gamma_{Tot}$ ) of the luminophores at the proximity of metal nanoparticles. The corrected GN model was used to calculate quantum efficiency change due to radiative

and nonradiative decay rate change. The calculations were done assuming the separation distance between nanoparticles and luminophore molecules to be 2.7 nm, the length of CTAB molecule as suggested in literature<sup>192</sup>. Theoretically calculated quenching of quantum efficiency of luminophore molecule due to Cu nanosphere is plotted against the size of the nanosphere in Figure 6-8. It can be seen from Figure 6-8 that there is an optimum size of nanoparticles for which quantum efficiency quenching is maximum. Spectral overlap between the absorption and emission spectra of luminophore and surface plasmon resonance spectra of metal nanoparticles is very important for resonance energy transfer<sup>24,154,168</sup>. When the size of the particle increases, the plasmon resonance is shifted to longer wavelength and broadened and decreases in magnitude due to dynamic polarization<sup>170</sup>. So, there exists an optimum diameter. Below this optimum diameter, the quenching efficiency should increase with increase in diameter and above this diameter the quenching efficiency should decrease with decrease in diameter. This explains our experimental finding that the static quenching coefficient decreases with the increase in diameter. In case of dynamic quenching, collision probability between the luminophore molecule and the nanoparticles also is an important factor. The collision probability between the nanoparticle and luminophore increases with the increase in size of nanoparticles. Since dynamic quenching efficiency depends on both effective coupling to the plasmon mode and also collisional efficiency, give rise to an optimum diameter.

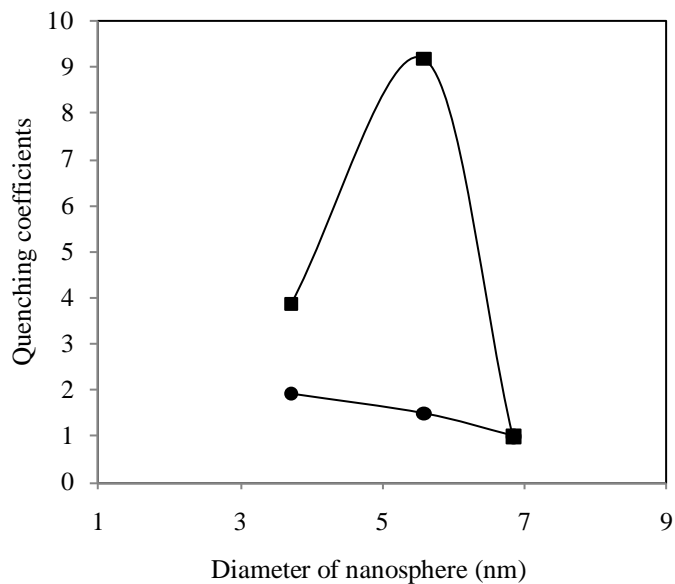


**Figure 6-11** Relative dynamic quenching constants ( $K_D$ ) (■) and static quenching constants ( $K_S$ ) (●) vs the mean diameter of Cu nanoparticles.

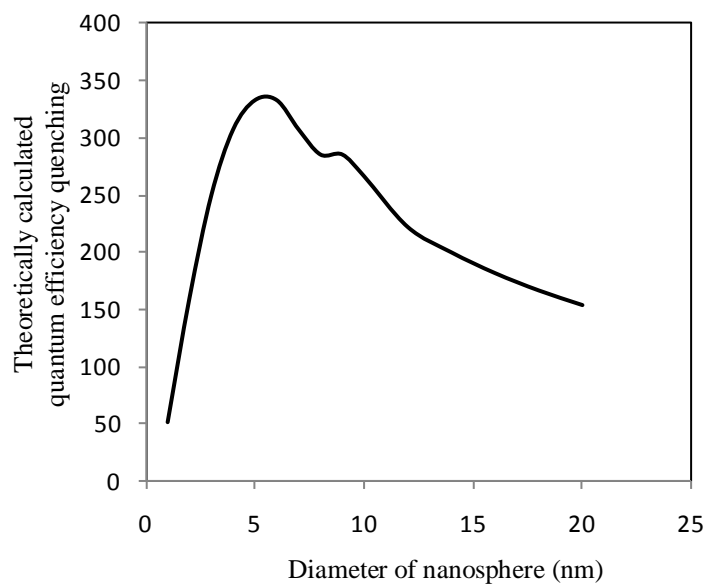


**Figure 6-12** Ratio of theoretically calculated luminescence quantum yields of a dipole emitter with and without copper metal nanosphere.

#### 6.4. Summary and Conclusions

Quenching effect of Cu nanoparticles on CdSe/ZnS nanocrystal quantum dots in aqueous solution has been explored in this work. Cu nanoparticles were found to

produce quenching for three different CdSe/ZnS nanocrystals (red, yellow and green). The luminescence of nanocrystals is sensitive to nanomolar concentrations of copper nanoparticles. Cu nanoparticles were observed to show better quenching effect when maximum spectral overlap between emission spectrum of nanocrystals and absorption spectrum of copper nanoparticles occurs suggesting quenching may be due to the resonance energy transfer from luminophore to Cu nanoparticles. This study also provides insight into the dependence of fluorescence quenching efficiency on the size of metallic nanoparticles. In this case static quenching constants were found to decrease with the increase in size of nanoparticles, however dynamic quenching constant did not show any definite trend. We used theoretical calculations based on the corrected GN model to explain our findings. These results on the quenching effect of copper nanoparticles will motivate their utilization of these nanoparticles as an inexpensive alternative to gold in many quenching based applications.

## Chapter 7 - Summary, Conclusions and Recommendations

### 7.1. Introduction

The emission intensity of luminophore molecules can either be enhanced or quenched depending on the environment. Metal nanoparticles can influence the emission intensity of vicinal luminophores depending on different factors like their orientation with respect to luminophore molecules, luminophore molecule and nanoparticles separation distance and ohmic losses of metallic nanoparticles.<sup>1-3</sup> Both enhancement and quenching have important applications in biological and sensor field.

This dissertation focused on both enhanced and quenched luminescence. In the first part of this dissertation, based on the fluorescence quenching by O<sub>2</sub> molecule, we have developed a method to measure oxygen diffusion properties in polymer using inverted fluorescence microscopy. Then, we studied enhanced and quenched fluorescence in the vicinity of alloy nanoparticles. Finally we studied fluorescence quenching of CdSe/ZnS nanocrystals in the presence of copper nanoparticles. In the following sections conclusions from these studies are presented.

### 7.2. Measurement of O<sub>2</sub> Diffusion Properties Using Inverted Fluorescence Microscopy

A fluorescence microscopy technique is developed to measure diffusion and permeation coefficients of oxygen in polymers. In this method, the microscopic level SV

responses of heterogeneous sensors can be monitored. This method allows us to distinguish the responses of background region (nearly homogeneous regions) from the region where the luminophore is aggregated. As the nearly homogeneous regions show better response to oxygen concentration and follow the linearity of SV equation, studying the response of these, one can eliminate the complexity of combining non-linear SV equation with a diffusion model. The method developed here can be applied for measuring oxygen diffusion properties in different polymers ranging from transparent to opaque and subjected to the condition that no component present in polymer interferes with the response of sensor to oxygen concentration and is also suitable for polymer composite. We also developed a new and simple quasi steady model for describing diffusion phenomena in the case of accumulation in volume technique, which can be applied for any other diffusion experiments.

### 7.3. Ag-Cu Nanoparticles for Enhanced Luminescence

In this part, we show that photoluminescence intensity can be enhanced in the vicinity to Ag-Cu alloy nanoparticles. In the first case, different composition Ag-Cu nanoparticles were synthesized by polyol synthesis method. The observed luminescence enhancement depends on the composition of Ag-Cu nanoparticles. It was found that with the increase of Cu percentage the luminescence enhancement decreases and finally pure Cu nanoparticles quench the fluorescence. This is attributed to the fact that, the imaginary component of the dielectric constant of copper is significantly larger (more than twice) than that of silver in the wavelength range of 300 nm to 600 nm. It is expected that in this wavelength range, due to higher ohmic losses, Cu nanoparticles will

mostly quench the luminescence at close proximity in contrast to the enhancement effect of Ag nanoparticles.

In the second part, we synthesized Ag-Cu nanoparticles using sputtering deposition and then tune their SPR spectra from visible to infra-red region by annealing. This allows us to see the effect of SPR spectra of Ag-Cu nanoparticles on the vicinal luminophores. We have found that with the spectral overlap between SPR spectra of nanoparticles and the emission and absorption spectra of luminophores, large metal enhanced luminescence is achieved (order of 100). Interestingly, when the spectral overlap with Ag-Cu nanoparticles is better, these nanoparticles show even better enhancement than pure Ag nanoparticles. This study establishes the importance of spectral overlap for metal enhanced luminescence.

In both of the above cases the experimental findings are supported by the theoretical calculations using an improved Gersten Nitzan model.

#### 7.4. Fluorescence Quenching by Cu Nanoparticles

Cu nanoparticles were found to be efficient quencher of fluorescence of CdSe/ZnS quantum dots in aqueous solution. Cu nanoparticles can participate in both static and dynamic quenching and the nanomole concentration of the Cu nanoparticles can also result in quenching effect. It was found that the quenching efficiency of Cu nanoparticles depends on the spectral overlap between SPR spectra of Cu nanoparticles and excitation and emission spectra of quantum dots. This suggests that the fluorescence quenching by Cu nanoparticles may be due to resonance energy transfer from the quantum dots to Cu nanoparticles. Furthermore, it was found that the quenching effect

by Cu nanoparticles significantly depends on the size of Cu nanoparticles. We hope our study will motivate the use of Cu nanoparticles in many fluorescence quenching based applications.

## 7.5. Major Contributions

The contributions of this dissertation to the field of luminescence sensor research are multifold. For the first time, the present work has explored the effect of alloy metal nanoparticles on the luminescence intensity of vicinal luminophores. This study finds that the tunable optical property of alloy nanoparticles sometime make them better candidates for metal enhanced luminescence in comparison to pure metal nanoparticles. This study also provides fundamental understanding of the effects of surface plasmon resonance properties of metal nanoparticles on metal enhanced luminescence. The outcome from the present research can be utilized to improve luminescence sensor design and produce sensors having enhanced signal to noise ratio, resolution and detection sensitivity. An opportunity to enhance the luminescence of sensors is likely to improve a wealth of biomedical and biochemical application including single molecule detection, DNA sequencing, medical diagnostics, genomics. Improved luminescence will also facilitate fabrication of improved emissive devices, such as lasers or organic light-emitting diodes (OLEDs). The findings of this research are not only beneficial for metal enhanced luminescence applications, but also provide a good platform for the study of other SPR based applications.

Finally, we have introduced Cu nanoparticles to quench the emission intensity of vicinal luminophores. The fluorescence of quantum dots is even sensitive to nanomol

concentration of Cu nanoparticles. This finding should motivate the application of quenching effect of Cu nanoparticles in different biological sensing methods.

## 7.6. Future Directions

Based on the findings of the current research the following possibilities exist which could lead to many worthwhile and interesting projects. The details are discussed in this section.

### 7.6.1. Fluorescence Microscopy for Simultaneous Imaging and O<sub>2</sub> Diffusion Measurement

Extension of fluorescence microscopy technique established in this work, to the measurement of O<sub>2</sub> diffusion coefficient in biological samples simultaneously with imaging will be a meritorious project to pursue. This project is particularly interesting because of following reasons. Fluorescence microscopy is already very popular for imaging different biological samples like cell, tissue, microbes and biofilms. Understanding how these biological samples react to different concentration of oxygen is very essential to understand in some cases. For example, simultaneous monitoring molecular oxygen concentration and imaging of tissue is an important part of photodynamic therapy. Recent studies also address the significance of oxygen concentration heterogeneities within a cell in health and disease.<sup>1-4</sup> Simultaneous monitoring of oxygen concentration in microenvironment and their effect on metabolic activity of different microbial communities is also very important. However the

technique for two dimensional monitoring of O<sub>2</sub> concentration and imaging is yet to be fully established.

#### 7.6.2. Exploration of Other Alloy Nanoparticles for Metal Enhanced Luminescence

We expect our study of metal enhanced luminescence by Ag-Cu alloy nanoparticles will motivate further studies of other alloy nanoparticles for MEL based applications. For example, silver-gold alloy nanoparticles can be an interesting candidate to study for MEL based application as silver-gold alloy nanoparticles eliminate the oxidation problem of pure silver nanoparticles and their surface plasmon resonance property can be manipulated by tuning their composition.

#### 7.6.3. Application of Alloy Nanoparticles for Enhancement of Photovoltaic Cells

Decreased absorbance of light and lower energy conversion efficiency are sometime major limitations of thin film solar cells for example amorphous silicon solar cells, GaAs solar cells and dye sensitized solar cells.<sup>5,6</sup> Scattering from noble metal nanoparticles excited at their SPR and near field concentration of light can increase the light absorption and light trapping in the photovoltaic cell, thus can enhance the efficiency.<sup>7</sup> Easy tunability of SPR wavelength of nanoparticles will be very designable property of metallic nanoparticles for enhancing the efficiency photovoltaic cell. This proposed work can exploit the scientific principles of tunable SPR properties of Ag-Cu alloy nanoparticles established in the present work for the efficiency enhancement of photovoltaic cells.

#### 7.6.4. Development of Sensors Based on the Quenching Property of Cu Nanoparticles

It was found in the present work that Cu nanoparticles can efficiently quench the fluorescence intensity of quantum dots and the quenching is nanomol concentration sensitive. This could be utilized to develop different biological sensors for detecting DNA hybridization and immunoassay.

#### 7.6.5. Theoretical and Computational Modeling of Optical Properties of Alloy

##### Nanoparticles

Theoretical investigation of SPR properties of alloy nanoparticles and their effect on vicinal luminophores require the exact knowledge of their exact dielectric constants. For the calculation of dielectric constants of alloy nanoparticles some semi-empirical models developed on the basis of assumption of homogeneous distribution of metallic atoms in their alloys exist in literature. However, there is one major limitation in applying this approach to Ag-Cu nanoparticles. Ag-Cu cannot form a solid solution at room temperature as does Ag-Au. In Ag-Cu nanoparticles, silver and copper remain phase separated.<sup>8-10</sup> With increase in annealing temperature, Cu atoms surface-segregate, thereby increasing the concentration of Ag in the nanoparticle core. So, the effect of metal segregation in the nanoparticles due to thermal annealing or from metallic interactions needs to be modeled. Knowledge of the atomic distribution profile in Ag-Cu alloy nanoparticles simulated at different temperature using molecular dynamics can give useful insights to understand the effect of annealing by computation of the atomic distribution profiles in the nanoparticles. This information about atomic distribution can

be used to calculate accurate dielectric constant for the room temperature and annealed Ag-Cu nanoparticles by constructing a statistical mechanical model.

## References

- 1 J. R. Lakowicz, *Principles of Fluorescence Microscopy*, 2nd ed. (Plenum, NY, 1999).
- 2 K. Aslan, I. Gryczynski, J. Malicka, E. Matveeva, J. R. Lakowicz, and C. D. Geddes, *Curr. Opin. Biotech.* 55, 16 (2005).
- 3 K. Aslan, J. R. Lakowicz, and C. D. Geddes, *Anal. Bioanal. Chem.* 382, 926 (2005).
- 4 A. Yekta, Z. Masoumi, and M. A. Winnik, *Can. J. Chem.* 73, 2021 (1995).
- 5 J. N. Demas, B. A. Deora, and W. Xut, *Anal. Chem.* 67, 1377 (1995).
- 6 K. Aslan, Meng Wu, J. R. Lakowicz, and C. D. Geddes, *J. Am. Chem. Soc.* 129, 1524 (2007).
- 7 M. H. Chowdhury, K. Aslan, S. N. Malyn, J. R. Lakowicz, and C. D. Geddes, *J. Fluoresc.* 16, 295–299 (2006).
- 8 L Wang, J Li, S Song, D Li, C Fan, *J. Phys. D: Appl. Phys.* 203001, **42** (2009)
- 9 C. D. Geddes and J. R. Lakowicz, *J. Fluoresc.* 12, 121 (2002).
- 10 C. D. Geddes, A. Parfenov, and J. R. Lakowicz, *Appl. Spectrosc.* 57, 526 (2003).
- 11 J. R. Lakowicz, J. Malicka, I. Gryczynski, Z. Gryczynski, and C. D. Geddes, *J. Phys. D: Appl. Phys.* 36, R240–R249 (2003).
- 12 K. Ray, R. Badugu, and J. R. Lakowicz, *J. Am. Chem. Soc.* 128, 8998 (2006).
- 13 K. Ray, R. Badugu, and J. R. Lakowicz, *Langmuir* 22, 8374 (2006).
- 14 K. Ray, R. Badugu, and J. R. Lakowicz, *J. Phys. Chem. B* 110, 13499 (2006).
- 15 J. Zhang, Y. Fu, and J. R. Lakowicz, *J. Phys. Chem. C* 111, 1955 (2007).

- 16 J. Zhang, E. Matveeva, I. Gryczynski, Z. Leonenko, and J. R. Lakowicz, *J. Phys. Chem. B* 109, 7969 (2005).
- 17 Y. Zhang, K. Aslan, M. J. R. Previte, and C. D. Geddes, *Appl. Phys. Lett.* 90, 173116 (2007).
- 18 Y. Zhang, A. Dragan, and C. D. Geddes, *J. Phys. Chem. C* in press (2009).
- 19 J. Malicka, I. Gryczynski, Z. Gryczynski, and J. R. Lakowicz, *Anal. Biochem.* 315, 57 (2003).
- 20 K. Sokolov, G. Chumanov, and T. M. Cotton, *Anal. Chem.* 70, 3898 (1998).
- 21 S. Pan and L. J. Rothberg, *J. Am. Chem. Soc.* 127, 6087 (2005).
- 22 P. P. Pompa, L. Martiradonna, A. D. Torre, F. D. Sala, L. Manna, M. D. Vittorio, F. Calabi, R. Cingolani, and R. Rinaldi, *Nat. Nanotechnol.* 1 (2006).
- 23 D. Cheng and Q.-H. Xu, *Chem. Commun.*, 248 (2007).
- 24 Y. Chen, K. Munechika, and D. S. Ginger, *Nano Lett.* 7, 690 (2007).
- 25 F. Tam, G. P. Goodrich, B. R. Johnson, and N. J. Halas, *Nano Lett.* (2007).
- 26 M. Thomas, J.-J. Greffet, and R. Carminati, *Appl. Phys. Lett.* 85, 3863 (2004).
- 27 K. Aslan and C. D. Geddes, *J. Fluoresc.* 16, 3 (2006).
- 28 K. Aslan, P. Holley, and C. D. Geddes, *J. Immunol. Methods* 312, 137 (2006).
- 29 K. Aslan, S. N. Malyn, and C. D. Geddes, *J. Fluoresc.* 17, 7 (2007).
- 30 J. Azoulay, A. Débarre, A. Richard, and P. Tchénio, *Europhys. Lett.* 51, 374 (2000).
- 31 P. Bharadwaj, P. Anger, and L. Novotny, *Nanotechnology* 4, 0957 (2007).
- 32 A. Ishida and T. Majima, *Analyst* 125, 535–540 (2000).
- 33 J. Kümmerlen, A. Leitner, H. A. Brunner, F. R. A. Aussenegg, and A. Wokaun, *Mol. Phys.* 80, 1031 (1993).
- 34 E. G. Matveeva, I. Gryczynski, A. Barnett, Z. Leonenko, J. R. Lakowicz, and Z. Gryczynski, *Anal. Biochem.* 363, 239 (2007).
- 35 L. Shang, H. Chen, and S. Dong, *J. Phys. Chem. C* 111, 10780 (2007).

- 36 L. Yan, H. Liu, and H. Iwasaki, *Chem. Phys. Lett.* 433, 312 (2007).
- 37 Z. Yongxia, A. Kadir, J. R. P. Michael, and D. G. Chris, *Appl. Phys. Lett.* 90, 053107 (2007).
- 38 J. Zhang, Y. Fu, M. H. Chowdhury, and J. R. Lakowicz, *Nano Lett.* 7, 2101 (2007).
- 39 J. R. Lakowicz, Y. Shen, S. D'Auria, J. Malicka, J. Fang, Z. Gryczynski, and I. Gryczynski, *Anal. Biochem.* 301, 261 (2002).
- 40 K. Aslan, J. R. Lakowicz, and C. D. Geddes, *J. Phys. Chem. B* 109, 6247 (2005).
- 41 C. D. Geddes, A. Parfenov, D. Roll, I. Gryczynski, J. Malicka, and J. R. Lakowicz, *J. Fluoresc.* 13, 267 (2003).
- 42 C. D. Geddes, K. Aslan, I. Gryczynski, J. Malicka, and J. R. Lakowicz, *Reviews in Fluorescence*. (Kluwer Academic/Plenum, New York, 2004), pp.365–401.
- 43 E. Dulkeith, M. Ringler, T. A. Klar, J. Feldmann, A. MunozJavier, and W. J. Parak, *Nano Lett.* 5, 585 (2005).
- 44 K. Ray, M. H. Chowdhury, and J. R. Lakowicz, *Anal. Chem.* 79, 6480 (2007).
- 45 R. Pribik, K. Aslan, Y. Zhang and C D. Geddes, *J. Phys. Chem. C* , 112, 17969–17973 (2008).
- 46 K. Aslan, M. J. R. Previte, Y. Zhang, and C. D. Geddes, *J. Phys. Chem. C* 112, 18368–18375 (2008 ).
- 47 A. Dorfman, N. Kumar, and J.-i. Hahn, *Langmuir* 22, 4890 (2006).
- 48 A. Dorfman, N. Kumar, and J.-i. Hahn, *Adv. Mater.* 18, 2685 (2006).
- 49 N. Kumar, A. Dorfman, and J.-i. Hahn, *Nanotechnology* 17, 2875–2881 (2006).
- 50 K. Aslan, M. J. R. Previte, Y. Zhang, and C. D. Geddes, *J Phys. Chem. C* 112, 18368 (2008).
- 51 P. J. Tarcha, J. Desaja-Gonzalez, S. Rodriguez-Llorente, and R. Aroca, *Appl. Spectrosc.* 53, 43 (1999).
- 52 J. C. Hulteen and R. P. V. Duynea, *J. Vac. Sci. Technol. A* 13, 1553 (1995).
- 53 T. R. Jensen, M. L. Duval, K. L. Kelly, A. A. Lazarides, G. C. Schatz, and R. P. V. Duyne, *J. Phys. Chem. B* 103, 9846 (1999).

- 54 T. R. Jensen, G. C. Schatz, and R. P. V. Duyne, *J. Phys. Chem. B* 103, 2394 (1999).
- 55 E. Dulkeith, A. C. Morteani, T. Niedereichholz, T. A. Klar, J. Feldmann, S. A. Levi, F. C. J. M. v. Veggel, D. N. Reinhoudt, M. Mo'ller, and D. I. Gittins, *Phys. Rev. Lett.* 89, 203002 (2002).
- 56 A. Campion, A. R. Gallo, C. B. Harris, H. J. Robota, and P. M. Whitmore, *Chem. Phys. Lett.* 73, 447 (1980).
- 57 T. Huang and R. W. Murray, *Langmuir* 18, 7077 (2002).
- 58 N. N. Horimoto, K. Imura, and H. Okamoto, *Chem. Phys. Lett.* 467, 105–109 (2008).
- 59 S. K. Ghosh, A. Pal, S. Kundu, S. Nath, and T. Pal, *Chem. Phys. Lett.* 395, 366 (2004).
- 60 D. J. Bergman, *Phys. Rev. Lett.* 44, 1285 (1980).
- 61 R. M. Drake and J. E. Gordon, *Am. J. Phys.* 53, 955 (1985).
- 62 G. W. Milton, *J. Appl. Phys.* 52, 5266 (1981).
- 63 G. Mondio, F. Neri, and G. Currb, *Physica Scripta*. T41, 153 (1992).
- 64 S. B. Singham and C. F. Bohren, *Optics Lett.* 12, 10 (1987).
- 65 G. Mie, *Ann. Phys., Lpz* 4 25, 377 (1908).
- 66 F. Wooten, *Optical Properties of Solids*, 1st ed. (Academic Press, New York 1972).
- 67 L. Gao and J. Z. Gu, *J. Phys. D: Appl. Phys.* 35, 267 (2002).
- 68 H. Garcia, J. Trice, R. Kalyanaraman, and R. Sureshkumar, *Phys. Rev. B* 75, 0454391 (2007).
- 69 S. K. Mandal, R. K. Roy, and A. K. Pal, *J. Phys. D: Appl. Phys.* 36, 261–265 (2003).
- 70 Z. Shaoli, L. Xiangang, D. Chunlei, L. Fei, Y. Shaoyun, D. Qiling, and F. Yongqi, *J. Appl. Phys.* 101, 064701 (2007).
- 71 G. Smith, *J. Phys. D: Appl. Phys.* 10, L39 (1977).

- 72 J. C. Maxwell-Garnett, *Phil. Trans. R. Soc. London A* 203, 385 (1904).
- 73 J. Chen, F. Saeki, B. J. Wiley, H. Cang, M. J. Cobb, Z. Y. Li, L. Au, H. Zhang, M. B. Kimmey, X. D. Li, and Y. Xia, *Nano Lett.* 5, 473 (2005).
- 74 E. Prodan and P. Nordlander, *Nano Lett.* 3, 543 (2003).
- 75 E. Prodan, P. Nordlander, and N. J. Halas, *Nano Lett.* 3, 1411 (2003).
- 76 E. Prodan, C. Radloff, N. J. Halas, and P. Nordlander, *Science* 302, 419 (2003).
- 77 B. Sareni, L. Krahenbuhl, A. Beroual, and C. Brosseau, *J. Appl. Phys.* 81, 2375 (1997).
- 78 Y.-I. Xu and B. A. S. Gustafson, *The Astrophys. J.* 513, 894 (1999).
- 79 Q. Xue, *Physica B: Condensed Matter* 344, 129 (2004).
- 80 E. Zubko, Y. Shkuratov, and K. Muinonen, *Opt. Spectrosc.* 91, 273 (2001).
- 81 B. T. Draine and P. J. Flatau, *J. Opt. Soc. Am. A* 11, 1491(1994).
- 82 B. T. Draine, *The Astrophys. J.* 333, 848 (1988).
- 83 F. Nordin, A. Jean, and L. Georges, *J. Chem. Phys.* 111, 1195 (1999).
- 84 D. A. Smith and K. L. Stokes, *Opt. Express* 14, 5746 (2006).
- 85 Y. Wen-Hui, C. S. George, and P. V. D. Richard, *J. Chem. Phys.* 103, 869 (1995).
- 86 M. I. Mishchenko and D. W. Mackowski, *Opt. Lett.* 19, 1604 (1994).
- 87 Y.-I. Xu, *Appl. Opt.* 34, 4573 (1995).
- 88 Y.-I. Xu and B. Å. S. Gustafson, *Appl. Opt.* 36, 8026 (1997).
- 89 T. Nakamura and S. Hayashi, *Jpn. J. Appl. Phys.* 44, 6833–6837 (2005).
- 90 B. J. Messinger, K. U. v. Raben, R. K. Chang, and P. W. Barber, *Phys. Rev. B* 24, 649 (1981).
- 91 E. M. Purcell, *Phys. Rev.* 69, 681 (1946).
- 92 R. Ruppin, *J. Chem. Phys.* 76, 1681 (1982).
- 93 H. Mertens, A. F. Koenderink, and A. Polman, *Phys. Rev. B* 76, 115123 (2007).

- 94 Y. S. Kim, P. T. Leung, and T. F. George, *Surf. Sci.* 195, 1 (1988).
- 95 J. Gersten and A. Nitzan, *J. Chem. Phys.* 75, 1139 (1981).
- 96 H. Mertens and A. Polman, in *ArXiv e-prints* (2007), Vol. 711.
- 97 C.-H. Su, H.-S. Sheu, C.-Y. Lin, C.-C. Huang, Y.-W. Lo, Y.-C. Pu, J.-C. Weng, D.-B. Shieh, J.-H. Chen, and C.-S. Yeh, *J. Am. Chem. Soc.* 129, 2139 (2007).
- 98 H. Cai, N. Zhu, Y. Jiang, P. He, and Y. Fang, *Biosens. Bioelectron.* 18, 1311 (2003).
- 99 M. S. Lang HG, Stevenson KJ, Chandler BD *J Am Chem Soc* 126, 2949–12956 (2004).
- 100 P. Mulvaney, *Langmuir* 12, 788 (1996).
- 101 M. Hirai and A. Kumar, *J. Appl. Phys.* 100, 0143091 (2006).
- 102 M. Hirai and A. Kumar, *J. Electron. Mater.* 36, 1574 (2007).
- 103 F. Hao and P. Nordlander, *Chem. Phys. Lett.* 446, 115, (2007).
- 104 J. Zhu, *Physica E: Low-dimensional Systems and Nanostructures* 27, 296 (2005).
- 105 S. Bruzzone, M. Malvaldi, G. P. Arrighini, and C. Guidotti, *J. Phys. Chem. B* 110, 11050 (2006).
- 106 S. Link, Z. L. Wang, and M. El-Sayed, *J Phys Chem B* 103, 3529–3533. (1999).
- 107 D.-H. Chen and C.-J. Chen, *J. Mater. Chem.* 12, 1557–1562 (2002).
- 108 U. Pal, J. F. S. ramirez, H. B. Liu, A. Medina, and J. A. Ascencio, *Appl. Phys. A* 79, 79 (2004).
- 109 C. Sangregorio, M. Galeotti, U. Bardi, and P. Baglioni, *Langmuir* 12, 5800 (1996).
- 110 J. Hongjin, M. Kyoung-sik, and C. P. Wong, presented at the *Advanced Packaging Materials: Processes, Properties and Interfaces, 2005. Proceedings. International Symposium on, 2005* (unpublished).
- 111 A. B. Smetana, K. J. Klabunde, C. M. Sorensen, A. A. Ponce, and B. Mwale, *J. Phys. Chem. B* 110, 2155 (2006).

- 112 R. G. Haverkamp, A. T. Marshall, and D. v. Agterveld, *J. Nanopart. Res.* 9, 697–700 (2007).
- 113 T. Itakura, K. Torigoe, and K. Esumi, *Langmuir* 11, 4129 (1995).
- 114 Y. Jia, H. Niu, M. Wu, M. Ning, H. Zhu, and Q. Chen, *Mater. Res. Bull.* 40, 1623 (2005).
- 115 K.-i. Okazaki, T. Kiyama, K. Hirahara, N. Tanaka, S. Kuwabata, and T. Torimoto, *Chem. Commun.*, 691 (2008).
- 116 J. Song, H. Li, J. Li, S. Wang, and S. Zhou, *Appl. Opt.* 41, 5413 (2002).
- 117 G. S. Anderson, *J. Appl. Phys.* 40, 2884 (1969).
- 118 J. H. Bell, E. T. Schairer, Lawrence A Hand, and R. D. Mehta, *Ann. Rev. Fluid Mech.* 33 (2001).
- 119 W. J. Bowyer, W. Xu, and J. N. Demas, *Anal. Chem.* 76, 4374 (2004).
- 120 C. N. Jayarajah, A. Yekta, I. Manners, and M. A. Winnik, *Macromolecules* 33, 5693 (2000).
- 121 K. A. Kneas, J. N. Demas, B. Nguyen, A. Lockhart, W. Xu, and B. A. DeGraff, *Anal. Chem.* 74, 1111 (2002).
- 122 S. Fischkoff and J. M. Vanderkooi, *J. Gen. Physiol* 65, 663 (1975).
- 123 M. E. Cox, *J. polymer Sci. A* 24, 621 (1986).
- 124 O. Stern and M. Volmer, *M. Phys. Z* 20, 183 (1919).
- 125 R. Ruffolo, C. E. B. Evans, X.-H. Liu, Y. Ni, Z. Pang, P. Park, A. R. McWilliams, X. Gu, X. Lu, A. Yekta, M. A. Winnik, and I. Manners, *Anal. Chem.* 72, 1894 (2000).
- 126 O. Pekcan and S. Ug̃ur, *J. Colloid Interface Sci.* 217, 154 (1999).
- 127 X. Lu and M. A. Winnik, *Chem. Mater.* 13, 3449 (2001).
- 128 X. Lu, I. Manners, and M. A. Winnik, *Macromolecules* 34, 1917 (2001).
- 129 C. N. Jayarajah, University of Toronto, 1998.
- 130 S. Draxler, M. E. Lippitsch, I. Klimant, M. Kraus, and O. S. Wolfbeis, *J. Phys. Chem.* 99, 3162 (1995).

- 131 S. Draxler and M. E. Lippitsch, *Anal. Chem.* 68, 753 (1996).
- 132 J. R. Bacon and J. N. Demas, *Anal. Chem.* 59, 2780 (1987).
- 133 E. R. Carraway, J. N. Demas, B. A. DeGraff, and J. R. Bacon, *Anal. Chem.* 63, 337 (1991).
- 134 E. R. Carraway, J. N. Demas, and B. A. DeGraff, *Langmuir* 7, 2991 (1991).
- 135 E. R. Carraway, J. N. Demas, and B. A. DeGraff, *Anal. Chem.* 63, 332 (1991).
- 136 J. Hubner and B. Carroll, *AIAA J.* 35, 1790 (1997).
- 137 G. Schappacher and P. Hartmann, *Anal. Chem.* 75, 4319 (2003).
- 138 K. A. Kneas, J. N. Demas, B. A. DeGraff, and A. Periasamy, *Microsc. Microanal.* 6, 551 (2000).
- 139 R. D. Bowman, K. A. Kneas, J. N. Demas, and A. Periasamy, *J. Microsc.* 211, 112 (2003).
- 140 J. M. Bedlek-Anslow, J. P. Hubner, B. F. Carroll, and K. S. Schanze, *Langmuir* 16, 9137 (2000).
- 141 Y. Rharbi, A. Yekta, and M. A. Winnik, *Anal. Chem.* 71, 5045 (1999).
- 142 X Lu, B-H Han, and M. A. Winnik, *J. Phys. Chem. B* 13349, 107, (2003)
- 143 D. R. Paul and A. T. Dibenedetto, *J. Polym. Sci.C* 10, 17 (1965).
- 144 J. Crank, *The Mathematics of Diffusion* second ed. (Oxford University Press, 1975).
- 145 W. J. Koros, J. Wang, and R. M. Felder, *J. Appl. Polym. Sci.* 26, 2805 (1981).
- 146 C. Khoe, S. Chowdhury, V. Bhethanabotla, and R. Sen, *ACI Materials J*, 107,138, (2010).
- 147 H. Shiku, T. Saito, C. Wu, T. Yasukawa, M. Yokoo, H. Abe, T. Matsue, and H. Yamada, *Chemistry Letters* 35, 234 (2006).
- 148 M. G. Siler, N. Bac, and L. Yilmaz, *J. Membr. Sci.* 91, 77 (1994).
- 149 D. Long and F. Lequeux, *Eur. Phys. J. E* 4, 371 (2001).
- 150 D. R. Paul and D. R. Kemp, *J. Polym. Sci. Symp.* 41, 79 (1973).

- 151 J. R. Lakowicz, *Anal. Biochem.* 298, 1 (2001).
- 152 H. Mertens, Utrecht University, 2007.
- 153 G. Schneider, G. Decher, N. Nerambourg, R. Praho, M. H. V. Werts, and M. Blanchard-Desce, *Nano Lett.* 6, 530 (2006).
- 154 F. Tam, G. P. Goodrich, B. R. Johnson, and N. J. Halas, *Nano Lett.* 7, 496 (2007).
- 155 K. Aslan, S. N. Malyn, and C. D. Geddes, *Chem. Phys. Letts.* 453, 222 (2008).
- 156 N. Kato and F. Caruso, *J. Phys. Chem. B* 109, 19604 (2005).
- 157 L. Ao, F. Gao, B. Pan, R. He, and D. Cui, *Anal. Chem.* 78, 1104 (2006).
- 158 W. Zai-Sheng, J. Jian-Hui, L. FU, S. Guo-Li, and Y. Ru-Qin, *Anal. Biochem.* 353, 22 (2006).
- 159 B. Dubertret, M. Calame, and A. J. Libchaber, *Nature Biotechnol.* 19, 365 (2001).
- 160 H. Imahori and S. Fukuzumi, *Adv. Mater.* 13, 1197 (2001).
- 161 W. A. Weimer and M. J. Dyer, *Appl. Phys. Lett.* 79, 3164 (2001).
- 162 Z. Y. Li, J. P. Wilcoxon, F. Yin, Y. Chen, R. E. Palmer, and R. L. Johnston, *Faraday Discuss* 138 363 (2008).
- 163 J. Zhang, H. Liu, Z. Wang, and N. Ming, *J. Solid State Chem.* 180, 1291 (2007).
- 164 <http://en.wikipedia.org/wiki/Cyanine>
- 165 K. B. Male, S. Hrapovic, Y. Liu, D. Wang, and J. H. T. Luonga, *Anal. Chim. Acta* 516 35–41 (2004).
- 166 J. Zhang, H. Liu, Z. Wang, and N. Ming, *J. Solid State Chem.* 180, 1291 (2007).
- 167 E. D. Palik, *Handbook of Optical Constants of Solids*, 1st ed. (Academic Press Inc., Orlando, 1985).
- 168 G. Ren, H. Shi, and Y. Xing, *Nanotechnology* 18, 385604 (2007)..
- 169 P. Bharadwaj and L. Novotny, *Opt. Express*, Vol. 15, Issue 21, pp. 14266-14274 15 14266 (2007).
- 170 M. Meier and A. Wokaun, *Opt. Lett.* 8 (1983).

- 171 S. Weiss, *Science* 283, 1676 (1999).
- 172 L. M. Smith, J. Z. Sanders, R. J. Kaiser, P. Hughes, C. Dodd, C. R. Connell, C. Heiner, S. B. H. Kent, and L. E. Hood, *Nature* 321, 674 (1986).
- 173 M. Pelton, C. Santori, J. Vuckovic, B. Zhang, G. S. Solomon, J. Plant, and Y. Yamamoto, *Phys. Rev. Lett.* 89, 233602 (2002).
- 174 J. Vučkovic, M. Loncar, and A. Scherer, *IEEE J. Quantum Electron.* 36, 1131 (2000).
- 175 F.-C. Gong, D.-X. Wu, Z. Cao, and X.-C. He, *Biosens. Bioelectron.* 22, 423 (2006).
- 176 H. Liu, Y. Ie, T. Yoshinobu, Y. Aso, and H. Iwasaki, *Appl. Phys. Lett.* 88, 061901 (2006).
- 177 E. Matveeva, Z. Gryczynski, J. Malicka, I. Gryczynski, and J. R. Lakowicz, *Anal. Biochem.* 334, 303 (2004).
- 178 K. Aslan, Z. Leonenko, J. R. Lakowicz, and C. D. Geddes, *J Fluoresc* 15, 643 (2005).
- 179 F. Tam, G. P. Goodrich, B. R. Johnson, and N. J. Halas, *Nano Lett.* (2007).
- 180 G. H. Chan, J. Zhao, E. M. Hicks, G. C. Schatz, and R. P. V. Duyne, *Nano Lett.* 7 1947 (2007).
- 181 G. Xu, M. Tazawa, P. Jin, and s. Nakao, *Appl. Phys. A.* 80, 1535 (2005).
- 182 R. G. Haverkamp, A. T. Marshall, and D. v. Agterveld, *J. Nanopart. Res.* 9, 697 (2007).
- 183 M. Moskovits, I. S.-S. loufova, and B. Vlc'kova, *J. Chem. Phys* 116, 10435 (2002).
- 184 Q. Luo and J. D. Andrade, *Journal of Colloid Interface Sci.* 200, 104 (1998).
- 185 R. A. Erb, *J. Phys. Chem.* 69, 1306 (1965).
- 184 B. Nikoobakht, C. Burda, M. Braun, M. Hun, and M. A. El-Sayed, *Photochem. and Photobiol.* 75, 591 (2002).
- 185 X. Li, J. Qian, L. Jiang, and S. He, *Appl. Phys. Lett.* 94, 063111 (2009).

- 186 L. Dyadyusha, H. Yin, S. Jaiswal, T. Brown, J. J. Baumberg, F. P. Booye, and T. Melvin, *Chem. Commun.*, 3201–3203 (2005).
- 187 P. P. H. Cheng, D. Silvester, G. Wang, G. Kalyuzhny, A. Douglas, and R. W. Murray, *J. Phys. Chem. B*, 110, 4637 (2006).
- 188 C. Wu, B. P. Mosher, and T. Zeng, presented at the Mater. Res. Soc. Symp., 2005 (unpublished).
- 189 S.-H. Wu and D.-H. Chen, *J. Colloid Interface Sci.* 273, 165 (2004).
- 190 J. T. Buboltz, C. Bwalya, S. Reyes, and D. Kamburov, *J. Chem. Phys.* 127, 215101 (2007).
- 191 I. Lisiecki, F. Billoudet, and M. P. Pileni, *J. Phys. Chem.* 100, 4160 (1996).
- 192 G. Palazzo, F. Lopez, M. Giustini, G. Colafemmina, and A. Ceglie, *J. Phys. Chem. B* 107, 1924 (2003).
- 193 M. Erecin´ska and I. A. Silver, *Respir Physiol* 128, 263–276 (2001).
- 194 M. Intaglietta, P. C. Johnson, and R. M. Winslow, *Cardiovasc Res* 32, 632–643 (1996).
- 195 T. Jue and S. Anderson, *Ma Reson Med* 13, 524 (1990).
- 196 C. Lochmann, T. Hansel, T. haupl, and J. Beuthan, *Biomed Tech* 51, 111 (2006).
- 197 D. Derkacs, S. H. Lim, P. Matheu, W. Mar, and E. T. Yub, *Appl. Phys. Lett.* 89, 093103 (2006).
- 198 K. Nakayama, K. Tanabe, and H. A. Atwaterb, *Appl. Phys. Lett.* 93, 121904 (2008).
- 199 K. R. Catchpole and A. Polman, *Optics Express* 16, 21793 (2008).
- 200 S. Chowdhury, V. R. Bhethanabotla, and R. Sen, *Appl. Phys. Lett.* 95, 131115 (2009).

## About The Author

Sanchari Chowdhury was born in Kolkata in West Bengal, India. Sanchari holds a BS from National Institute of Technology, Durgapur, India and an MS from Indian Institute of Technology, Roorkee, India, both in chemical engineering.

She began pursuing her Ph.D. degree in the Chemical and Biomedical Engineering Department at University of South Florida in 2006. Her dissertation research deals with the enhancement of luminescence sensors using metallic nanoparticles, resulted in publications in high quality journals such as Applied Physics Letters, Journal of Physical Chemistry C, and Journal of Microscopy and microanalysis. Her research has also resulted in 10+ presentations in prestigious national and international conferences.